MECHANISMS OF SPIKELET GENERATION IN CORTICAL PYRAMIDAL NEURONS

D I S S E R T A T I O N

zur Erlangung des akademischen Grades

doctor rerum naturalium
(Dr. rer. nat.)
im Fach Biologie

eingereicht an der
Lebenswissenschaftlichen Fakultät
Humboldt-Universität zu Berlin

von
Martina Michalikova M.Sc.

Präsident der Humboldt-Universität zu Berlin:
Prof. Dr.-Ing. Dr. Sabine Kunst

Dekan der Lebenswissenschaftlichen Fakultät:
Prof. Dr. Bernhard Grimm

Gutachter/innen:
1. Prof. Dr. Richard Kempter
2. Dr. Romain Brette
3. Dr. James Poulet

Tag der mündlichen Prüfung: 1. Dezember 2016

Abstract

Spikelets are transient spike-like depolarizations of small amplitudes that can be measured in somatic intracellular recordings of many neuron types. Pronounced spikelet activity has been demonstrated in cortical pyramidal neurons *in vivo* (Crochet et al., 2004; Epsztein et al., 2010; Chorev and Brecht, 2012), influencing membrane voltage dynamics including action potential initiation. Nevertheless, the origin of spikelets in these neurons remains elusive. In thi thesis, I used computational modeling to examine the mechanisms of spikelet generation in pyramidal neurons. First, I reviewed the hypotheses previously suggested to explain spikelet origin. I discovered two qualitatively different spikelet types described in the experimental literature. This thesis focuses on the more commonly reported spikelet type, characterized by relatively large amplitudes of up to 20 mV. I found that the properties of these spikelets fit best to an axonal generation mechanism. Second, I explored the hypothesis that somatic spikelets of axonal origin can be evoked with somatodendritic inputs. I identified the conditions allowing these orthodromic inputs to trigger an action potential at the axon initial segment, which propagates along the axon to the postsynaptic targets, but fails to elicit an action potential in the soma and the dendrites. Third, I simulated extracellular waveforms of action potentials and spikelets and compared them to experimental data (Chorev and Brecht, 2012). This comparison demonstrated that the extracellular waveforms of single-cell spikelets of axonal origin are consistent with the data. Together, my results suggest that spikelets in pyramidal neurons might originate at the axon initial segment within a single cell. Such a mechanism might be a way of reducing the energetic costs associated with the generation of output action potentials. Moreover, it might allow to control the dendritic plasticity by backpropagating action potentials.

Zusammenfassung

Unter Spikelets versteht man kleine Depolarisationen mit einer Spike-ähnlichen Wellenform, die man in intrazellulären Ableitungen von verschiedenen Neuronentypen messen kann. In kortikalen Pyramidenzellen wurde ausgeprägte Spikelet-Aktivität nachgewiesen, die erheblich das Membranpotential beeinflussen kann (Crochet et al., 2004; Epsztein et al., 2010; Chorev and Brecht, 2012). Nichtsdestotrotz bleibt der Ursprung von Spikelets in diesen Neuronen unbekannt. In der vorgelegten Arbeit nutzte ich theoretische Modellierung um die Mechanismen von Spikelet-Erzeugung in Pyramidenzellen zu untersuchen. Zuerst sah ich die verschiedenen Hypothesen über den Ursprung von Spikelets durch. In der Literatur entdeckte ich zwei verschiedene Typen von Spikelets. Diese Arbeit konzentriert sich auf den häufiger vorkommenden Typ von Spikelets, welcher durch relativ große Amplituden gekennzeichnet ist. Die Eigenschaften dieser Spikelets passen am besten zu einem axonal Erzeugungsmechanismus. Im zweiten Kapitel widmete ich mich der Hypothese, dass somatische Spikelets axonalen Ursprungs mit somato-dendritischen Inputs hervorgerufen werden können. Ich identifizierte Bedingungen, die es erlauben ein Aktionspotential (AP) am Initialsegment vom Axon (AIS) zu initiieren, welches sich entlang des Axons ausbreitet, aber kein AP im Soma auslöst. Schließlich simulierte ich extrazelluläre Wellenformen von APs und Spikelets und verglich sie mit experimentellen Daten (Chorev and Brecht, 2012). Dieser Vergleich zeigte auf, dass die extrazellulären Wellenformen von Spikelets, die innerhalb einer Zellen am AIS erzeugt werden, gut zu den Daten passen. Zusammenfassend unterstützen meine Ergebnisse die Hypothese, dass Spikelets in Pyramidenzellen am AIS entstehen. Dieser Mechanismus könnte ein Mittel zum Energiesparen bei der Erzeugung von Output-APs sein. Außerdem könnte dadurch die dendritische Plastizität, die auf der Rückwärtspropagierung von APs beruht, reguliert werden.

Contents

1 Introduction

"The brain is a world consisting of a number of unexplored continents and great stretches of unknown territory."

– Santiago Ramón y Cajal

The brain is the central organ of nervous systems, and controls the behavior of animals. It is specialized for information processing including perception, learning and memory, decision making, and motor control. Despite intense research and many ground-breaking discoveries in the last decades, much of the brain functioning is still obscure because of the highly complex structure and signaling based on electrical activity, which is hard to access experimentally.

According to the *neuron doctrine*, initially formulated in 1888–1889 by the spanish investigator Ramón y Cajal, the fundamental structural and functional units of nervous systems are cells called neurons. One element of the neuron doctrine, the *law of dynamic polarization*, states that neurons conduct electrical signals unidirectionally, from dendrites to axons. The axon terminals form synaptic contacts to the dendrites and somata of their downstream targets, where the transmitted synaptic potentials summate temporally. If a certain voltage threshold is crossed, an action potential is evoked, typically at the axon initial segment, which propagates along the axon to the axon terminals (Fig. 1.1).

The action potential is a brief depolarizing event that constitutes one of the main ingredients of neuronal communication. The mechanism of action potential generation and propagation was first described by Hodgkin and Huxley (1952), and is based on the voltage-dependent permeability of the neuronal membrane to sodium and potassium ions. If the membrane potential reaches a certain level, voltage-sensitive sodium channels transiently open and allow the positively-charged sodium ions to flow into the cell, resulting in a strong and fast membrane depolarization. This depolarization triggers the opening of potassium channels, so that positively-charged potassium channels, abundant in the intracellular space of neurons, flow out of the cell and repolarize the membrane potential (Fig. 1.2). The action potential is an all-or-none event, which means that its amplitude does not depend on the strength of the underlying stimulus and appears fairly constant. Thus, this mode of neuronal signaling can be called *digital*, providing the advantages of relatively low energy cost and faithful transmission over long distances (Debanne et al., 2013).

However, the above presented general textbook knowledge became much more nuanced in the last decades, as the technical advances in measurement and analysis methods enabled increasingly detailed study of the biological reality of a given neural system. It has been discovered, for example, that the action potential sometimes naturally propagates in the opposite (antidromic) direction (Sheffield et al., 2010), the spiking threshold is not fixed but depends on the membrane potential history (Henze and Buzsaki, 2001), and the axonal signaling is not purely digital, but subthreshold membrane potential fluctuations influence the axonal output and synaptic transmission in an analog way as well (Alle and Geiger, 2006; Shu et al., 2006).

Many studies on action potential initiation and propagation have been carried out in pyramidal neurons of the hippocampus. The hippocampus became a model system for studying neurophysiology because of its highly organized structure conserved across the mammalian species (Fig. 1.3 A, B). Pyramidal neurons are the principal projecting cells in the hippocampus and neocortex (Fig. 1.3 C), characterized by a triangular cell body giving rise to a thick apical dendrite (Fig. 1.3 D). Besides action potentials, another all-or-none-event has been frequently

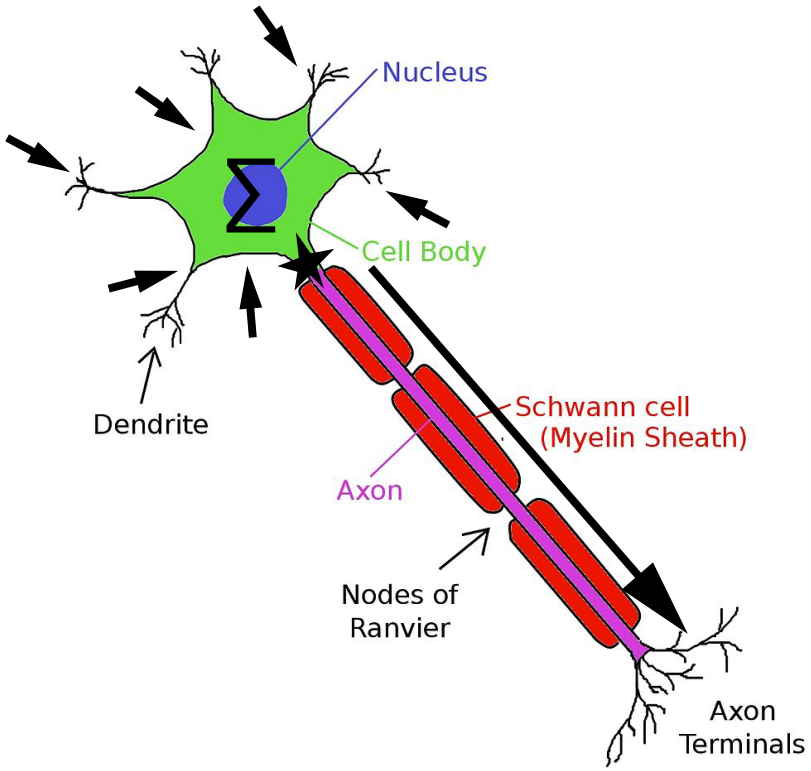

Figure 1.1: Neuronal morphology and the direction of signal conduction.
Neurons are composed of a soma (cell body, green), which contains the nucleus (blue), and two types of cell processes: dendrites and axons (pink). The axon can be insulated by a myelin sheath (red), which is formed by glial cells (Schwann cells and oligodendrocytes in the peripheral and central nervous system, respectively). The axonal patches of membrane without insulation are called Nodes of Ranvier. The axon branches at the end into axon terminals, which contact dendrites and somata of other neurons, creating the substrate for chemical synapses. Synaptically transmitted signals called postsynaptic potentials (thick short arrows) summate in the soma (Σ). The action potential is initiated at the axon initial segment (black star) and propagates along the axon (long thick arrow). Adapted from: `https://en.wikipedia.org/wiki/File:Neuron1.jpg` by NickGorton-commonswiki, used under the Creative Commons Attribution-Share Alike 3.0 Unported. To view a copy of this licence, visit `https://creativecommons.org/licenses/by-sa/3.0/deed.en`.

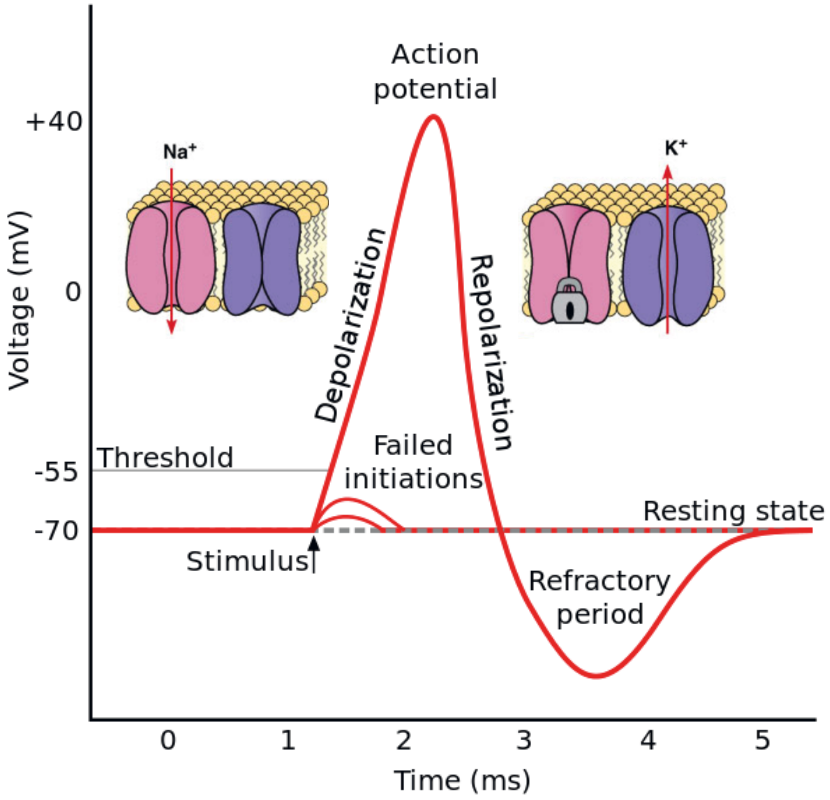

Figure 1.2: Action potential and its phases.
Illustration of an action potential waveform (red), and sodium (pink) and potassium (blue) ion channels (insets). Electrical stimulus that is strong enough to depolarize the membrane over its firing threshold causes the voltage-dependent sodium channels to open, which leads to inflow of sodium ions and more depolarization. After a brief period of time ($<$ 1 ms), the sodium channels close and the voltage-dependent potassium channels open. As a consequence, potassium ions flow out of the cell, thus repolarizing the membrane again. Then a refractory phase of one to few milliseconds follows, when the sodium channels cannot open (lock symbol in the inset right), thus no action potential can be triggered in this period. Adapted from: `https://en.wikipedia.org/wiki/File:Action_potential.svg` by Tomtheman5, used under the Creative Commons Attribution-Share Alike 3.0 Unported. To view a copy of this licence, visit `https://creativecommons.org/licenses/by-sa/3.0/deed.en`.

observed in somatic intracellular recordings of pyramidal neurons: the spikelet. Spikelet waveforms resemble action potentials, but their amplitudes are smaller (Fig. 2.1). Nevertheless, spikelets in pyramidal neurons exhibit amplitudes large enough to trigger somatic action potentials and, thus, influence the computations of pyramidal neurons. So it is not surprising that several studies attempted to resolve the question of spikelet origin. However, it has proved difficult to distinguish between the different hypotheses of spikelet generation with a purely experimental approach.

This thesis aims at complementing the experimental studies with computational modeling to elucidate spikelet origin in pyramidal neurons. In chapter 2, I review the various mechanisms that can lead to the generation of spikelets. I compare the theoretical predictions about spikelet properties produced by each of the mechanism to the spikelet data from pyramidal neurons. In chapter 3, I propose a novel hypothesis for spikelet origin. I argue that spikelets in pyramidal neurons can arise from action potentials initiated with somato-dendritic inputs at the axon initial segment that only propagate down the axon, but do not trigger a somatic action potential. I examine the implications of this hypothesis with minimal cable models and with biophysically complex models of pyramidal neurons. In chapter 4, I simulate extracellular waveforms of action potentials and spikelets produced with the novel single-cell mechanism proposed in chapter 2 as well as spikelets generated in pairs of neurons electrotonically coupled by gap junctions. Comparing these modeling results to the corresponding experimental data reveals that the axonal single-cell mechanism provides a good match to the data. Overall, this work presents a strong support for the axonal origin of spikelets in pyramidal neurons.

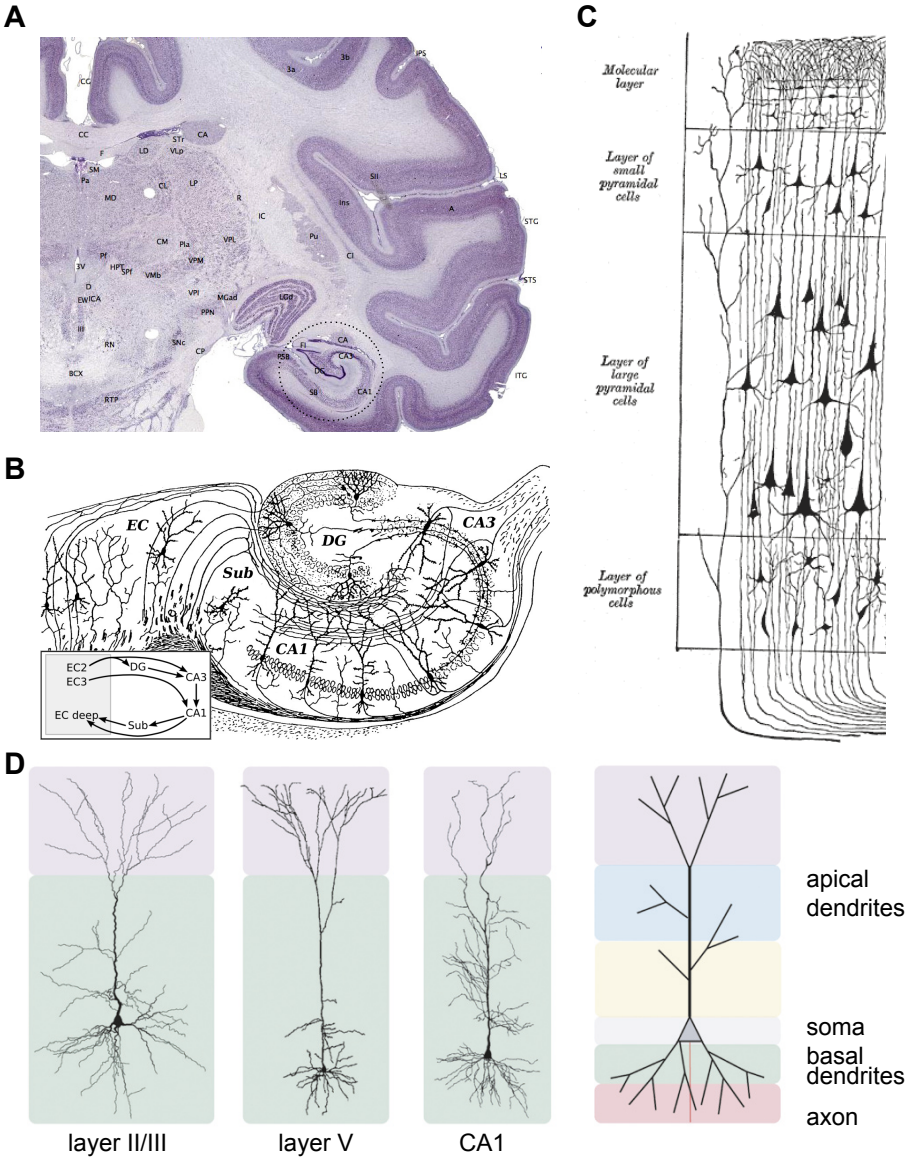

Figure 1.3: Cerebral cortex and its principal neurons.
A: A Nissl-stained section of a macaque-monkey brain. The cerebral cortex is the outer layer (dark violet). The hippocampus is encircled. **B**: Hippocampal circuit drawn by Ramón y Cajal. The inset schematically shows the major excitatory pathways of the hippocampus (DG: dentate gyrus, Sub: subiculum, EC: entorhinal cortex). **C**: A neocortical column with pyramidal neurons. The "layer of small pyramidal cells" and the "layer of large pyramidal cells" are also called layer II/III and layer V, respectively. **D**: Morphologies of example pyramidal cells from the neocortical layers II/III and V, as well as from the hippocampal CA1 region. Right: A schematic morphology of a pyramidal neuron with a soma, apical and basal dendrites, and an axon (red). The shaded background represents regions that could receive unique synaptic input. A: From `https://en.wikipedia.org/wiki/File:Brainmaps-macaque-hippocampus.jpg` by brainmaps.org, used under the Creative Commons Attribution-Share Alike 3.0 Unported. To view a copy of this licence, visit `https://creativecommons.org/licenses/by-sa/3.0/deed.en`. B: From `https://en.wikipedia.org/wiki/File:CajalHippocampus_(modified).png`, derived by Looie496 from an original by Santiago Ramón y Cajal, public domain. C: Adapted from `https://en.wikipedia.org/wiki/File:Gray754.png` by Henry Vandyke Carter, public domain. D: Reprinted by permission from Macmillan Publishers Ltd: Nat Rev Neurosci, Spruston (2008), ©(2008), all rights reserved.

2 Spikelets and the various origins of the underlying spikes: a review

Spikelets are non-synaptic events of small amplitudes (< 30 mV) that occur in intracellular recordings in many types of neurons. Because of their spike-like appearance and all-or-none character, spikelets are considered to originate in APs generated in electrotonically distinct neuronal compartments, when currents from a remote AP influence the membrane voltage of the recorded compartment, but do not suffice to initiate an AP there. As spikelets are typically measured in somatic recordings, the underlying APs might, in principle, occur in dendritic or axonal compartments within the same cell or in another cell coupled by gap junctions or ephaptically through extracellular fields. Since each of these mechanisms has different functional implications, it is important to determine the origin of spikelets to assess their computational role in a given system.

One factor that complicates (comparative) spikelet studies and contributes to the confusion about their origin is the many different names for spikelets that can be found in the literature. These alternative names, sometimes reflecting the presumed origin of spikelets, include: "IS spikes" (IS: initial segment; Coombs et al., 1957a), "fast prepotentials" (FPPs; Spencer and Kandel, 1961), "short-latency depolarizations" (Llinas et al., 1974), "d-spikes" (d:dendritic; Wong and Stewart, 1992), "partial spikes" (Zhang et al., 1998), "small spikes" (Connors and Kriegstein, 1986), "third potentials" (Kaplan and Shapley, 1984) and "ePSPs" (electrical PSPs; Gibson et al., 2005).

The question of spikelet origin is resolved for some systems. For example, spikelets in cortical interneurons were found to result from electrotonic coupling by dendro-dendritic and somato-dendritic gap junctions, which increases the firing synchrony of interneurons and promotes generation and maintenance of network oscillations (Bennett and Zukin, 2004). In contrast, the origin of spikelets in pyramidal neurons is still not settled. Virtually all possible spikelet mechanisms have been hypothesized to explain spikelet occurrence in these cells, but the experimental evidence is ambiguous.

In this chapter, I first describe the properties of spikelets recorded in cortical pyramidal neurons, noting that there are at least two qualitatively distinct spikelet types occuring in these cells. Then I review the various mechanisms that can give rise to spikelets. I present theoretical considerations about spikelet properties generated by each of the possible mechanisms and compare them to experimental data from pyramidal neurons. I also discuss the functional implications of each type of spikelet. I argue that the large-amplitude spikelets occurring in pyramidal neurons at high frequencies (Fig. 2.1 A and B) are best explained by axonal origin. In contrast, the small-amplitude spikelets with fast decay (Fig. 2.1 C and D) might be caused by ephaptic coupling to a close-by neuron.

2.1 Properties of spikelets in pyramidal neurons

At least two qualitatively different spikelet types have been observed in cortical pyramidal cells (Fig. 2.1). The first spikelet type (Fig. 2.1 A and B) is characterized by relatively large amplitudes (typically $3 - 20$ mV) and fast rise dynamics (max. dV/dt of $10 - 40$ V/s). The decay is often, but not always, biphasic, with an initial faster phase (time constant < 1 ms) followed by

a slower phase (time constant > 5 ms; Fig. 2.1 A and B right). These large-amplitude spikelets show an all-or-none behavior, and in a single cell there is usually one, rarely two, discrete amplitudes of spikelets. The generation of these spikelets is voltage-dependent, where somatic hyperpolarization suppresses the spikelets and somatic depolarization promotes the spikelet incidence (Crochet et al., 2004; Chorev and Brecht, 2012). Moreover, the large-amplitude spikelets are sensitive to sodium channel blockers, which suggests that they are actively propagating in the recorded cells (Schmitz et al., 2001; Crochet et al., 2004). This type of spikelet occurs as a single event or in bursts with short inter-spikelet-intervals of few milliseconds (Fig. 2.1 B; Chorev and Brecht, 2012). Interestingly, the large-amplitude spikelets can trigger somatic APs, which show a distinct initial rising phase ("shoulder") that fits the spikelet waveform (Epsztein et al., 2010). In CA1 pyramidal neurons *in vivo*, firing rates of these spikelets show spatial modulation with place fields virtually identical to the place fields of somatic APs (Epsztein et al., 2010).

A different type of spikelet was also found in both neocortical (Fig. 2.1 C, Scholl et al., 2015) and hippocampal (Fig. 2.1 D, Valiante et al., 1995) pyramidal neurons. These spikelets exhibit smaller amplitudes ($1 - 6$ mV) and a brief time course (width at half-maximum amplitude < 0.5 ms). Frequently, spikelets of several discrete amplitudes appear in a single cell, with inter-spikelet-intervals similar to the inter-spike-intervals. These small-amplitude spikelets occur independently of the somatic membrane potential or somatic APs. Accordingly, they are not suppressed by somatic hyperpolarization and were even observed superimposed on somatic AP bursts (Fig. 2.1 D). In CA1 pyramidal neurons, such spikelets were found during calcium-free-induced epileptic activity in slices (Valiante et al., 1995). Their occurrence correlated with population activity, as both were co-modulated by pH. Brief spikelets were also reported in cat visual neocortex (Fig. 2.1 C; Scholl et al., 2015), where they shared several sensory selectivities with the APs, including orientation selectivity, receptive field location, and eye preference. However, binocular disparity tuning was typically not correlated between the APs and spikelets, and in half of the cells, the simple-cell/complex-cell receptive field properties did not match between APs and spikelets (Scholl et al., 2015).

The following sections reviewing spikelet properties generated with the various mechanisms reveal that the first type of spikelet (Fig. 2.1 A and B) fits best to axonal origin within a single cell. The second type of spikelet (Fig. 2.1 C and D) matches the properties of spikelets generated via ephaptic coupling to a neighboring cell.

2.2 Spikelets evoked by dendritic spikes

Historically, one of the first studies on spikelets in cortical neurons was carried out by Spencer and Kandel (1961). In 25% of units recorded in cat hippocampus *in vivo*, the authors observed fast events of small, but constant amplitudes (mean 5.9 ± 2.4 mV), which were initiated approximately 10 mV below the usual AP firing threshold of these cells. These events were called "fast prepotentials" (FPPs), because under normal conditions, they only occured in the rising phase of APs. To study the FPPs in isolation, hyperpolarizing pulses had to be delivered to the soma during spontaneous discharges (Fig. 2.2 A, B). A "process of elimination" was applied to deduce the origin of these events: Since FPPs were present in rebound responses to intracellularly delivered hyperpolarization (Fig. 2.2 B), the authors reasoned that they probably originated within the impaled neurons. The decay of isolated FPPs appeared faster than a purely passive process (Fig. 2.2 C), so active currents were postulated in FPP generation. Next, as the antidromically evoked APs never showed FPPs, the authors proposed that FPPs might reflect dendritic spikes that are attenuated on their way to the soma. And finally, the presence of FPPs in response to subicular stimulation let the authors conclude that they originated in the apical dendritic tree where subicular inputs converge via the perforant pathway. Due to the stereotypic appearance and small amplitudes of FPPs, the underlying dendritic spikes were supposed to occur in a single discrete area of the dendritic tree, separated by passive membrane from the soma. Functionally, FPPs of apical dendritic origin would act as a "booster" for "otherwise ineffectual distal dendritic synapses" (Spencer and Kandel, 1961).

Subsequent studies in the following decades indeed found that several cell types, among them hippocampal interneurons (Martina et al., 2000) and pyramidal cells (Golding and Spruston, 1998), have active dendrites capable of producing fast sodium spikes. However, these dendritic spikes occur in a graded manner (Golding and Spruston, 1998), so they are unlikely to result in all-or-none spikelets such as those described by Spencer and Kandel (1961). Moreover, dendritic sodium channels undergo slow inactivation (Mickus et al., 1999), so they do not support high-frequency firing as is typical for spikelets *in vivo* (e.g., Wong and Stewart, 1992; Crochet et al., 2004; Epsztein et al., 2010). Dual somatic and dendritic intracellular recordings demonstrated that dendritic spikes evoked in the distal apical dendrites of pyramidal neurons often fail to propagate to the soma (Spruston, 2008). However, these failed spikes appear as wide depolarizations at the soma (Fig. 2.3, Golding and Spruston, 1998). Jarsky et al. (2005) discovered that the propagation of distal apical dendritic spikes is substantially facilitated by the activation of more proximal synapses. They observed that some somatically subthreshold responses exhibited spikelets of dendritic origin. Unfortunately, the authors did not report on the amplitude variability of these spikelets. Interestingly, distal apical inputs in CA2 pyramidal cells were shown to efficiently trigger dendritic spikes, which propagated reliably to the soma (Sun et al., 2014). Somatic hyperpolarization or a local TTX application revealed large and fast spikelets (amplitudes of $30 - 40$ mV and max. $\mathrm{dV/dt}$ of $40 - 50$ V/s), however, with graded amplitudes (Sun et al., 2014).

Not only apical, but also basal dendrites of pyramidal neurons contain active conductances and fire dendritic spikes. Here, the resulting somatic spikelets appear rather slow (max. $\mathrm{dV/dt}$ up to 10 V/s) and have a distinct shape: the initial fast sodium spikelet is followed by a slower NMDA-receptor-dependent depolarization (Losonczy et al., 2008; Fig. 2.4 A). The latter, however, can be blocked by recurrent inhibition (Müller et al., 2012; Fig. 2.4 B). Nonetheless, repetitive initiation of dendritic spikes as well as AP backpropagation was found to cause inactivation of sodium channels in basal dendrites lasting for hundreds of milliseconds and resulting in attenuated dendritic spikes (Remy et al., 2009). Together, these properties of dendritic spikes enable basal dendritic branches to function as "independent processing units" (Remy et al., 2009), where local synchronous synaptic input can trigger dendritic spikes, which evoke pre-

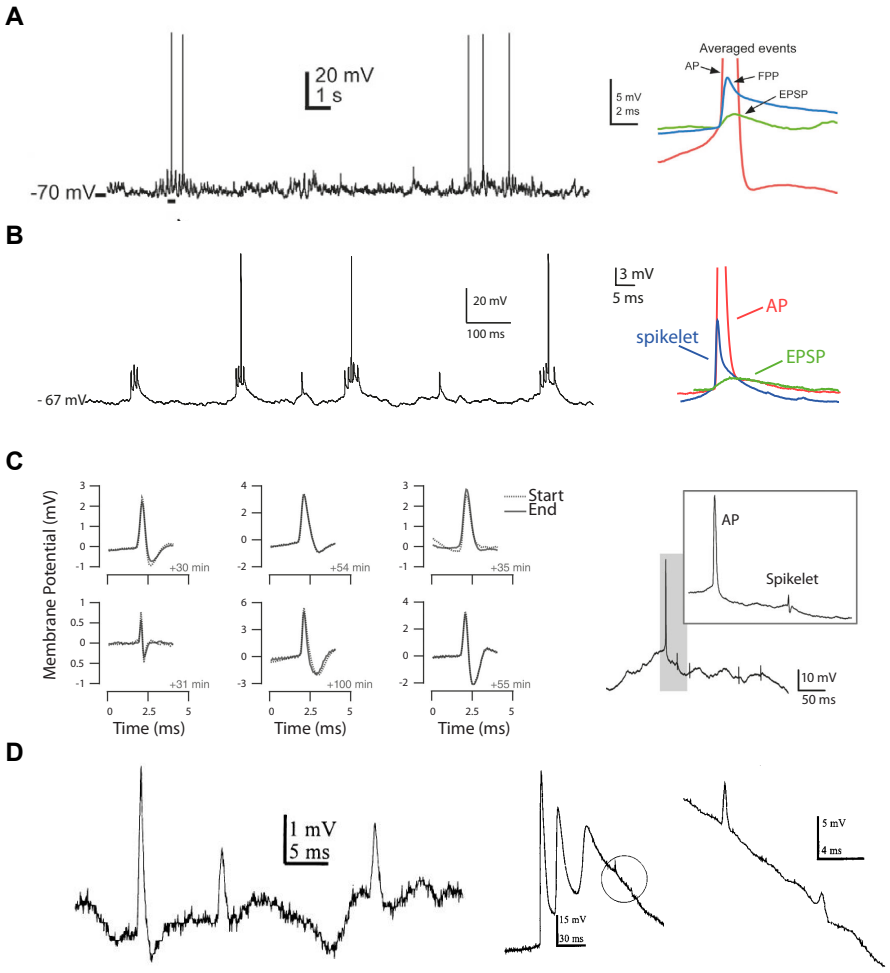

Figure 2.1: Two types of spikelets observed in pyramidal neurons.
A + **B**: Spikelets with a slow component in the decay phase, recorded *in vivo* in putative putative pyramidal cells in cat neocortex (**A**, Crochet et al., 2004) and in hippocampal CA1 pyramidal neurons (**B**, Epsztein et al., 2010). Left: example somatic voltage traces with APs and spikelets. Right: Overlay of mean AP (red, truncated), spikelet ("FPP", blue), and EPSP (green) waveforms.
C + **D**: Spikelets with fast, often hyperpolarizing, decay. **C**: Spikelets from neocortical principal cells recorded in cat visual cortex *in vivo* (Scholl et al., 2015). Left: mean spikelet waveforms from individual cells, as recorded at the beginning (dotted line) and towards the end of the recording session (solid line). Time passed between the two averages is indicated for each example. Right: a voltage trace showing an AP and spikelets, the gray region is enlarged in the inset. Note that the spikelet waveform is briefer than the AP waveform. **D**: Spikelets occurring in CA1 pyramidal neurons *in vitro* during calcium-free-induced epileptic activity (Valiante et al., 1995). Left: example voltage trace with spikelets of two different amplitudes. Middle: AP burst with two spikelets encircled and expanded on the right. A: Reprinted from Crochet et al. (2004) by permission of Oxford University Press. B: From Epsztein et al. (2010). Reprinted with permission of AAAS. C: Reprinted from Scholl et al. (2015), with permission of John Wiley and Sons. D: Republished with permission of Society For Neuroscience, from Valiante et al. (1995); permission conveyed through Copyright Clearance Center, Inc. A-D: all rights reserved.

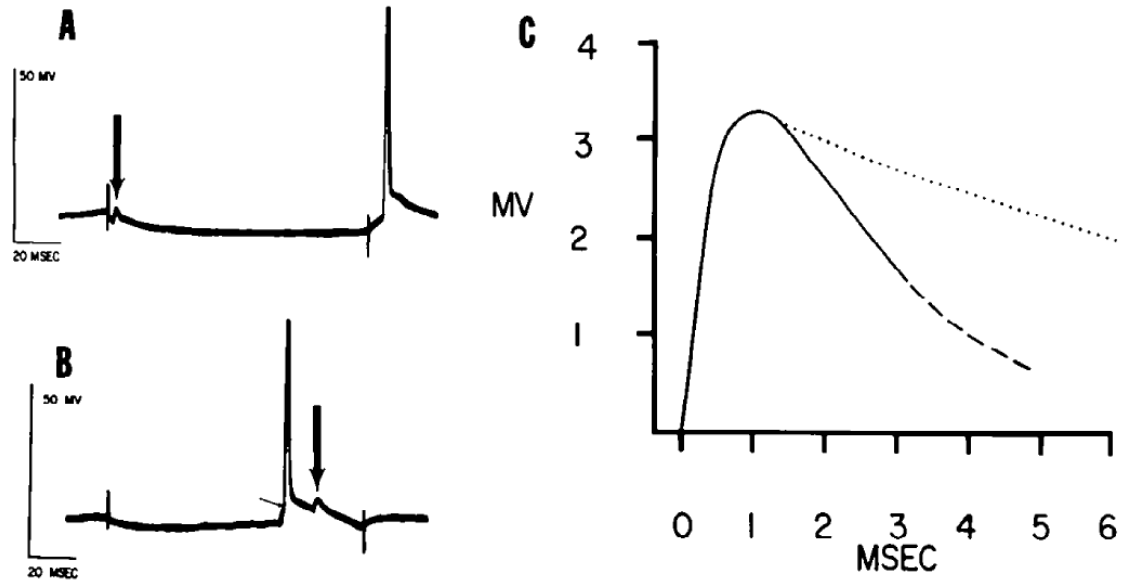

Figure 2.2: "Fast prepotentials" (FPPs) in hippocampal pyramidal neurons *in vivo*.
A: Weak somatic hyperpolarization (presumably applied between the two stimulation artifacts) can isolate FPPs (large vertical arrow, left) in somatic intracellular recordings. In this example, the rebound AP (right) does not show an FPP. **B**: A rebound AP is preceded by an FPP (diagonal mark) and followed by an isolated FPP (large vertical arrow). **C**: Waveform of an isolated FPP (solid line). The dashed part indicates "the uncertainty in judging the baseline on which these small prepotentials ride". Time course of a purely passive decay is depicted as a dotted line. Reprinted from Spencer and Kandel (1961), all rights reserved.

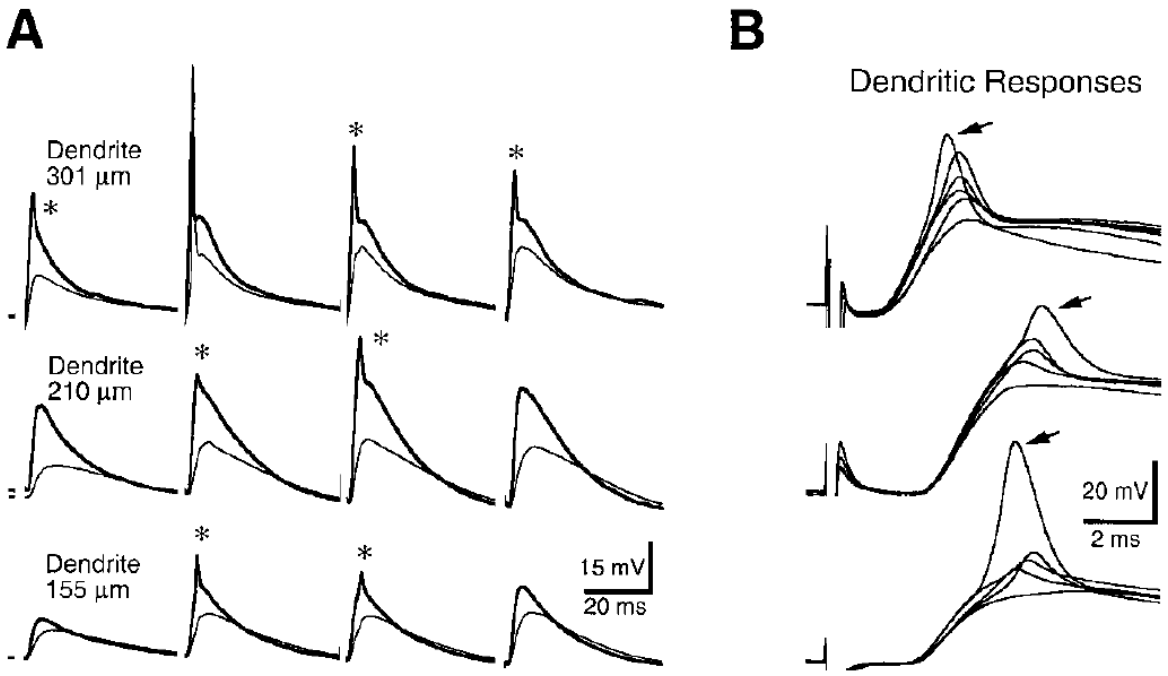

Figure 2.3: Propagation failures of apical dendritic spikes are not manifested as all-or-none somatic spikelets.
A: Dual intracellular recordings in apical dendrites and the soma in three different CA1 pyramidal cells (rows). Shown are synaptically elicited dendritic spikes (asterisks, thick line) that failed to trigger a somatic AP (thin line: somatic traces). **B**: Overlay of dendritic spikes from the three neurons shown in **A** reveal the graded nature of dendritic spikes. Arrows mark spikes that evoked somatic APs. Reprinted from Golding and Spruston (1998), with permission of Elsevier, all rights reserved.

cisely timed AP output.

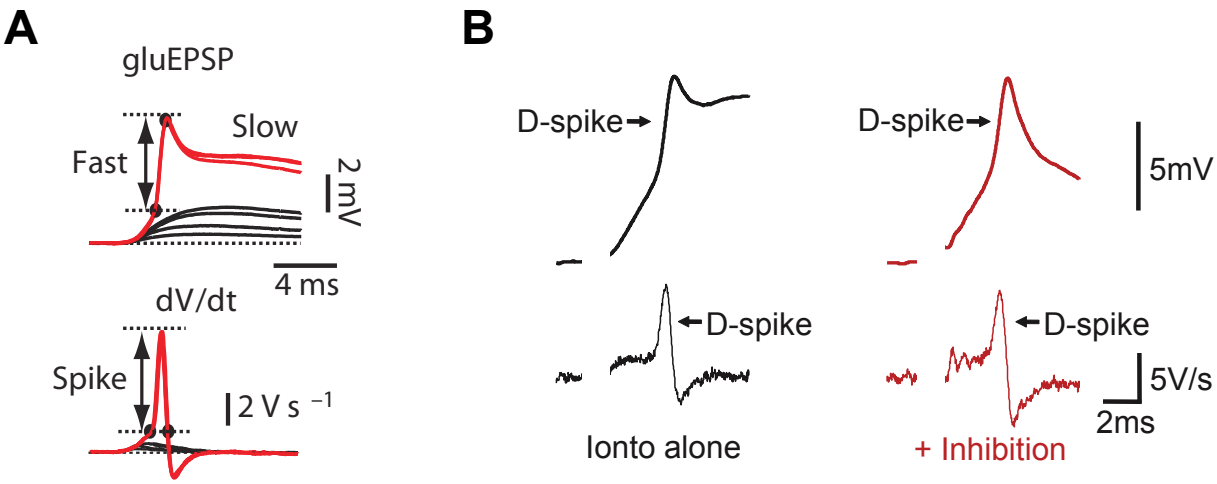

Figure 2.4: Spikelets originating in basal dendrites of CA1 pyramidal neurons.
A: Subthreshold EPSPs (black) and dendritic spikes (red) evoked with uncaged glutamate, measured at the soma. Shown are voltage traces (top) and first time derivatives of voltage (bottom). The dendritic spikes exhibit two distinct components: an initial fast component and a late slow component. Reprinted by permission of Macmillan Publishers Ltd: Nature, Losonczy et al. (2008), ©2008. **B**: Dendritic spikes evoked with glutamate iontophoresis in the absence (black) and in the presence (red) of recurrent inhibition, which blocks the slow spike component. Depicted are somatic voltage traces (top) and first time derivatives of voltage (bottom). Reprinted from Müller et al. (2012), with permission of Elsevier, all rights reserved.

Dendritic spikes are commonly assumed to underly spikelets in pyramidal cells (Wong and Stewart, 1992; Crochet et al., 2004). However, the graded nature of dendritic spikes and the inability of dendrites to fire at higher frequencies do not fit to the all-or-none spikelets occurring at high frequencies in these studies (Wong and Stewart, 1992; Crochet et al., 2004). Similarly to the reasoning by Spencer and Kandel (1961), the dendritic origin of spikelets is often concluded from the observation that spikelets can be evoked by dendritic, but not somatic inputs. The study by Stuart et al. (1997) might help to resolve this paradox: the authors performed triple dendritic, somatic and axonal recordings in layer V pyramidal neurons and demonstrated that output-APs were always initiated in the axon before the soma, even when the dendritic spike preceded the somatic AP (Fig. 2.5). This suggests that spikelets evoked by dendritic inputs do not necessarily reflect dendritic spikes, but might instead stem from axonal APs that are triggered by the dendritic spikes.

2.3 Spikelets generated by axonal action potentials

In this section, I argue that large-amplitude ($3 - 20$ mV) all-or-none spikelets occurring with short inter-spikelet-intervals in pyramidal neurons (Crochet et al., 2004; Epsztein et al., 2010) originate in axonal APs, even when they are evoked with orthodromic (dendritic) stimuli. I first present insights from pioneering studies and complement them with the recent knowledge about the axon initial segment where AP initiation occurs.

Axonal APs and spikelets have been studied in various neuron types as early as in the 1950s. Coombs et al. (1955) examined AP propagation in motoneurons and found that axonal APs evoked with distal axonal stimulus and propagating antidromically towards the soma might

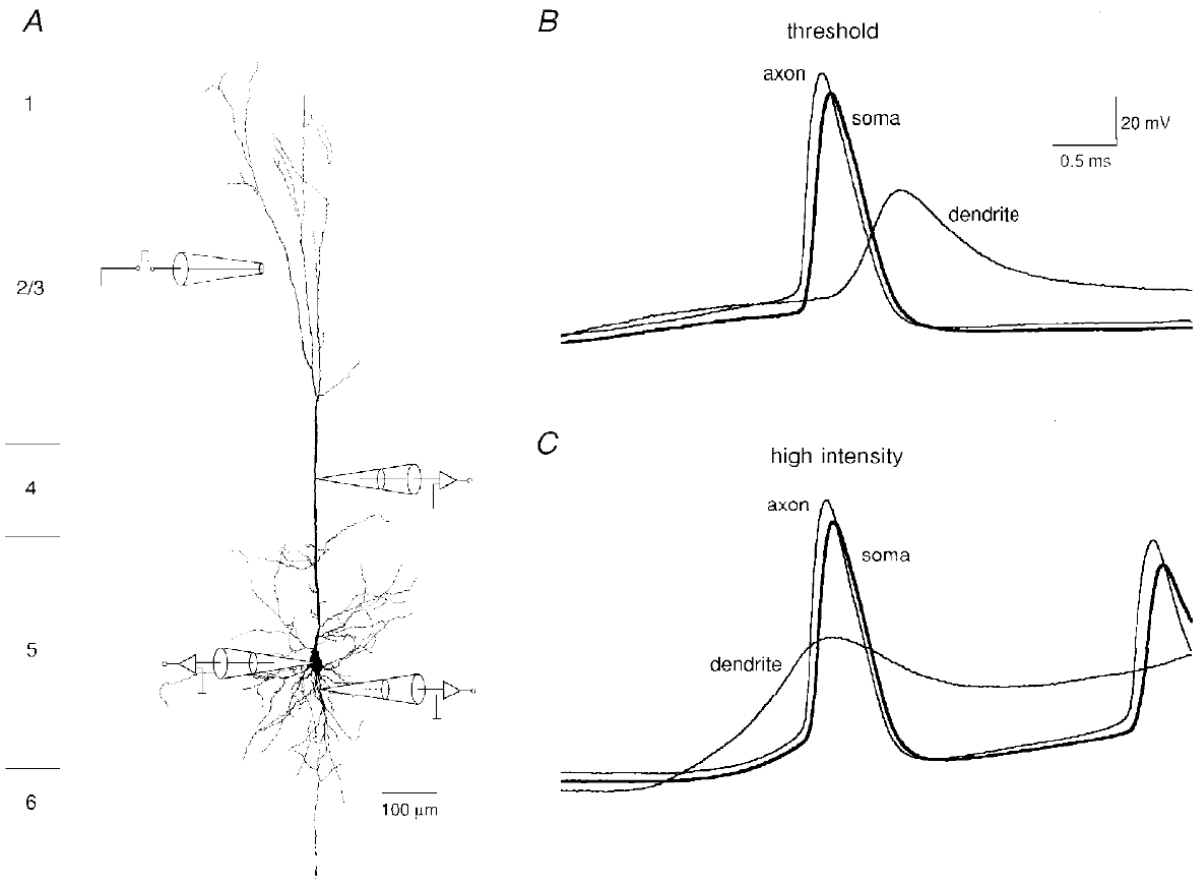

Figure 2.5: APs occur in the axon before the soma, even when the dendritic spike precedes the somatic AP.
A: Drawing of the experimental setting: Synaptic inputs were evoked with an extracellular electrode placed in layer 2/3. Whole-cell patch-clamp recordings were obtained simultaneously at the soma, apical dendrite (300 μm from soma), and axon (20 μm from soma). **B**: A threshold-intensity stimulus resulted in AP initiation at the AIS, followed by a somatic AP and an attenuated backpropagating AP in the dendrite. **C**: A strong stimulus elicited a dendritic spike first, but nevertheless, the axonal AP preceded the somatic AP. Reprinted from Stuart et al. (1997), with permission of John Wiley and Sons, all rights reserved.

fail to activate a somatic AP and appear as an all-or-none spikelet when the somatic membrane voltage is hyperpolarized (Fig. 2.6 A) or strongly depolarized (Fig. 2.6 B). The authors concluded that "there is the same failure of invasion, both when the membrane is heavily depolarized and the activation mechanism is continuously partially engaged, and when the membrane is hyperpolarized and the axonal currents are insufficient to depolarize the membrane to the extent of setting off the activation mechanism" (Coombs et al., 1955). These observations hold also for pyramidal neurons, where somatic hyperpolarization is still a popular method to uncover and study antidromic axonal spikelets (Fig. 2.6 C, Hu et al., 2009).

Another way to generate antidromic spikelets is the so-called "two-shock technique". Here, pairs of brief stimuli are delivered to the distal axon, resulting in a pair of somatic APs. Then, the interstimulus interval is decreased until the failure of the second somatic AP occurs and the underlying (all-or-none) spikelet is unveiled (Fig. 2.6 D, Kandel et al., 1961). This effect can be explained by a shorter relative refractory period of the axon as compared to the soma (Chen et al., 2010) and fits to the common occurrence of spikelets in bursts with short inter-spikelet-intervals (Wong and Stewart, 1992; Crochet et al., 2004; Epsztein et al., 2010). Consequently, the antidromically evoked spikelet is shaped by axial currents generated during the axonal AP propagation that result in a relatively fast and strong somatic depolarization: the spikelet.

However, cortical *in vivo* inputs are usually considered to arrive at the soma orthodromically, and it is not immediately evident how the mechanisms of antidromic spikelet generation might relate to orthodromic spikelets, i.e., spikelets evoked with dendritic synaptic inputs. Remarkably, Coombs et al. (1957a) have shown in a series of experiments, that "when an impulse is generated in a motoneuron by synaptic or direct stimulation, there is the same two-stage invasion [of the soma] as with antidromic activation, though the [temporal] interval between the small-spike [spikelet] and the large-spike is much less than with antidromic invasion [...], and it is more difficult to block the impulse between the two stages". In these experiments, the authors could evoke somatic spikelets with direct (orthodromic) stimulation using the effects of somatic hyperpolarization and refractoriness. For example, somatic spikelets could be triggered by a brief somatic depolarization immediately followed by a hyperpolarizing pulse (Fig. 2.7 A). This closely resembles the situation described by Crochet et al. (2004): "Cortical stimulation evoked a sequence of depolarization-hyperpolarizing potential; the early depolarization was crowned with an FPP [i.e., a spikelet] when it reached the threshold for FPP generation" (Fig. 2.7 B). The simulations presented in chapter 3 agree with the above experimental results and demonstrate that the orthodromic inputs giving rise to spikelets are briefer and weaker than the inputs eliciting APs (Fig. 3.1 H).

Interestingly, already Coombs et al. (1957a) hypothesized that (orthodromic) somatic APs are initiated at the axon initial segment (AIS) where the firing threshold is about 10-20 mV lower than at the soma. Consequently, orthodromic spikelets might be viewed as backpropagated APs elicited at the AIS, which failed to trigger an AP at the soma. This failure does not happen as easily for orthodromic as for antidromic stimulation because the orthodromic stimulus depolarizes the soma closer to its threshold and thus strengthens the coupling between the AIS and soma. However, the initial segment of vertebrate axons has been recently recognized as a distinct, complex, and plastic structure, involved in AP initiation and regulation of neuronal excitability. These recent findings might indicate additional possibilities for spikelet generation, and are reviewed in what follows.

Axon initial segment - the site of AP initiation

As has been discussed above, the axon initial segment has been implicated in the AP generation already decades ago (Coombs et al., 1957a). Additionally, early anatomical research identified its distinct ultrastructure, characterized by microtubule bundles and a dense granular layer underneath the plasma membrane (Fig. 2.8 A; Palay et al., 1968), which distinguishes the AIS

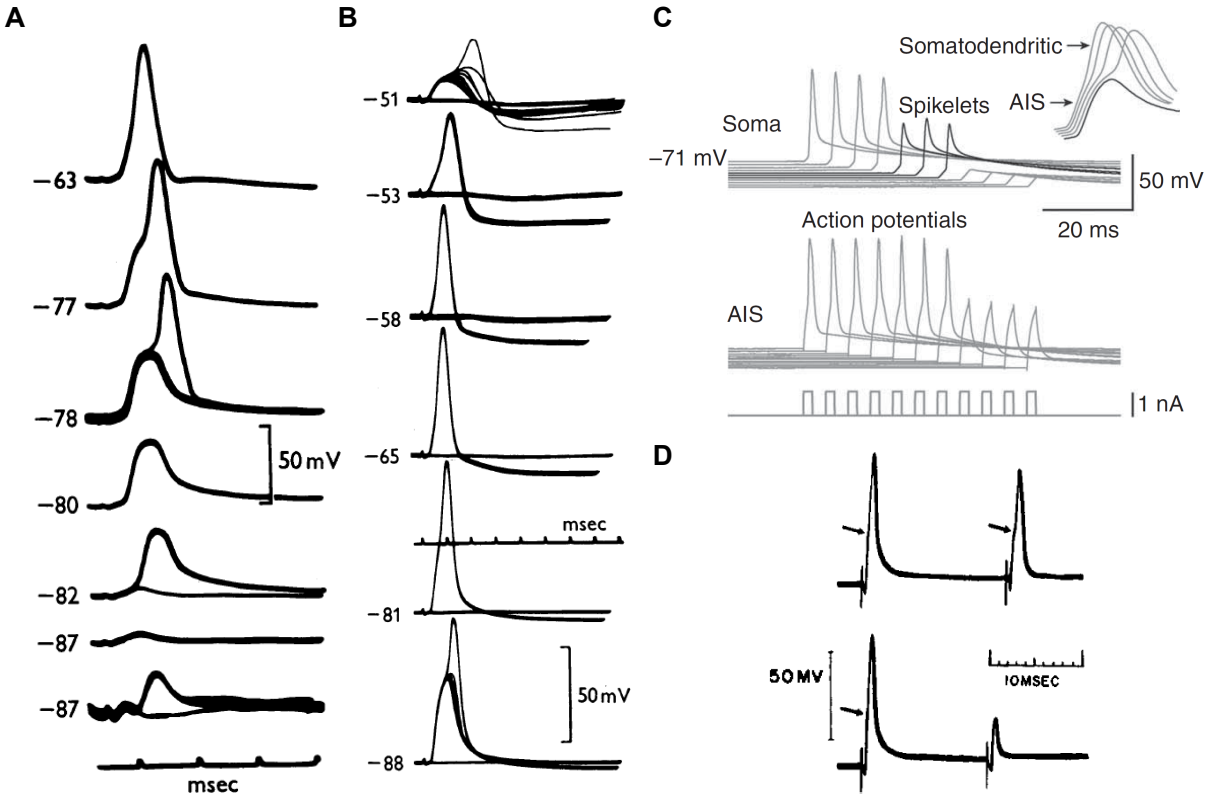

Figure 2.6: Antidromic generation of axonal spikelets.
A: Somatic hyperpolarization of a motoneuron revealed all-or-none spikelets of axonal origin: a large spikelet (3rd – 5th row) was postulated to result from AP propagation failure at the axon hillock – soma boundary. Further hyperpolarization uncovered a smaller spikelet (5th and 6th row; 6th row enlarged below), which was supposed to reflect an AP propagation failure at the transition from the myelinated to the non-myelinated axon. **B**: Somatic depolarization of a motoneuron also resulted in all-or-none spikelets (first row), albeit the transition from full APs to spikelets appeared in a somewhat graded manner. **C**: Somatic hyperpolarization disclosed spikelets in layer V pyramidal neurons (upper traces). The inset shows the correspondence between the initial rising phase of the APs ("shoulder", gray) and the rising phase of the spikelets (black). The simultaneous recordings from the AIS demonstrated APs corresponding to somatic spikelets (lower traces). **D**: In a CA1 pyramidal neuron, applying a sequence of two brief stimuli to the axon results in two APs (first trace), but if the interstimulus interval is small enough, a spikelet is evoked with the second stimulus (second trace). The arrows mark the inflection in the rising phase of the APs corresponding to the spikelet.
A+B: Reprinted from Coombs et al. (1955), with permission of John Wiley and Sons. C: Reprinted by permission of Macmillan Publishers Ltd: Nature, Hu et al. (2009), ©(2009). D: Reprinted from Kandel et al. (1961). A-D: all rights reserved.

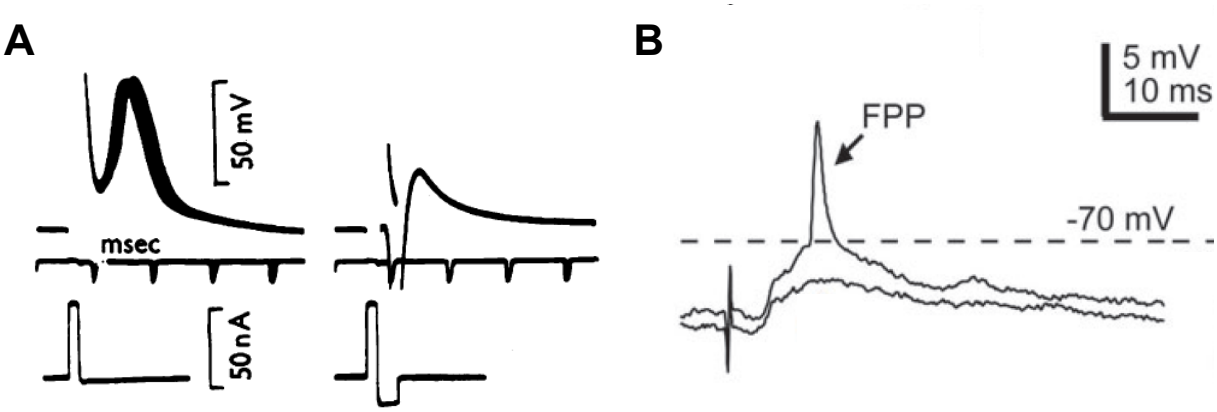

Figure 2.7: Orthodromic generation of spikelets.
A: APs evoked in a motoneuron with somatic current pulses (left). Orthodromic spikelets could be generated when a brief somatic depolarization was immediately followed by a hyperpolarizing pulse (right trace). The current input is depicted below the corresponding voltage trace. Reprinted from Coombs et al. (1957a), with permission of John Wiley and Sons, all rights reserved. **B**: In neocortical pyramidal neurons *in vivo*, spikelets (FPPs) could be triggered by cortical synaptic stimulation, which resulted in somatic depolarization followed by hyperpolarization. Reprinted from Crochet et al. (2004) by permission of Oxford University Press, all rights reserved.

from the rest of the axon. Yet only technical advances in the past decade enabled to study the unique molecular composition of the initial segment in great detail (Fig. 2.8 B, Rasband, 2010), providing the basis for further electrophysiological experiments and modeling work.

Since the early pioneering work, many independent studies have confirmed the AIS as the common site of AP initiation in various neuron types, including the hippocampal (Meeks and Mennerick, 2007) and neocortical (Palmer and Stuart, 2006) pyramidal cells. Also the original proposal has been supported that somatic APs are initiated at the AIS due to its lower firing threshold compared to the soma (Kole and Stuart, 2008). Converging lines of evidence indicated that APs in cortical pyramidal neurons are initiated in the distal part of the AIS (Palmer and Stuart, 2006), where a distinct subtype of Na_V channels was found to cluster (Royeck et al., 2008), activating at more hyperpolarized membrane potentials (Colbert and Pan, 2002). Finally, Hu et al. (2009) demonstrated in layer V pyramidal neurons that the low-threshold $Na_V1.6$ channels accumulate at the distal AIS and promote AP initiation. In contrast, the high-threshold $Na_V1.2$ channels aggregate at the proximal AIS and are responsible for the backpropagation of the AP to the soma (Fig. 2.9). The shift of the activation and inactivation curves between these two channel subtypes was found to lie between 7 mV (Colbert and Pan, 2002) and 13 mV (Hu et al., 2009). However, it is still not resolved whether the effective sodium channel density at the AIS is substantially (up to 50-times) larger than the sodium channel density at the soma (Kole et al., 2008) or whether the sodium channel densities are similar at the soma and AIS (Colbert and Pan, 2002; Fleidervish et al., 2010).

In addition to the shifted activation and inactivation curves, the two Na-channel subtypes $Na_V1.2$ and $Na_V1.6$ were shown to differ in several other properties as well (Rush et al., 2005). The axonal $Na_V1.6$ subunit was identified to generate larger persistent sodium current than the somatic $Na_V1.2$ subunit (Fig. 2.10 A, Rush et al., 2005). The axonal persistent current was found to be active already at resting potentials and to contribute to the low firing threshold of the AIS and to rapid AP initiation (Fleidervish et al., 2010). Relevant for spikelet generation is

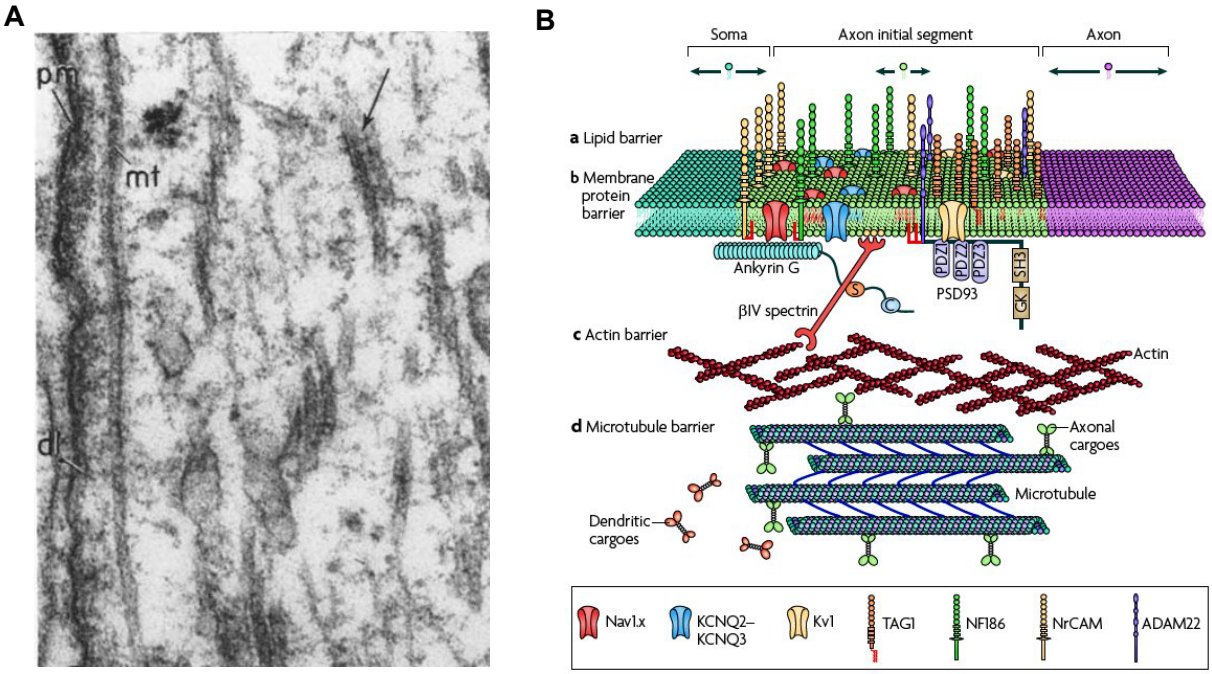

Figure 2.8: AIS ultrastructure.
A: A micrograph of an AIS reveals a dense layer (dl) underneath the plasma membrane (pm) and bundles of microtubules (mt) connected with cross-bars (arrow). Magnification: $83,000\times$. Reprinted with permission from Palay et al. (1968), all rights reserved. **B**: A current view of the rich ultrastructure of the AIS. Reprinted by permission from Macmillan Publishers Ltd: Nature, Rasband (2010), ©(2010), all rights reserved.

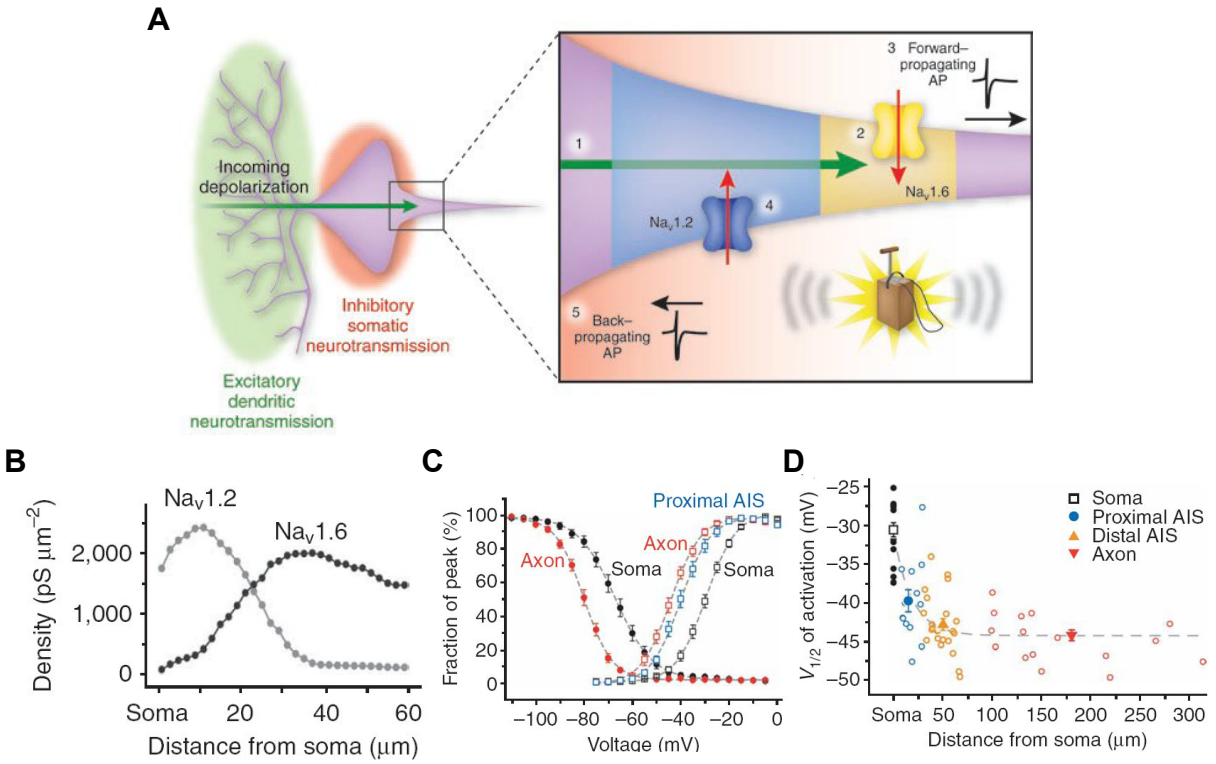

Figure 2.9: APs are initiated at the distal AIS.
A: Schematic picture of AP initiation. Incoming depolarization (green arrow) initiates an AP in the distal AIS (yellow) where the low-threshold $Na_V1.6$ channels are localized. From there, the AP propagates forward along the axon as well as backpropagates to the soma. Reprinted by permission from Macmillan Publishers Ltd: Nat Neurosci, Dulla and Huguenard (2009), ©(2009), all rights reserved. **B**: Distribution of $Na_V1.2$ (gray) and $Na_V1.6$ (black) channel densities along the AIS, as estimated from immunofluorescence measurements. **C**: Activation (empty squares) and inactivation (full circles) curves of somatic (black) and axonal (red) sodium currents. The activation curve for proximal AIS (blue) was added for comparison. **D**: Half-activation voltages of sodium channels measured along the soma and axon. B–D: Reprinted by permission from Macmillan Publishers Ltd: Nature, Hu et al. (2009), ©(2009), all rights reserved.

also the finding that the axonal $Na_V1.6$ subtype is able to better sustain high-frequency firing and conducts more current at high frequencies than the predominantly somatic $Na_V1.2$ channel subtype (Fig. 2.10 B, Rush et al., 2005). This might be at least partly caused by the slow, cumulative inactivation that was found in somato-dendritic, but not axonal sodium channels (Mickus et al., 1999), and predicts that high-frequency axonal firing is accompanied by high-frequency occurrence of somatic spikelets, as has been observed, for example, by Crochet et al. (2004) or Epsztein et al. (2010).

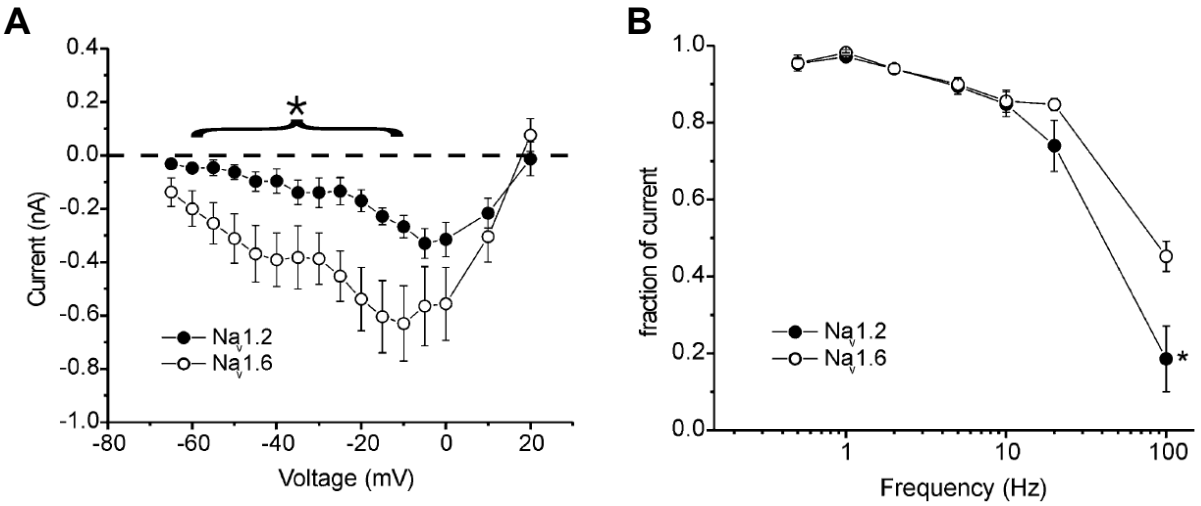

Figure 2.10: Electrophysiological properties of $Na_V1.6$ and $Na_V1.2$ sodium channels.
A: $Na_V1.6$ channels (empty circles) generate larger persistent current than the $Na_V1.2$ channels (full circles). **B**: $Na_V1.6$ channels conduct more current during high-frequency stimulation than the $Na_V1.2$ channels. Reprinted from Rush et al. (2005) with permission from John Wiley and Sons, all rights reserved.

Besides the $Na_V1.6$ sodium channels, several potassium channel types are specifically localized in the axon and enriched at the AIS. The fast activating and slowly inactivating K_V1 channels are co-localized at high densities with $Na_V1.6$ subunits at the distal AIS, but are rare at the soma. Kole et al. (2007) found that these potassium channels regulate the axonal AP waveform independently from the soma. Furthermore, the authors have shown that the AP width at the soma and the axon is modulated by different firing patterns: somatic APs become wider during high-frequency bursts, whereas axonal APs broaden during slow rhythmic activity (Kole et al., 2007). As the AP width at axon terminals controls the efficacy of excitatory synaptic transmission (Geiger and Jonas, 2000), this suggests that neuronal activity can be integrated in the axon independently from the soma. The slowly activating and non-inactivating K_V7 channels are likewise abundant in the AIS. They generate the subthreshold M-current, which diminishes neuronal excitability by increasing the AP threshold. In CA1 pyramidal neurons, the M-current has been found to suppress the intrinsic spontaneous firing of these neurons (Shah et al., 2008).

The studies reviewed above imply that the variety of ion channels specifically targeted to the AIS provide powerful posibilities to set and regulate neuronal excitability and AP generation. Indeed, recently emerging evidence indicates that the neuron type-specific differences in firing properties and AP waveform can be largely explained by differences in the composition and organization of the axon initial segments (Lorincz and Nusser, 2008; Kress et al., 2010). Moreover, it has been shown that the AIS is a highly plastic region and its length as well as position can undergo activity-dependent plasticity (Fig. 2.11, Grubb and Burrone, 2010a; Kuba et al., 2010). And finally, the AIS is exclusively targeted by the synapses of a specific interneuron

type, called Chandelier or axo-axonic neuron (Buhl et al., 1994). However, it is currently not resolved whether these synapses are inhibitory (Glickfeld et al., 2008) or excitatory (Szabadics et al., 2006) under *in vivo* conditions and how they modulate neuronal firing and subthreshold activity. An excitatory effect would promote spikelet generation, since the synaptic input would selectively depolarize the AIS. Inhibition at the AIS is expected to act differently than somatic inhibition. For example, Rojas et al. (2011) found in hippocampal dentate granule neurons that activating the somatic $GABA_A$ receptors strongly reduced somatic input resistance and thus the amplitudes of individual EPSPs. In contrast, activation of AIS $GABA_A$ receptors increased the firing threshold without a significant effect on input resistance (Fig. 2.12).

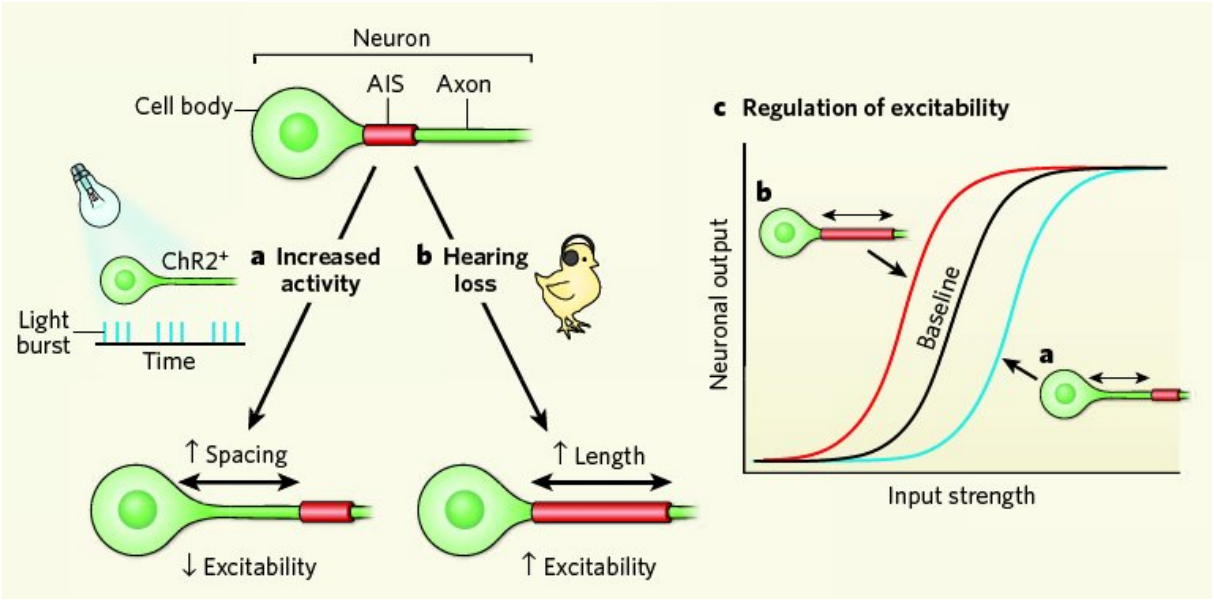

Figure 2.11: Intrinsic plasticity of the axon initial segment.
a: Grubb and Burrone (2010a) have shown that artificially increased neuronal activity (here induced by light stimulation of cultured hippocampal neurons, which express the light-activated channelrhodopsin-2) moved the AIS further away from soma, and reduced neuronal excitability. **b**: Kuba et al. (2010) have demonstrated that the AIS of auditory neurons from nucleus magnocellularis was prolonged following the input deprivation caused by loss of hearing. This led to an increase in neuronal excitability. **c**: Summary of the findings from **a** and **b**: plasticity of the AIS position and length allows to regulate neuronal excitability. Reprinted by permission from Macmillan Publishers Ltd: Nature, Gründemann and Häusser (2010), ©(2010), all rights reserved.

To summarize, the axon initial segment is a highly specialized structure, which can be activated and regulated independently from the soma. This can promote the generation of orthodromic spikelets, originating at the AIS like regular APs, but failing to elicit a somatic action potential. Such spikelets are characterized by relatively fast (max. $dV/dt > 10$ V/s) and large (up to $20 - 30$ mV) waveforms due to the large sodium currents evoked at the AIS. Unlike spikelets originating in dendritic spikes, axonal spikelets can occur at high frequencies because of the shorter refractory period of the axon in comparison to the soma. And finally, the generation of axonal (AIS) spikelets is dependent on the somatic membrane voltage due to the close proximity of the AIS. Spikelets with these properties were reported in several *in vivo* studies (Fig. 2.1 A and B; Spencer and Kandel, 1961; Wong and Stewart, 1992; Crochet et al., 2004; Epsztein et al., 2010; Chorev and Brecht, 2012), although none of them implied an axonal origin of spikelets. It seems that the generation of spikelets upon dendritic inputs is an important factor

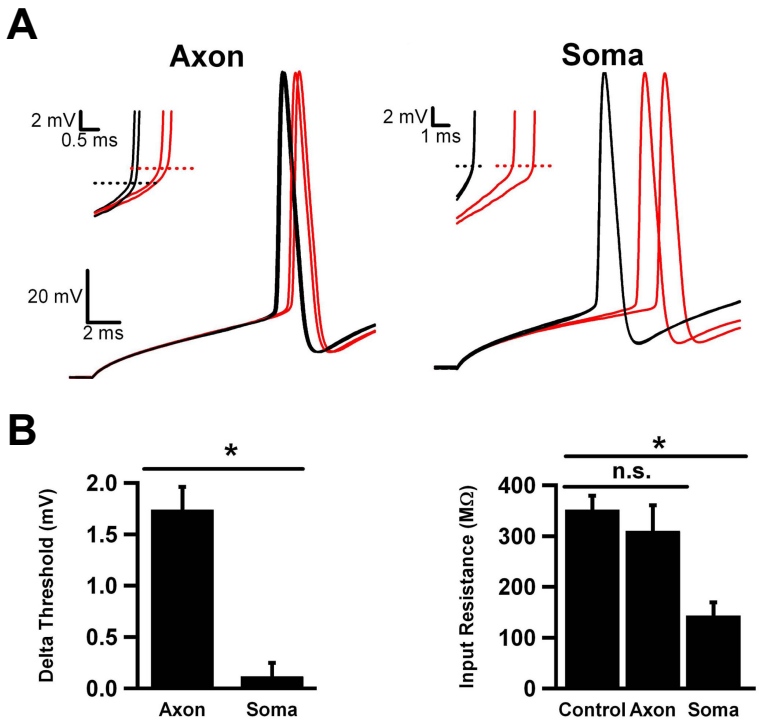

Figure 2.12: Differential effects of somatic and AIS inhibition on neuronal excitability.
A: APs evoked with somatic current injections in the presence (red) and absence (black) of inhibition. Left: Moderate activation of $GABA_A$ receptors at the AIS (red traces) increased the somatic firing threshold (horizontal dotted lines in the inset). The subthreshold depolarization was unaffected by the presence of inhibition, indicating that the somatic input resistance is not altered by AIS inhibition. Right: Activation of $GABA_A$ receptors at the soma significantly decreased input resistance, but did not affect firing threshold (horizontal dotted lines in the inset). **B**: Quantification of the results shown in **A**. Left: change in the somatic spiking threshold for the presence vs. absence of inhibition at the AIS ("Axon") and at the soma. Right: Somatic input resistance without inhibition ("Control"), for AIS inhibition ("Axon"), and for somatic inhibition. Reprinted from Rojas et al. (2011), all rights reserved.

misleading the interpretation. As discussed above, the study by Stuart et al. (1997) demonstrated in neocortical pyramidal neurons directly that dendritic spikes can first initiate an AP at the AIS, which then triggers a somatic AP. Also recent studies in turtle pyramidal neurons (Larkum et al., 2008) and CA1 pyramidal neurons (Apostolides et al., 2016) suggest that dendritically evoked spikelets might originate in axonal APs. Spikelets associated with dendritic plateau-driven potentials in CA1 pyramidal neurons do not occur in an all-or-none manner and have been postulated to be initiated not in the AIS, but further down in the axon, where the sodium channels are not affected by the strong somatic depolarization resulting in inactivation of proximal sodium channels (Apostolides et al., 2016). Orthodromically evoked spikelets of axonal origin would have interesting functional consequences: the ability to generate output APs without firing an AP in the large somato-dendritic compartments would reduce the energetic costs of AP propagation (Ashida et al., 2007) and would allow to control dendritic plasticity triggered by backpropagating APs (Spruston et al., 1995).

Antidromic axonal spikelets can easily be triggered by distal axonal stimulation *in vitro*, but it is not clear whether they also occur spontaneously *in vivo*. Besides a subpopulation of cortical interneurons, where antidromic APs and antidromic spikelets are generated in response to naturally occuring input patterns (Sheffield et al., 2010), antidromic spikelets – also called "ectopic" – are typically reported in pyramidal neurons under various artificial or pathological conditions like epilepsy (Avoli et al., 1998). These antidromic spikelets are characterized by an abrupt rise from the baseline without an underlying depolarization, and unlike orthodromic spikelets, they persist also during moderate somatic hyperpolarization. However, antidromic-like spikelets would also result from axo-axonic coupling by gap junctions, which has been proposed for adult cortical pyramidal neurons (Schmitz et al., 2001; Hamzei-Sichani et al., 2007) and is reviewed in the following section, along with somato-dendritic gap junction coupling.

2.4 Spikelets resulting from electrotonic coupling by gap junctions

Another possibility for spikelet generation provides direct electrotonic coupling between pairs of neurons mediated via specialized structures called gap junctions. If two cells are coupled by such an electrical synapse, an AP occurring in one cell is transmitted through the gap junction and appears as a spikelet in the other cell.

Unlike chemical synapses, electrical synapses are reciprocal, enabling passive current flow in both directions, depending on the potential gradient between the two connected compartments. The strength of electrotonic coupling, called *coupling coefficient*, is defined as the ratio of voltage change between the prejunctional and the postjunctional cell. The coupling coefficient does not only depend on the junctional conductance g_j, but also on the membrane properties of the postjunctional neuron. Accordingly, the postjunctional membrane acts as a low-pass filter: the transmitted current first flows through the membrane capacitance, and as the capacitance gets charged, the current starts to flow through the membrane resistance. Consequently, slow fluctuations of membrane potential are transmitted more effectively than fast signals like APs, which appear in the postjunctional cell as spikelets with slowed time-courses and attenuated amplitudes (Fig. 2.13 A). Although the transmission of signals through gap junctions is immediate, an apparent delay can result from the time needed for capacitive loading of the postjunctional membrane to a detectable level (Bennett and Zukin, 2004).

In the mammalian brain, gap junctions were first demonstrated by Sloper (1972) as dendro-dendritic or dendro-somatic close membrane appositions with a dense, seven-layered structure (Fig. 2.14). Later work has revealed that gap junctions consist of clusters of channels directly connecting the intracellular space of the two coupled neurons such that ions and small metabolites can pass through. Vertebrate gap junction channels are composed of proteins called *connexins*. Six connexin subunits constitute a hemmichannel called *connexon*, which is provided by

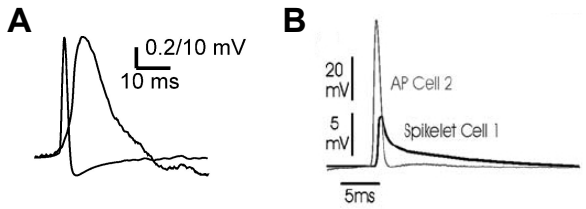

Figure 2.13: Spikelets in electrotonically coupled cells.
A: AP (briefer event) and the corresponding spikelet (wider event) recorded in a coupled pair of hippocampal stratum oriens interneurons. Amplitudes are scaled for a better comparison of their time-course. Reprinted from Zhang et al. (2004), with permission of John Wiley and Sons, all rights reserved. **B**: AP and the corresponding spikelet from a pair of CA1 pyramidal neurons. Amplitudes are scaled, but the short (< 1 ms) time delay is as recorded experimentally Reprinted from Mercer et al. (2006), with permission of Springer, all rights reserved.

each of the two connected cells to form a functional gap junction (Fig. 2.15). In rodents and humans, around 20 isoforms of connexins exist, forming gap junctions in many different tissues. Although about half of the connexins is present in the central nervous system, most of them are not expressed in neurons, but in astrocytes and oligodendrocytes (Willecke et al., 2002). Connexin 36 (Cx36) appears to be the only neuron-specific gap junctional protein. Experimental data indicate that Cx36 promotes electrotonic coupling in various brain regions including hippocampus and neocortex (Connors and Long, 2004).

In the adult brain, gap junctions have been thoroughly demonstrated to connect hippocampal and neocortical interneurons of the same type (reviewed, e.g., in Galarreta and Hestrin, 2001). First, dual recordings identified coupled pairs, where a subthreshold current injection or an AP in one cell resulted in a voltage change or a spikelet waveform, respectively, in the other cell. Next, anatomical studies delivered ultrastructural evidence for the existence of dendrodendritic or dendro-somatic gap junctions as early as in the 1970s (Sloper, 1972). And finally, molecular studies revealed that interneuron gap junctions are composed of connexin 36. The coupling between interneurons was found abundant, but rather weak, and the spikelet waveforms resulting from AP transmission through these electrical synapses exhibit small amplitudes (typically < 1 mV) and slow dynamics (Fig. 2.13 A).

In contrast, much controversy accompanies the notion of electrical coupling between cortical pyramidal cells. Here, the evidence is rather indirect, mostly comprised of dye coupling data (based on gap junctional permeability for small tracer molecules such as neurobiotin, biocytin or Lucifer yellow), and pharmacological modulation of spikelet occurrence and waveform. Up to date, only few studies demonstrated direct electrical coupling in pairs of hippocampal (Schmitz et al., 2001; Mercer et al., 2006) and neocortical (Wang et al., 2010) pyramidal neurons, and one study provided anatomical evidence for the presence of gap junctions between mossy fiber axons in the dentate gyrus (Hamzei-Sichani et al., 2007). Moreover, the protein underlying the electrical coupling in pyramidal neurons remains unknown. The spikelet waveforms found in dual recordings of pyramidal cells are substantially larger ($2 - 20$ mV) and faster than the waveforms typical of interneuron spikelets (Fig. 2.13 B), and resemble the spikelet waveforms recorded in pyramidal neurons *in vivo* (Fig. 2.1 A and B). Furthermore, unlike interneuron spikelets, spikelets in pyramidal neurons are abolished when the sodium channels of the recorded neuron are blocked intracellularly with QX314, which suggests that these spikelets propagate actively in the putative postjunctional neuron. Consistent with the fast spikelet waveform and active propagation in the recorded neuron is axo-axonal coupling, which has been suggested in some studies (Schmitz et al., 2001; Wang et al., 2010), but not in

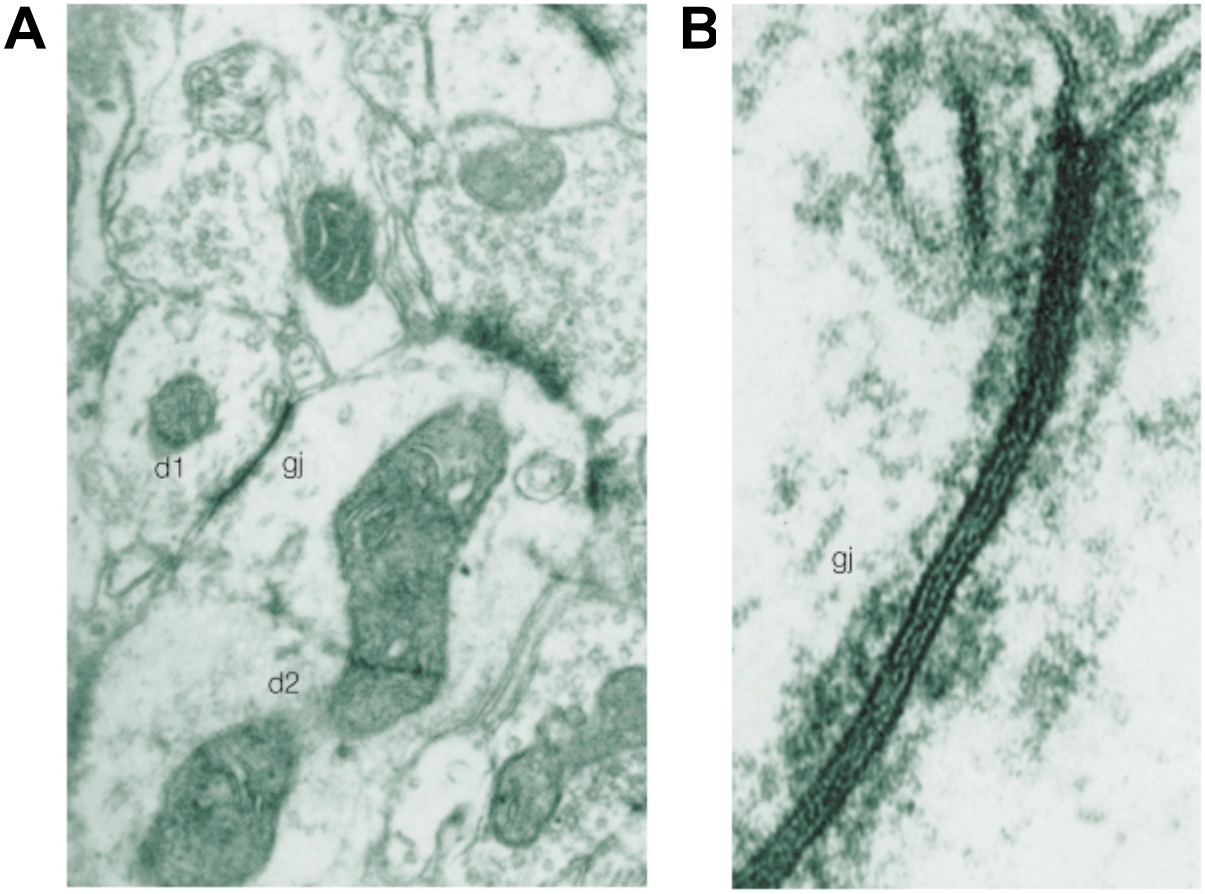

Figure 2.14: Gap junctions between dendrites of cortical interneurons, visible on electron micrographs.
A: A gap junction (gj) between dendrites (d1 and d2) of two interneurons from adult primate neocortex. Magnification: $29,000\times$. **B**: A higher magnification of the gap junction reveals its multi-layered structure and associated dense material in the cytoplasm. Magnification: $250,000\times$. Reprinted from Sloper and Powell (1978), by permission of the Royal Society, all rights reserved.

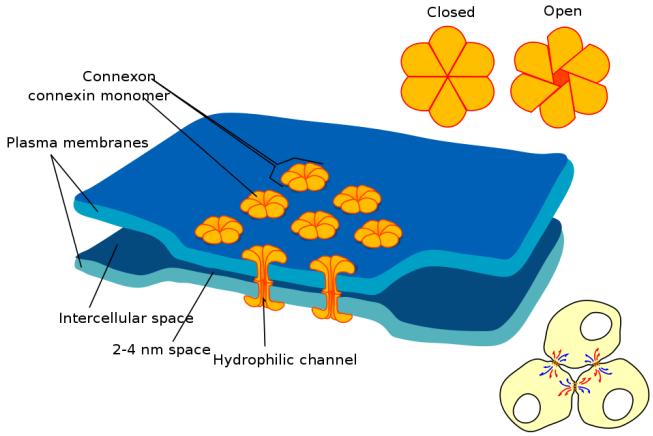

Figure 2.15: Schematic illustration of gap junctional ultrastructure.
Gap junctions connect the intracellular spaces of two cells by hydrophilic channels composed of connexin proteins. Six connexins build a hemichannel called connexon that is provided by each of the two cells. The gap junction can open and close by changing the configuration of the connexins. From `https://en.wikipedia.org/wiki/File:Gap_cell_junction-en.svg` by LadyofHats, public domain.

others (Mercer et al., 2006).

This rather scarce evidence of gap junctional coupling in pyramidal neurons is further weakened by inherent issues associated with the methods used to demonstrate gap junctional coupling. First, the paired recordings are typically performed with sharp electrodes as these allow successive penetration of many neurons before they get clogged and have to be exchanged. However, sharp electrodes are prone to the so-called "shish-kebap artifact", where the recording electrode would penetrate more neurons at the same time and introduce artifactual coupling (Bennett and Pereda, 2006). This problem also affects dye coupling experiments, where further artifacts might occur due to, for example, dye leakage into the extracellular space that can be taken up by adjacent neurons (Jefferys, 1995).

In general, the relation between electrotonic coupling and dye coupling is not very clear. For instance, Knowles et al. (1982) reported frequent spread of Lucifer yellow into non-injected CA1 pyramidal neurons *in vitro*. They did not find electrotonically coupled cell pairs nor did they observe spikelets in their recordings. Andrew et al. (1982), also using Lucifer yellow and recording with sharp electrodes from CA1 pyramidal cells, showed that spikelets and dye coupling can occur independently. The opposite effect has also frequently been observed: interneurons are rarely dye coupled, whereas their electrotonic coupling via Cx36 gap junctions is now well established (Bennett and Zukin, 2004). Gutnick et al. (1985) demonstrated that the occurence of dye coupling might also result from the slicing procedure. These authors did not observe dye coupling in tangential slices, but they did observe it in radial neocortical slices, where greater damage to dendritic trees can be expected. They proposed that the observed coupling might occur as a specific reaction of the neurons to the injury, by strenghtening of existing and/or formation of new gap junctions (Belousov and Fontes, 2013). However, the possibility of artifactual coupling due to fusion of cut neuronal processes can not be completely excluded (Buzsáki, 2001). Such an artificial fusion of neuronal processes would induce apparent electrical coupling, which would have serious implications for the interpretation of the dual recording data. These concerns seem indeed justified as paired recordings in hippocampal (Mercer et al., 2006) and neocortical (Wang et al., 2010) pyramidal neurons demonstrated electrical and dye

coupling in cells with somata located very close to each other (Fig. 2.16 and 2.17), but the close membrane appositions found at proximal somato-dendritic sites did not show any "distinctive structures indicative of a gap junction" (Fig. 2.16; Mercer et al., 2006).

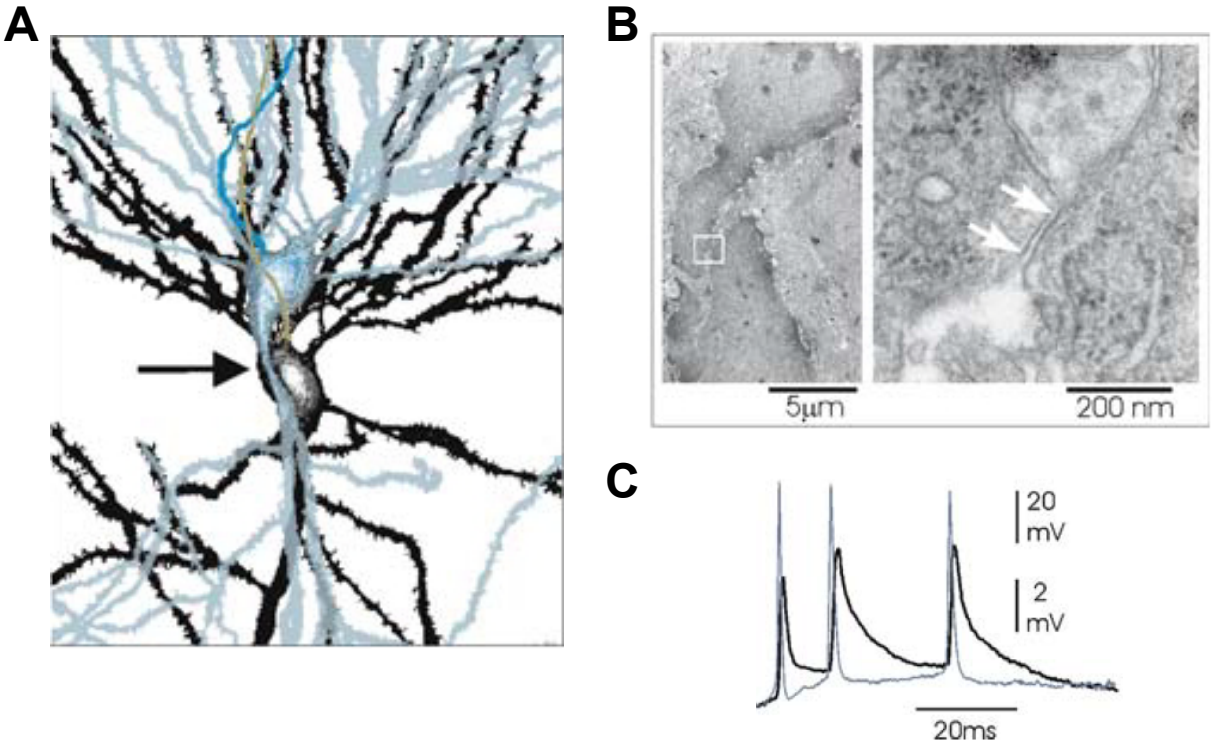

Figure 2.16: Electrical coupling in CA1 pyramidal neurons *in vitro*.
A: Reconstruction of an electrically coupled pair of neurons. The arrow marks a putative contact between the apical dendrite of one cell (blue) and the soma of the other cell (black). **B**: Left: Electron micrograph depicting the cells from A (proximal apical dendrite of the blue cell and both somata). The white box indicates the region of the putative contact site, which is expanded on the right. Note that the close membrane apposition, marked with white arrows, does not show any distinctive ultrastructure. **C**: Demonstration of electrical coupling in the two cells shown in A and B: APs in the blue cell (thin blue-gray traces) evoked spikelets in the black cells (black traces). Reprinted from Mercer et al. (2006), with permission of Springer, all rights reserved.

Up to now, the only study providing direct ultrastructural evidence for gap junctions in cortical excitatory neurons has been published by Hamzei-Sichani et al. (2007). In thin-section transmission electron micrographs, the authors found altogether ten close appositions of dentate granule axons called mossy fibers. Nonetheless, these putative gap junctions were missing the typical "submembrane densities" and showed a pentalaminar instead of heptalaminar structure (Fig. 2.18, A and B). A further instance of a presumed axonal gap junction could be detected by freeze-fracture replica immunogold labeling (FRIL) using anti-Cx36 immunogold beads. However, it could not be determined whether the labeled axon was coupled to another axon or to a dendritic spine (Fig. 2.18, C and D). Moreover, other studies did not find connexin 36 in pyramidal neurons (Hormuzdi et al., 2001; Pais et al., 2003).

Much more commonly, gap junctional coupling is inferred from modulatory effects of pH and pharmacology, although the effects of these manipulations are not specific to gap junctions (Connors and Long, 2004). In general, decreased intracellular pH (i.e., acidification) tends to close gap junctions, whereas increased intracellular pH (i.e., alkalization) opens gap junctions

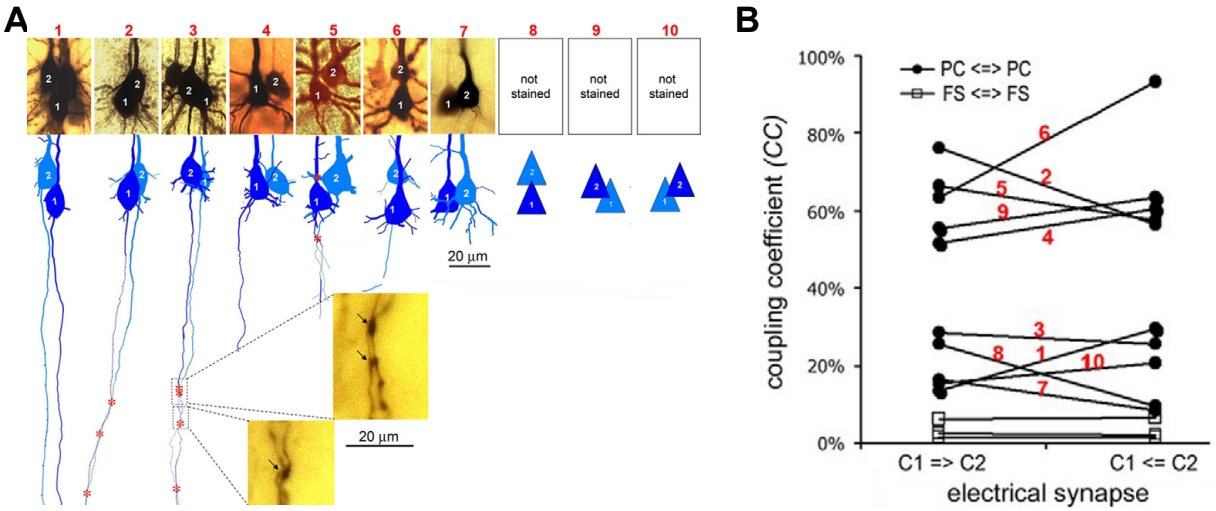

Figure 2.17: Electrical coupling in neocortical pyramidal neurons *in vitro*.
Morphologies (**A**) and coupling coefficients (**B**) of ten coupled pairs of neocortical pyramidal neurons. In **A**, red asterisks mark possible coupling sites and insets show putative axo-axonal contacts. **B** depicts the coupling coefficients (CCs) in both directions (cell 1 to cell 2, C1→C2, and cell 2 to cell 1, C2→C1) for all 10 pairs from **A**. Three fast-spiking (FS) interneurons are included for comparison. The CCs were determined for step-currents (No. 2,3,6,10) or spikelet and AP transmission (No. 1,4,5,7-9). Reprinted from Wang et al. (2010), used under the Creative Commons Attribution licence. To view a copy of this licence, visit `https://creativecommons.org/licenses/by/4.0/`.

and strengthens electrical coupling (Connors and Long, 2004). However, pH levels have been shown to regulate not only gap junctions, but various membrane channels as well. Moreover, the physiological regulation of neuronal pH appears to be homeostatic: neuronal activity leads to acidosis, which in turn diminishes the excitability of neurons. Elevated pH has the opposite effect of increasing neuronal excitability (Chesler, 2003).

There are various pharmacological agents shown to modulate the strength of electrotonic coupling. These are chemically diverse and include long-chain alcohols such as heptanol or octanol, the anesthetic halothane, carbenoxolone, and mefloquine. However, most of these substances act non-specifically and have been shown to influence other physiological properties of neurons as well (Connors and Long, 2004). The specificity of carbenoxolone is controversial, with some studies reporting no influence on intrinsic neuronal properties (Schmitz et al., 2001), while others found reduction of various membrane conductancies, incresed AP threshold or decreased input resistance (Rouach et al., 2003; Tovar et al., 2009). The quinine derivate mefloquine has recently gained interest as a specific and potent blocker of Cx36 channels, but also here some side-effects have been reported (Cruikshank et al., 2004). Yet it needs to be considered that if pyramidal cells are coupled at axonal sites, the transmitted AP is propagated actively in the axon of the postjunctional cell and the propagation failure occurs close to the soma. Therefore, the pharmacological modulation of spikelet amplitude unlikely reflects a modulation of axo-axonal gap junction itself, but rather a change of some other neuronal property.

To address the question whether electrotonic coupling occurs in pyramidal neurons *in vivo*, Chorev and Brecht (2012) performed dual intra- and extracellular recordings of CA1 pyramidal neurons in anesthetized rats. The authors identified an extracellular AP waveform associated with, and slightly preceding the onset of intracellular spikelets. In chapter 4, I simulated extra-

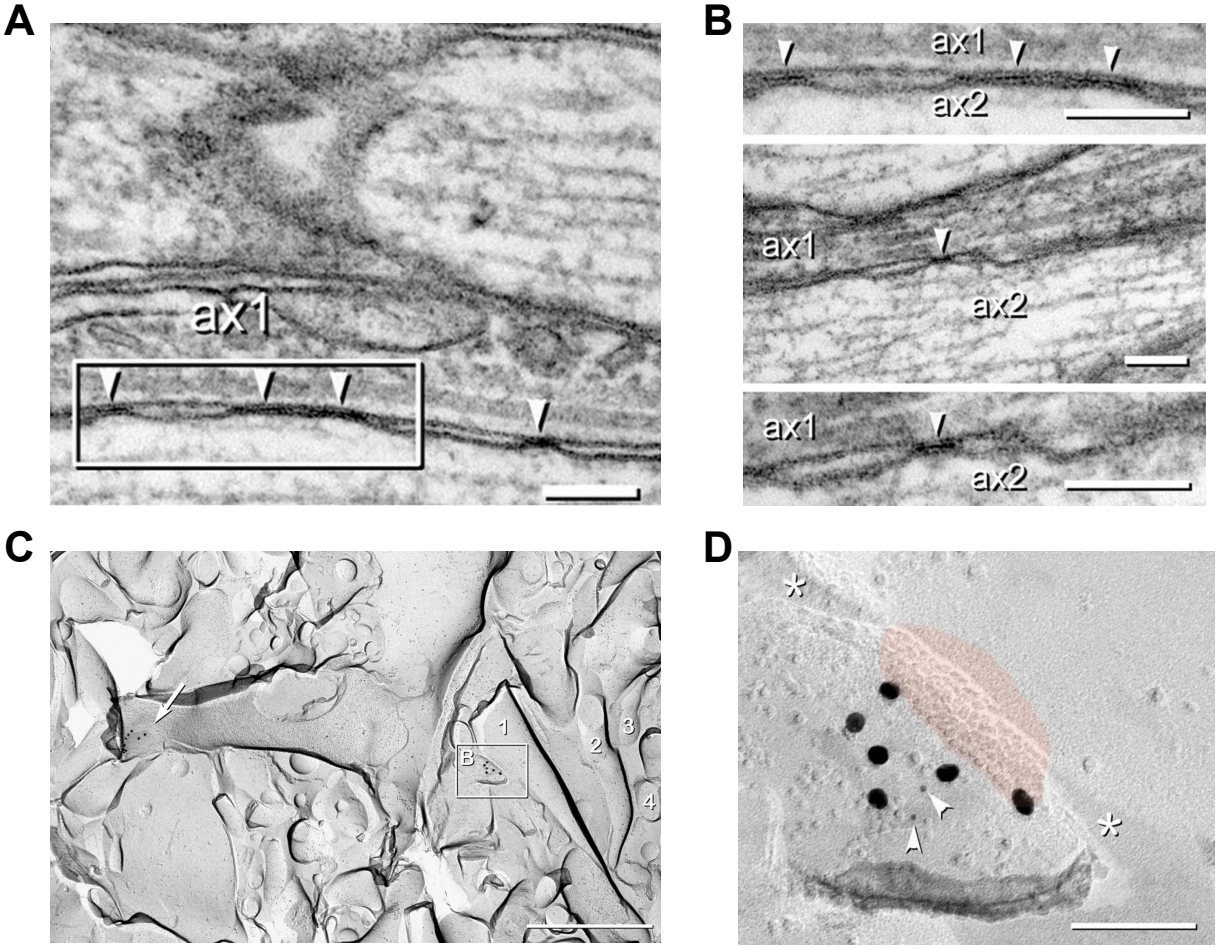

Figure 2.18: Ultrastructural evidence for axonal coupling in mossy fiber axons.
A and **B**: Electron micrographs with several gap junctions (arrowheads), located between a pair of axons (ax1 and ax2). **C**: FRIL electron micrograph reveals a dendritic (arrow) and axonal (Box B) gap junction. The axonal site is shown in detail in **D**. It was labeled by six 18-nm gold beads and two 6-nm gold beads (arrowheads). The red overlay marks the presumed gap junction, and asterisks label the narrowed extracellular space at the gap junction. (Scale bars: 1 μm in A and 100 nm in B-D.) Reprinted with permission from Hamzei-Sichani et al. (2007),

cellular waveforms of APs and spikelets in compartmental models of pyramidal neurons and found that electrotonic coupling can account for all aspects of the data only for an axonal gap junction and a large (ca. $> 140\mu$m) distance between the somata of the coupled cells, such that only the intracellularly recorded cell shapes the extracellular waveform.

To summarize, there is a large body of evidence supporting gap junctional origin of spikelets in local GABAergic interneurons. These interneurons are frequently, but weakly coupled by Cx36-channels at dendritic, somatic or dendro-somatic coupling sites. This coupling gives rise to small and slow spikelets, which propagate passively. In contrast, only few *in vitro* studies have directly shown that spikelets in cortical pyramidal neurons can result from electrotonic coupling and anatomical evidence for gap junctions is even scarcer. Theoretical as well as some experimental studies have suggested an axonal coupling site, which could account for the relatively high amplitudes, fast time-course, and active propagation of these spikelets. Spikelets generated by axo-axonal coupling are similar to antidromically evoked axonal spikelets discussed in the previous section, since the transmitted AP propagates antidromically in the postjunctional axon and the propagation failure occurs close to the soma. Weak dendro-dendritic and dendro-somatic gap junctions in cortical interneurons were shown to significantly contribute to the generation and maintenance of network oscillations, for example in the gamma range, by promoting neuronal firing synchrony (Bennett and Zukin, 2004). Theoretical studies suggested that axo-axonal coupling of pyramidal neurons could underlie the generation of high-frequency oscillations such as hippocampal sharp wave-ripples (Traub et al., 1999). However, recent experimental studies suggest that local inhibitory synaptic interactions give rise to sharp-wave ripples *in vitro* (Schlingloff et al., 2014) as well as *in vivo* (Stark et al., 2014).

2.5 Spikelets produced by ephaptic coupling

Ephaptic coupling is a form of electrical coupling between two cells without a specialized connection like a synapse or a gap junction. The term "ephapse" (from greek $\epsilon\phi\alpha\pi\tau\omega$ - to touch) was coined by Arvanitaki (1942) to describe "the locus of contact or close vicinity of the active functional surfaces". Such a close apposition of neuronal compartments enables transmission of electrical signals from one cell to another via extracellular electric fields. Here, I follow the seminal work by Jefferys (1995) and distinguish ephaptic coupling from population field effects, where synchronized activity of many neurons produces large extracellular fields, which influence the membrane voltage of the whole neural population located within the reach of the field. Indeed, the stereotypical spike-like waveforms of spikelets indicate that spikelets originate from individual APs. So when an AP is triggered in one cell, a spikelet waveform might be visible in another cell that has a process running closely to the firing cell.

Unlike the "resistive coupling" by gap-junctions that results in slow, low-pass filtered spikelets, the nature of ephaptic AP transmission is capacitive: there is no transmembrane current flow, but the charge is redistributed on the intra- and extracellular surfaces of membranes (Valiante et al., 1995; Vigmond et al., 1997; Weiss and Faber, 2010). Consequently, the AP waveforms are high-pass filtered, and ephaptic spikelets appear brief, typically briefer than the underlying APs (Vigmond et al., 1997). The hallmark of ephaptic spikelets is a fast decay – similarly fast as their rising phase – and frequently observed biphasic shape (i.e., depolarizing phase followed by a hyperpolarizing phase), which clearly distinguishes ephaptic spikelets from all other types of spikelets.

Such brief spikelets were observed in CA1 pyramidal neurons *in vitro* during calcium-free-induced epileptic activity where in every cell the amplitudes of spikelets occurred in $2-4$ well-defined clusters (Valiante et al., 1995; Fig. 2.1 D). Another example of putative ephaptic

spikelets provides the study by Scholl et al. (2015), which found that spikelets in cat visual cortex *in vivo* shared some, but not all, sensory selectivities with the APs recorded in the same cell (Fig. 2.1 C).

Amplitudes of these somatically recorded spikelets were several millivolt large ($1 - 6$ mV), which agrees with theoretical and modeling predictions for transmembrane voltage changes due to ephaptic AP transfer from a soma to a neuronal cable (Holt and Koch, 1999). However, Vigmond et al. (1997) noted that, in a passive model of a CA3 pyramidal neuron, the amplitudes measured intracellularly were an order of magnitude smaller (< 0.1mV) than the induced transmembrane potentials. Holt and Koch (1999) pointed out that ephaptically generated transmembrane potentials do not spread electrotonically "unless there are active channels at the location of the ephaptic depolarization". Fast sodium currents active at subthreshold potentials could, in principle, boost the intracellular amplitudes of spikelets. Vigmond et al. (1997) alternatively proposed that intracellular spikelet amplitudes of several millivolts might be achieved by synchronized firing of several close-by neurons. This is conceivable for epileptic activity (Valiante et al., 1995), but rather unlikely to occur under physiological *in vivo* conditions (Scholl et al., 2015).

In general, ephaptic interactions are weak even for cells that are very close (3 nm apart in the model of Vigmond et al., 1997) because the AP waveform is transmitted through the low-resistance extracellular medium. Consistently, increased extracellular resistance has been shown to promote ephaptic coupling: Jefferys (1995) reviewed experiments with squid giant axons, where even APs could be evoked in an ephaptically coupled axon if the two nearby axons were immersed in mineral oil, which acts as an insulator and thus increases extracellular resistance. The physiological extracellular resistance is largest in brain regions with densely packed cells and restricted extracellular space like in rat hippocampus, especially in the CA1 cell body layer, which has double the resistivity of the surrounding layers (Gold et al., 2006). Moreover, the extracellular space is not constant over time, but shrinks with intense neuronal activity that results in tissue swelling (Fox et al., 2004; Weiss and Faber, 2010). This might explain the occurrence of ephaptic spikelets in CA1 pyramidal neurons under epileptic conditions. However, neocortical tissue is less densely packed and the *in vivo* activity is incomparable to epileptic states. So it is not immediately clear how ephaptic spikelets of several millivolts in amplitude can be generated in neocortical cells as observed by Scholl et al. (2015).

Further theoretical studies are needed to examine ephaptic coupling in active models and to identify factors that might result in relatively large spikelet amplitudes in the millivolt range. One of these factors are probably fast sodium currents. However, subthreshold sodium currents are mainly located in the axons of pyramidal cells (Fleidervish et al., 2010), whereas cable theory posits that the induced voltage change is smaller in thin cables like axons than in thicker cables like dendrites (Holt and Koch, 1999). Moreover, it needs to be considered that the intracellular spikelets are typically measured in the soma or in the proximal apical trunk, so spikelets evoked in distal cables would get low-pass filtered when propagating passively to the soma. Future studies should also assess the effect of activity-dependent tissue swelling on ephaptic coupling and the occurrence of spikelets (Jefferys, 1995; Weiss and Faber, 2010). And finally, the potential functional role of ephaptically induced spikelets needs to be understood. Similarly to population field effects, ephaptic coupling could synchronize the firing of close-by neurons, but without the influence on the whole network. However, it is also possible that ephaptic spikelets are an epiphenomenon – and, at best, an indicator – of a certain network state.

2.6 Conclusions

In this chapter, I have reviewed the various spikelet generating mechanisms with the aim to understand the origin of spikelets in pyramidal neurons. I noted that at least two qualitatively different types of spikelets appear in the experimental literature. One spikelet type is defined by a very brief time course (width at half-amplitude < 0.5 ms), which fits well to theoretical predictions of waveforms transmitted ephaptically through extracellular fields. However, more reports are on spikelets of another type, which exhibit relatively large amplitudes (up to 20 mV) and fast rise times (max. dV/dt of $10 - 40$ V/s). Several lines of evidence point to an axonal origin within a single neuron, especially the short inter-spikelet-intervals, its large and fast waveform, its dependence on membrane polarization, and active conductance within the recorded neuron. And finally, dual and triple recordings from dendrites, somata and axons of pyramidal neurons directly demonstrated that somatic spikelets are associated with axonal APs, but not dendritic spikes. Nevertheless, there is also some evidence suggesting that spikelets in pyramidal neurons are generated through electrical coupling by gap junctions. The waveforms of experimentally recorded spikelets fit to axonal coupling sites. However, the existence of axo-axonal gap junctions is still highly controversial.

In the following chapters, I present my simulation results investigating the generation of spikelets in pyramidal neurons. In chapter 3, I examine the conditions of orthodromic spikelet generation in a single cell. These spikelets are initiated as an AP in the axon initial segment, which fails to trigger a somatic AP. In chapter 4, I compare my simulated extracellular waveforms of APs and spikelets to the experimental data, with the aim to constrain possible spikelet mechanisms. There, I consider spikelets generated at the AIS of a single cell as well as spikelets generated through gap-junctional coupling at dendritic, somatic, and axonal coupling sites.

3 Single-cell mechanism of spikelet generation

Spikelets are small spike-like depolarizations that can be measured in somatic intracellular recordings. Their origin in pyramidal neurons remains controversial. To explain spikelet generation, we propose a novel single-cell mechanism: somato-dendritic input generates action potentials at the axon initial segment that may fail to activate the soma and manifest as somatic spikelets. Using mathematical analysis and numerical simulations of compartmental neuron models, we identified four key factors controlling spikelet generation: (1) difference in firing threshold, (2) impedance mismatch, and (3) electrotonic separation between the soma and the axon initial segment, as well as (4) input amplitude. Because spikelets involve forward propagation of action potentials along the axon while they avoid full depolarization of the somato-dendritic compartments, we conjecture that this mode of operation saves energy and regulates dendritic plasticity while still allowing for a read-out of results of neuronal computations.[1]

3.1 Introduction

Brain functions rely on computations in single neurons, but some basic features of neural processing still remain unclear. Here, we focus on spikelets, which are brief, spike-like depolarizations of small amplitude (< 20 mV). Spikelets can be measured in somatic intracellular recordings in diverse neuron types, including cortical interneurons (e.g., Galarreta and Hestrin, 1999) and pyramidal cells (Epsztein et al., 2010; Harvey et al., 2009; Crochet et al., 2004). Due to their all-or-none appearance and spike-like shape, spikelets are considered to reflect action potentials (APs) occurring in electrotonically distinct compartments. These APs might originate either in the dendrites or in the axon of the same cell, or in another neuron that is either coupled ephaptically or through gap junctions. Since spikelets influence somatic voltage dynamics, including AP generation (Epsztein et al., 2010), identifying the origin of spikelets is important for understanding neural computations.

The origin of spikelets in hippocampal (Chorev and Brecht, 2012; Epsztein et al., 2010; Harvey et al., 2009) and neocortical (Crochet et al., 2004) pyramidal neurons is not well understood. The original hypothesis of spikelets resulting from dendritic spikes (Spencer and Kandel, 1961) could not be supported by subsequent studies (Golding and Spruston, 1998). Instead, axo-axonal (Schmitz et al., 2001; Hamzei-Sichani et al., 2007) and somato-dendritic (Mercer et al., 2006; Wang et al., 2010) gap-junction coupling of pyramidal neurons has been suggested as the spikelet origin, however, the supporting experimental evidence is scarce, raising the question whether there are other mechanisms for generating spikelets in pyramidal neurons.

In vitro, somatic spikelets can be evoked with distal axonal stimulation if an antidromically propagating AP (Dugladze et al., 2012) does not suffice to activate the somatic sodium channels. This can happen because of somatic hyperpolarization, (prolonged) somatic depolarization, or fast repeated axonal stimulation (Coombs et al., 1955, 1957a; Kandel et al., 1961; Hu et al., 2009). However, *in-vivo* inputs are usually considered to arrive at the soma orthodromically. Indeed, spontaneous antidromic spikelets (also called "ectopic") have been identified

[1] The content of this chapter has been submitted for publication and is currently under revision:
Michalikova M, Remme M, Kempter R: *Spikelets in pyramidal neurons: Action potentials initiated in the axon initial segment that do not activate the soma.* M. Remme calculated the analytic results shown in Fig. 3.3. I generated all the other results and wrote the text.

mainly under pathological conditions, such as epilepsy (Avoli et al., 1998). Additionally, antidromic spikelets are expected to occur when neurons would be coupled through axo-axonal gap junctions (Schmitz et al., 2001).

Here, we present a novel hypothesis for the origin of spikelets in pyramidal neurons. Using a computational approach, we demonstrate that spikelets can be evoked orthodromically with somato-dendritic inputs, which initiate APs at the distal axon initial segment (AIS). Under certain conditions, these APs in the AIS fail to fully activate the soma and appear there as spikelets. Consequently, the possibility of a forward propagating AP without it propagating back to the soma and into the dendrites presents a powerful mechanism for control of dendritic plasticity while ensuring the read-out of neural computations.

3.2 Methods

Detailed compartmental model

For the results in Figs 3.1, 3.6, 3.7 and 3.8 we used a previously published detailed model of a reconstructed layer V pyramidal neuron (ModelDB accession number 123897; Hu et al., 2009), implemented in NEURON (Carnevale and Hines, 2006). Compared to the original model, we made two modifications. First, a small geometrical discontinuity at the AIS was corrected. In the original model, the AIS tapers from 1.7 μm to 1.22 μm. However, the diameter at the end of the axon hillock, i.e., at the hillock-AIS boundary, is 1.3 μm. We removed this sudden jump in the diameter so that the diameters at the end of the axon hillock and at the beginning of the AIS are equal at a value of 1.3 μm (then tapering smoothly to 1.22 μm, at the end of AIS). Second, the density of the $Na_V1.2$ subtype was decreased in soma, axon hillock, and AIS to 80%, and in dendrites to 60% of the original values. These changes only weakly influenced the AP properties and firing patterns (Table 3.1). The largest effects were observed for spikelet frequency and maximum AP slope. The decrease in maximum AP slope was desired, as it reflects the smaller AP slopes reported *in vivo*. Overall, the properties of APs generated in this model (Table 3.1) fit well into the range reported for pyramidal neurons in the experimental literature (Epsztein et al., 2010; Chorev and Brecht, 2012; Naundorf et al., 2006; Kole et al., 2007; Palmer and Stuart, 2006).

Table 3.1: Comparison of AP- and spikelet-firing properties in the original model and in the adapted model used in Fig. 3.1.

Model properties	**Original model**[1]	**Original gNa + corrected diam**	**Adapted model**[2]
AP threshold (kink)* [mV]	-49.87	-50.01	-50.31
AP amplitude* [mV]	92.54	92.97	85.99
AP width at half amplitude* [ms]	0.71	0.71	0.78
Max. AP dV/dt* [mV/ms]	349.53	359.22	261.82
AP firing rate# [APs/s]	6.57	6.57	5.79
Spikelet firing rate# [spikelets/s]	0	0.04	0.63
std(Vm@soma)#° [mV]	8.51	8.52	8.09

[1] original model Hu et al. (2009): original Na channel densities (gNa) and diameter discontinuity at hillock - AIS boundary
[2] adapted model used in Fig. 3.1: reduced Na channel densities (gNa) and corrected diameter discontinuity as described in the Methods
* single APs evoked with somatic current pulses (1 nA for 10 ms)
# 100 s simulation with stochastic synaptic conductances like in Fig. 3.1
° standard deviation of somatic membrane voltage

The compartmental model cell was stimulated with two fluctuating synaptic point conductances placed at the soma (ModelDB accession number 8115; Destexhe et al., 2001) with the following parameters (values given in parentheses): reversal potential of the excitatory ($E_e = 0$ mV) and inhibitory ($E_i = -75$ mV) conductance, average excitatory ($g_{e0} = 0.01$ μS) and inhibitory ($g_{i0} = 0.0573$ μS) conductance, standard deviation of the excitatory ($\text{std}_e = 0.014$ μS) and inhibitory ($\text{std}_i = 0.02$ μS) conductance and time constant of the excitatory ($\tau_e = 2.728$ ms) and inhibitory ($\tau_i = 10.49$ ms) conductance. As a result, the somatic membrane voltage fluctuated with a standard deviation of 8.09 mV, producing a somatic AP firing rate of 5.79 s^{-1} and a spikelet firing rate of 0.63 s^{-1} (Fig. 3.1).

The somatic APs and spikelets were detected using a voltage-threshold criterion at the AIS

and at the soma (both $-10\mathrm{m}V$). For both types of events, the threshold at the AIS had to be crossed. If the threshold at the soma was crossed within a time window from 1 ms before to 5 ms after the AIS threshold crossing, such an event was classified as an AP. Otherwise, the event was a spikelet. We also used a double-threshold criterion for the somatic voltage derivative (dV/dt) to confirm that no event was missed by the above voltage-threshold criterion and that indeed all somatic APs and spikelets were associated with an AP at the AIS: events that crossed the first threshold (20 V/s), but not the second threshold (100 V/s) were classified as spikelets, whereas somatic APs had to cross both thresholds within 2 ms time.

In Fig. 3.1 E, the APs were aligned in time to the point of crossing a somatic voltage threshold of -10 mV, whereas spikelets were aligned to the point of crossing a voltage threshold of -10 mV at the AIS. In Fig. 3.1 H, all events were aligned to the point of crossing the voltage threshold at the AIS to allow for a comparison of inputs between APs and spikelets. In Fig. 3.1 H, the effective synaptic reversal potential was calculated as $(g_e(t)E_e + g_i(t)E_i)/(g_e(t) + g_i(t))$, i.e., the excitatory and inhibitory reversal potentials weighted with the respective conductances.

In Fig. 3.6, in addition to the somatic conductance inputs as in Fig. 3.1, the model cell was also stimulated with brief current pulses (0.5 nA for 2 ms) delivered every 500 ms at the most distal axonal compartment. Somatic spikelets were classified as orthodromic (i.e., evoked with somatic inputs) or antidromic (i.e., evoked with distal axonal inputs) based on the relative timing of the AP at the distal AIS and in the axon. For orthodromic spikelets, the AP at the distal AIS preceded the AP in the axon; for antidromic spikelets, the AP at the distal AIS followed the AP in the axon.

In Fig. 3.7, the morphology of the model cell was altered: the axon hillock was omitted and the AIS was attached to a basal dendrite ("dendrite3[2](0.5)") 20.5 μm away from the soma. In addition to the somatic conductance inputs as in Fig. 3.1, an EPSG ($\tau_{\mathrm{rise}} = 0.5$ ms, $\tau_{\mathrm{decay}} = 2$ ms, peak conductance = 0.02 μS, $E_{\mathrm{syn}} = 0$ mV) was delivered every 500 ms to the axon-carrying dendrite, distally to the AIS-connecting site ("dendrite3[3](0.1)"). Spikelets evoked with dendritic EPSGs were distinguished from the orthodromic spikelets (evoked with somatic inputs) as spikelets occurring within a 2 ms window after the dendritic EPSG.

In Fig. 3.8, in addition to the somatic conductance inputs as in Fig. 3.1, the model cell was also stimulated with a brief current pulse (2 nA for 1 ms) delivered every 20 ms at the proximal apical dendrite ("dendrite11[2](0)") 47 μm away from soma. In 200 s of simulation 2,106 somatic APs and 91 somatic spikelets were generated. We classified the spikelets as evoked with the dendritic input if the somatic spikelet was evoked within 2 ms from dendritic stimulus onset ($N = 43$); if the spikelet occurred 10 ms or later after the onset of the dendritic stimulus, the spikelet was classified as triggered by the somatic background stimulus ($N = 41$).

In Fig. 3.4, we simulated two identical cells (as in Fig. 3.1) coupled by a gap junction. The gap junction was modelled as an ohmic resistor, allowing to transmit voltage changes between the coupled cells. In cell 1, an AP was evoked with a somatic current step (2 nA applied for 15 ms), and a spikelet was recorded in cell 2. The strength of the gap junction was varied between 22 and 82 MΩ in 5 MΩ steps (corresponding to gap junctional conductance of $12 - 45$ nS). The gap junction was placed at the soma or at several positions along the main apical dendrite (at a distance of $\approx$ 8, 24, 47, 78, or 109 μm from soma). The leak reversal and initial membrane voltages were set to -80 mV instead of the original leak reversal of -70 mV because otherwise the closest and strongest gap junctions could only generate an AP and not a spikelet in cell 2. The amplitude of spikelets was measured from the maximum of the 2nd derivative (the "kink") to the maximum amplitude.

Passive-membrane model of an axonal cable and a somato-dendritic compartment

We mathematically analyzed a model consisting of a semi-infinite cable with an RC-circuit as a boundary condition, representing the axon and the entire somato-dendritic compartment,

respectively (Fig. 3.3). The system is mathematically equivalent to the lumped-soma model introduced by Rall (1960). Our model describes the dynamics of the voltage V along the axon at distance x from the soma in response to current input at location $x = y$ using the linear cable equation:

$$\lambda^2 \frac{\delta^2}{\delta x^2} V(x,t) - \tau \frac{\delta}{\delta t} V(x,t) - V(x,t) = g(x,t) \quad \text{for} \quad x > 0 \tag{3.1}$$

where τ is the membrane time constant (in ms), λ is the axonal length constant (in cm), and $g(x,t)$ is the input to the model. The boundary condition to include the somato-dendritic compartment at $x = 0$ is

$$\tau \frac{\delta}{\delta t} V(0,t) = \lambda \rho \frac{\delta}{\delta x} V(0,t) - V(0,t) \tag{3.2}$$

where the dimensionless parameter ρ denotes the ratio of the total somato-dendritic membrane resistance to the input resistance of the axon. The semi-infinite cable boundary condition is

$$\lim_{x \to \infty} V(x,t) = 0. \tag{3.3}$$

For notational convenience we consider the resting potential in this linear system to be 0 mV. The parameters τ, λ, and ρ are determined by physiological parameters. Setting the specific membrane resistance $R_m = 10^4\ \Omega\,\text{cm}^2$, specific membrane capacitance $C_m = 1\ \mu F/\text{cm}^2$, axial resistivity $R_a = 150\,\Omega\,\text{cm}$, surface area of the somato-dendritic compartment $A_{sd} = 2 \cdot 10^{-4}\,\text{cm}^2$ and diameter of the axon $d_a = 10^{-4}$ cm yields $\tau = R_m C_m = 10$ ms, $\lambda = \sqrt{\frac{R_m d_a}{4 R_a}} = 0.041$ cm and $\rho = \frac{\pi d_a^{3/2}}{2 A_{sd}} = 0.064$.

The purpose of the mathematical model was to compute the frequency-dependent attenuation of voltage signals between the axon and the somato-dendritic compartment. One approach is to use a complex-valued input current in the original partial differential equation and solve for the voltage responses of the axon and the somato-dendritic compartment. Here, we will instead proceed using a real-valued input current and use the Fourier transforms of the above partial differential equation and boundary conditions:

$$\lambda^2 \frac{\delta^2}{\delta x^2} \hat{V}(x,\omega) - b(\omega)^2 \hat{V}(x,\omega) = \hat{g}(x,\omega) \quad \text{for} \quad x > 0 \tag{3.4}$$

with the boundary conditions

$$\frac{\delta}{\delta x} \hat{V}(0,\omega) - \frac{b(\omega)^2}{\lambda \rho} \hat{V}(0,\omega) = 0 \tag{3.5}$$

and

$$\lim_{x \to \infty} \hat{V}(x,\omega) = 0, \tag{3.6}$$

where $\hat{V}(x,\omega)$ and $\hat{g}(x,\omega)$ are the Fourier transforms of $V(x,t)$ and $g(x,t)$, respectively, $\omega = 2\pi f$ with frequency f (in Hertz), and $b(\omega)^2 = 1 + i\omega\tau$. We next calculated the voltage response of the model to the real-valued sinusoidal input current at location $x = y$:

$$g(x,t) = \frac{R_m}{\pi d_a} I_0 \cos(\omega_0 t) \delta(x - y) \tag{3.7}$$

with radial frequency $\omega = \omega_0 \geq 0$ and amplitude I_0. The Fourier transform of the input term

is

$$\hat{g}(x,\omega) = \frac{R_m}{\pi d_a} I_0\, \delta(\omega-\omega_0)\, \delta(x-y), \tag{3.8}$$

where we neglected the negative-frequency terms. We then solved the above second-order, nonhomogeneous ODE by first considering solutions of the form $\hat{V}_h(x,\omega) = c_1 \exp(b(\omega)\, x/\lambda) + c_2 \exp(b(\omega)\, x/\lambda)$ for the homogeneous version of the ODE and use this to find a particular solution $\hat{V}_{nh}(x,\omega)$ for the nonhomogeneous ODE; subsequently the constants c_1 and c_2 were determined by considering the boundary conditions (Tuckwell, 1988, section 6.2). The sinusoidal voltage response at location $0 \le x \le y$ is

$$\hat{V}(x,\omega_0) = \frac{I_0 R_\infty}{b_0} \left(\frac{\rho \cosh(b_0\, x/\lambda) + b_0 \sinh(b_0\, x/\lambda)}{(b_0+\rho)\exp(b_0\, y/\lambda)} \right), \tag{3.9}$$

and for $x \ge y$ it is

$$\hat{V}(x,\omega_0) = \frac{I_0 R_\infty}{b_0} \left(\frac{\rho \cosh(b_0\, x/\lambda) + b_0 \sinh(b_0\, x/\lambda)}{(b_0+\rho)\exp(b_0\, y/\lambda)} - \sinh(b_0\,(x-y)/\lambda) \right) \tag{3.10}$$

where $b_0 = b(\omega_0)$ is the principal square root (i.e., with positive real part) of $\sqrt{1+i\omega_0\tau}$ and $R_\infty = \frac{2}{\pi}\, d_a^{-3/2} \sqrt{R_m R_a}$ is the input resistance of a semi-infinite cable. The steady-state voltage attenuation from axon to soma is then given by the ratio of the voltage response amplitude at the axonal injection site to the somatic voltage response amplitude:

$$A_{axon\to soma}(y,\omega_0) = \left| \frac{\hat{V}(y,\omega_0)}{\hat{V}(0,\omega_0)} \right| = \left| \cosh(b_0\, y/\lambda) + \frac{b_0}{\rho} \sinh(b_0\, y/\lambda) \right|, \tag{3.11}$$

where $|z|$ denotes the absolute value of the complex number z. Similarly, the frequency-dependent voltage attenuation from soma to axon for a somatic input (i.e., $y = 0$ and $x \ge y$) can be computed, which is equal to the attenuation in an (semi-) infinite cable:

$$A_{soma\to axon}(x,\omega_0) = \left| \frac{\hat{V}(0,\omega_0)}{\hat{V}(x,\omega_0)} \right| = \left| \exp b_0\, x/\lambda \right|. \tag{3.12}$$

In Fig. 3.3B–G, the natural logarithm of the attenuation was plotted. The axonal stimulation/recording site was $y = 50$ μm away from the soma (except in Fig. 3.3B where it was varied). The passive-membrane model was also simulated numerically with the NEURON module embedded in Python (Hines et al., 2009) to compare the antidromic (axon-to-soma) attenuation of pure sine waves with the attenuation of an AP waveform. Here, identical parameters were used as in the analytical calculations (see above). The axon length was set to 2 mm, corresponding to an electrotonic length of 4.9 λ. The AP waveform was delivered via a voltage clamp at a 1 μm long axonal compartment located 50 μm away from the soma. We used an AP waveform recorded at the AIS of the detailed model (Fig. 3.1D, middle). The input capacitance in Fig. 3.3G was calculated from a small, prolonged voltage-clamp step by dividing the integrated transient charge by the voltage-clamp step size (Taylor, 2012).

Active model with reduced morphology

Results presented in Fig. 3.4 used an active compartmental model of a simplified neuron morphology. The model consisted of a dendritic cable (length × diameter: 900 μm × 6 μm), an axonal cable (1,060 μm × 1 μm), and a cylindrical somatic compartment (40 μm × 20 μm). The axonal cable included a proximal AIS (30 μm), a distal AIS (30 μm), and the axon (1,000 μm).

The passive model properties were uniform along the model neuron: specific membrane capacitance 1 μF/cm^2, specific membrane resistance 10 kΩcm^2, and axial resistivity 150 Ωcm. The resting membrane potential equaled the leak reversal potential, which was set to -70 mV. The active model properties included transient sodium and delayed rectifier potassium conductances. Channel models were taken from Migliore et al. (1999; ModelDB accession number 2796), with parameter values corresponding to hippocampal pyramidal neurons. Active currents were present in all compartments (densities given in parentheses): Na-channel conductance in the soma and the dendrite (0.02 S/cm^2), in the proximal AIS and the axon (0.04 S/cm^2), and in the distal AIS (0.1 S/cm^2); K-channel conductance in the soma and the dendrite (0.05 S/cm^2), in the proximal and distal AIS (0.25 S/cm^2), and in the axon (0.125 S/cm^2). Additionally, the activation and inactivation curves of the Na-channels in the distal AIS and in the axon were shifted by 10 mV in hyperpolarizing direction compared to the activation and inactivation curves of Na-channels in the dendrite, the soma, and the proximal AIS.

To elicit spiking activity in the model, rectangular current stimuli of 50 ms duration were applied at the soma. The resulting somatic event amplitude was measured from the voltage at the maximum of its second derivative (i.e., maximum curvature) to the peak voltage. However, if there was no AP occurring at the AIS (detected as not crossing a voltage threshold of -20 mV), the somatic amplitude was not plotted (white regions in the heat maps). The input capacitance (Fig. 3.4E) was calculated in the same way as in the passive-membrane model (see above).

Voltage traces shown in Fig. 3.5 were generated in a model with default parameters, except the length of the proximal AIS, which was set to 100 μm instead of the default 30 μm, so that all event types (spikelet, sh-AP, fb-AP) could be produced. In Fig. 3.5 C, the dynamics of sodium channel inactivation was "frozen" to the steady-state value at -70 mV by setting the time constant of inactivation to a very large value (10^5 ms).

Numerical simulations were performed using the NEURON simulation environment (Carnevale and Hines, 2006), with the NEURON module embedded in Python (Hines et al., 2009).

3.3 Results

3.3.1 In vivo-like input generates spikelets in a detailed model of a cortical pyramidal neuron

To investigate mechanisms underlying spikelet occurrence, we first used a previously published multi-compartmental model of a reconstructed layer V pyramidal neuron (Hu et al., 2009; Fig. 3.1 A). This model includes a detailed sodium channel distribution at the AIS and a hyperpolarized voltage shift of 13 mV in the activation and inactivation functions of the low-threshold $Na_V1.6$ channels, present in the AIS and axon To increase the incidence of spikelets, we modestly reduced the density of sodium channels (see Methods for details). The model cell was stimulated at the soma with stochastic excitatory and inhibitory synaptic point conductances (Destexhe et al., 2001) representing *in vivo*-like background activity. The resulting somatic voltage traces (Fig. 3.1 B, top) showed both APs and spikelets (stars). All APs were shoulder-APs (sh-APs; Epsztein et al., 2010) characterized by two components in the rising phase. The first component (the shoulder) was slower and resembled the waveform of spikelets (Fig. 3.1 C); the second, faster component included the peak of the AP.

To reveal the origin of spikelets and sh-APs in our model, we compared voltage traces in the soma and the AIS (Fig. 3.1 B). The APs and spikelets recorded at the soma were initiated as full APs at the distal AIS (Fig. 3.1 D). Accordingly, both the shoulders of the sh-APs and the spikelets reflected axonal APs invading the soma (Coombs et al., 1957a; Yu et al., 2008). Next, we aligned APs to the times of crossing a voltage threshold in the soma, and spikelets to the times of crossing the same voltage threshold in the AIS (Fig. 3.1 E, see also Methods). This alignment revealed a variable delay between the shoulder and the peak of the AP (Fig. 3.1 E, left) and demonstrated the all-or-none nature of the spikelet waveform (Fig. 3.1 E, F), as observed experimentally (Fig. 3.1 G; Epsztein et al., 2010).

To understand why APs initiated at the AIS sometimes failed to elicit a somatic AP, we calculated both AP-triggered and spikelet-triggered averages of the synaptic input (Fig. 3.1 H). Excitation slowly increased ca. 5 ms before the onset of both APs and spikelets but dropped sharply prior to spikelet initiation; inhibition was stronger during spikelets compared to APs (Fig. 3.1 H2). Together, this input resulted in a weaker and briefer depolarizing synaptic drive for the initiation of spikelets compared to APs (Fig. 3.1 H3). We found that fast sodium channel inactivation, known to modulate spiking thresholds (Platkiewicz and Brette, 2011), was not a major factor influencing spikelet generation in our model (Fig. 3.2).

Spikelets can thus be generated in a computational model of a single pyramidal neuron experiencing *in vivo*-like synaptic input: APs initiated at the AIS may fail to activate the soma and appear there as spikelets.

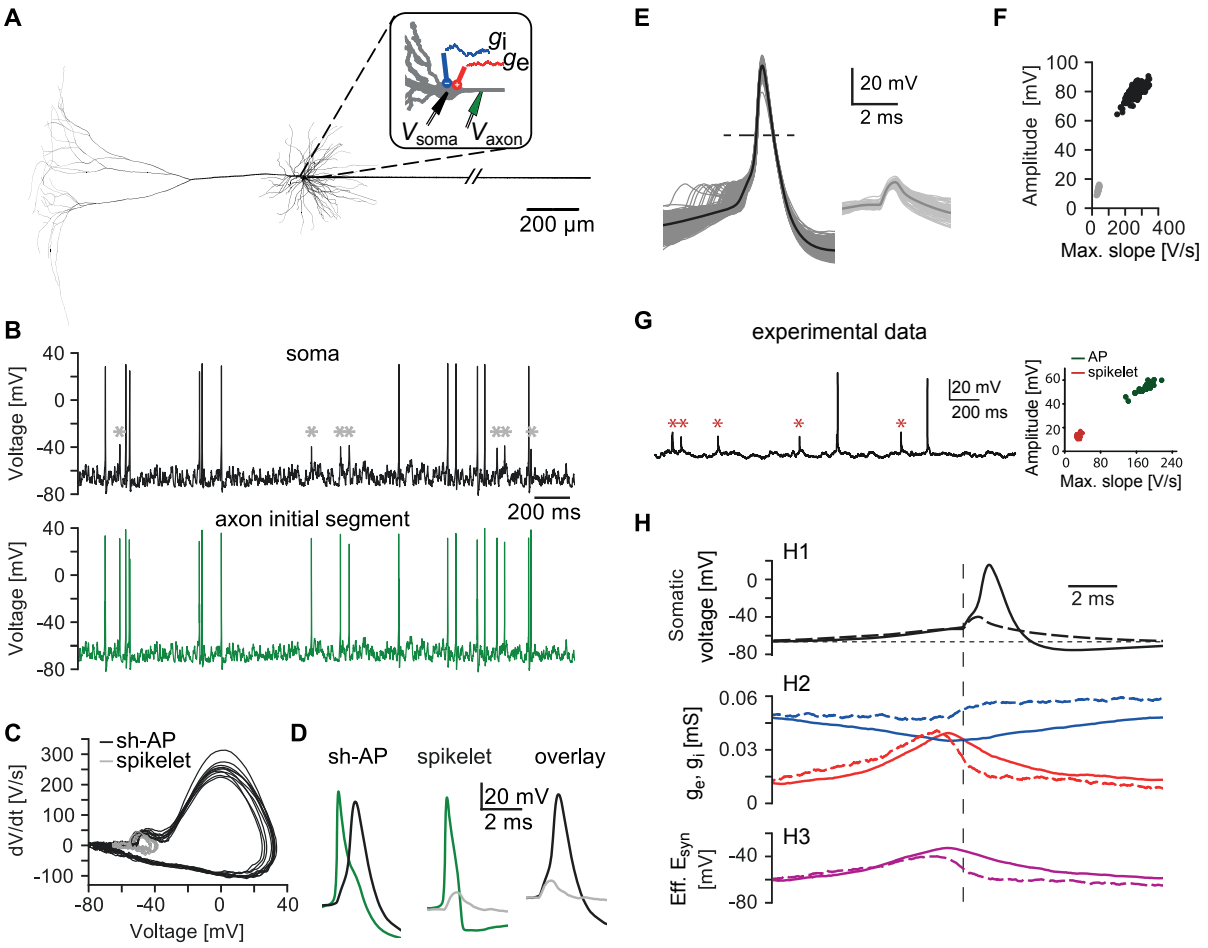

Figure 3.1: Somatic spikelets in a detailed biophysical model of a cortical pyramidal neuron in response to noisy input. (Continued on the following page.)

Figure 3.1: Somatic spikelets in a detailed biophysical model of a cortical pyramidal neuron in response to noisy input. **A**: Morphology of the model neuron. Inset: excitatory (g_e, red) and inhibitory (g_i, blue) conductances are placed at the soma. Recording electrodes are placed at the soma (V_{soma}, black) and the AIS (V_{axon},green). Basal dendrites were removed for clarity. **B**: Example three seconds of membrane voltage recorded at the soma (upper trace, black) and AIS (lower trace, green) during noisy stimulation. Somatic spikelets are marked with gray asterisks (*). Spikelets co-occur with APs at the AIS. **C**: Phase plot of ten somatic APs (black) and ten somatic spikelets (gray). **D**: Examples of a somatic AP (left, black) and a somatic spikelet (middle, gray) overlaid with the corresponding APs at the AIS (green traces). Right: overlay of the somatic AP (black) and the spikelet (gray). **E**: All somatic events generated during a 100 s simulation. Left: APs ($N = 579$, dark gray), aligned in time to crossing of the somatic voltage threshold (-10 mV, dashed line). The mean is shown in black. Right: spikelets ($N = 63$, light gray), aligned to the voltage threshold (-10 mV) crossing at the AIS. The mean is shown in dark gray. **F**: The all-or-none nature of APs (black) and spikelets (gray) is revealed in a plot of event amplitude against the maximum slope. **G**: Left: an example voltage trace recorded in a CA1 pyramidal neuron in a freely moving rat. Spikelets are marked with red asterisks (*). Right: Event amplitude plotted against the maximum slope of APs (dark green) and spikelets (red). From Epsztein et al. (2010). Reprinted with permission from AAAS, all rights reserved. **H**: AP- and spikelet-triggered averages (solid and dashed lines, respectively), aligned to the time of crossing the voltage threshold in the AIS (vertical dashed line) H1: mean somatic AP (solid line) and mean somatic spikelet (dashed line) waveform. The horizontal dashed line accentuates the depolarization prior to AP and spikelet occurrence. H2: mean excitatory (red) and mean inhibitory (blue) AP-triggered (solid line) and spikelet-triggered (dashed) conductances. H3: the mean effective synaptic reversal potential combines mean excitatory and inhibitory conductances (see also Methods). During APs (solid line), the synaptic drive was stronger than during spikelets (dashed line).

3.3.2 The soma-axon asymmetry shapes signal propagation in a passive-membrane model

Failure of AP propagation from the AIS to the soma (Fig. 3.1) suggests that there is a strong voltage attenuation from axon to soma such that the somatic voltage does not reach the spiking threshold. To identify cell properties that could underlie such attenuation, we mathematically analyzed a passive-membrane model consisting of an axonal cable connected to a single somato-dendritic compartment (Fig. 3.3 A; see Methods for details). In particular, we computed the attenuation for sinusoidal input currents at several frequencies as a function of all model parameters (Fig. 3.3 B–G; see Methods for equations).

A central factor influencing signal attenuation is the electrotonic distance between the soma and the AIS. Attenuation thus increases with increasing physical distance (Fig. 3.3 B), increasing axial resistivity (Fig. 3.3 C), and decreasing axonal diameter (Fig. 3.3 D). Importantly, the attenuation is typically much larger in the antidromic (axon-to-soma) than in the orthodromic (soma-to-axon) direction because the large somato-dendritic compartment provides a substantially stronger current sink for the passively propagated signal than the thin axon, i.e., there is a strong impedance mismatch between the two. Consistently, increasing the somato-dendritic surface area increased the attenuation of the antidromic signal whereas it did not affect the orthodromic propagation (Fig. 3.3 E). However, this did not reveal the nature of the current sink since the membrane resistance and the membrane capacitance are co-varied when changing the surface area. The specific membrane resistance, when varied separately in a range realistic for a pyramidal neuron ($> 1\ k\Omega\ cm^2$), did not influence the antidromic attenuation for frequencies > 100 Hz (Fig. 3.3 F); in contrast, the antidromic attenuation of high-frequency (> 100 Hz)

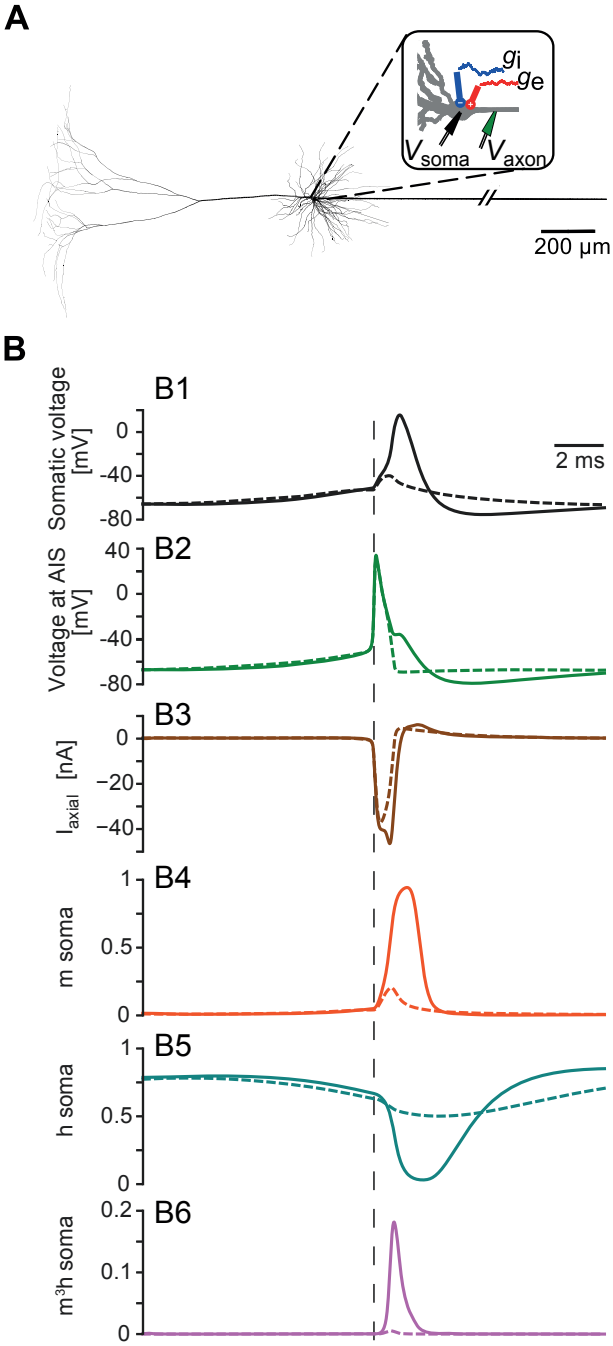

Figure 3.2: Fast sodium channel inactivation does not control spikelet generation in the detailed model from Fig. 3.1. Spiking thresholds are commonly modulated by (fast) sodium channel inactivation (Platkiewicz and Brette, 2011). In this context, spikelet generation could be theoretically supported by several mechanisms that restrict the soma from reaching the firing threshold, including: (1) larger somatic sodium channel inactivation, increasing the somatic firing threshold; (2) weaker $Na_V1.6$ channel inactivation at the AIS during spikelets, resulting in lower AP threshold at the AIS and, thus, larger threshold difference between the AIS and the soma; and (3) larger inactivation of proximal axonal $Na_V1.2$ channels, leading to smaller axial currents and, therefore, less somatic depolarization. (Continued on the following page.)

Figure 3.2: Fast sodium channel inactivation does not control spikelet generation in the detailed model from Fig. 3.1. This figure demonstrates that none of these mechanisms does account for spikelet generation in our model: AP thresholds at the soma (B1) and at the AIS (B2) are virtually identical for APs and spikelets, and so are the initial phases of the axial currents, corresponding to the currents from the AP initiated at the AIS (B3). Also the inactivation of somatic sodium channels is similar for spikelets and APs (B5). **A**: Morphology of the model neuron and location of the inputs and recording sites as in Fig. 3.1. **B**: AP- and spikelet-triggered averages (solid and dashed lines, respectively), aligned to the time of crossing the voltage threshold in the AIS (vertical dashed line), as in Fig. 3.1. B1: Mean somatic AP (solid line) and mean somatic spikelet (dashed line) waveform. B2: Mean AP waveforms at the AIS for somatic APs (solid line) and somatic spikelets (dashed line). B3: Mean axial currents entering the soma from the axon hillock during somatic APs (solid line) and spikelets (dashed line). Note that the first phase of the axial current, around the AP onset (vertical dashed line), is identical for APs and spikelets. B4: Mean activation variable of somatic sodium channels during APs (solid line) and spikelets (dashed line). B5: Mean somatic sodium channel inactivation during APs (solid line) and spikelets (dashed line). B6: The participation of somatic sodium channels is substantial during APs (solid line), but much smaller during spikelets (dashed line).

inputs was strongly influenced by the membrane capacitance (Fig. 3.3 G). For a fast, transient signal such as an AP, particularly the high-frequency components determine its shape. Indeed, in our model, the axon-to-soma attenuation of an AP waveform (black dashed lines in Fig. 3.3 B–G) was very similar to the attenuation of a 300 Hz sine wave.

Hence, apart from the electrotonic distance between soma and AIS, the capacitance of the somato-dendritic compartment strongly influences the attenuation of APs propagating from axon to soma. In general, the attenuation is asymmetric, i.e., much larger in the axon-to-soma than in the soma-to-axon direction, which constitutes a favorable condition for spikelet generation.

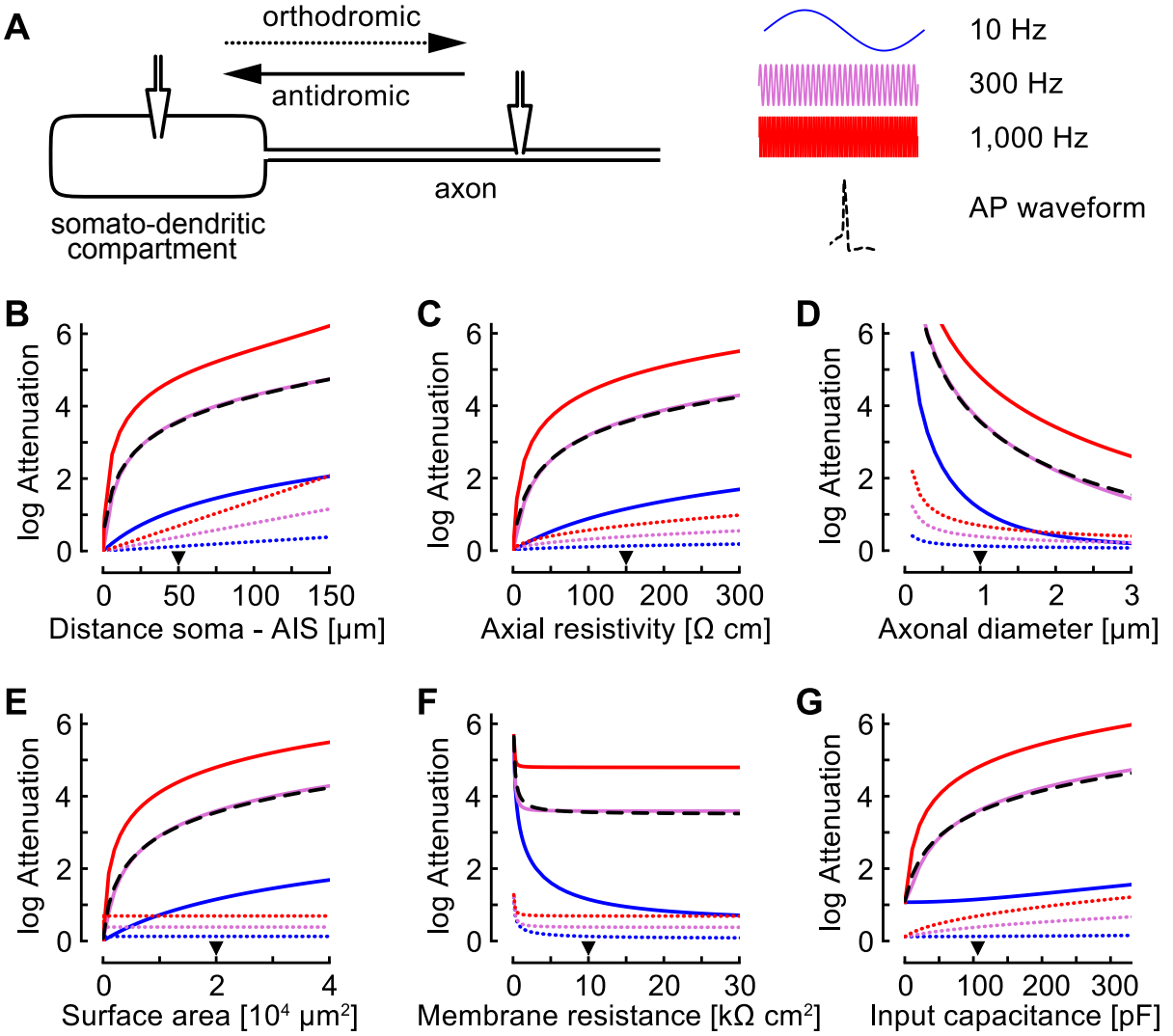

Figure 3.3: Signal attenuation in a passive-membrane model. **A**: The model consists of a somato-dendritic compartment attached to a semi-infinite cable (axon). Attenuation of sinusoidal inputs was calculated according to equations given in the Methods. Attenuation of an AP waveform was determined numerically. **B**–**G**: The natural logarithm of attenuation is plotted for the antidromic, axon-to-soma (solid lines) and for the orthodromic, soma-to-axon (dotted lines) signal propagation for three input frequencies: 10 Hz (blue), 300 Hz (purple), and 1,000 Hz (red). The results for the antidromic propagation of an AP waveform are shown as black dashed lines. The triangle indicates the default value of the parameter that is varied, all other parameters are held constant at their default values (see Methods for the default parameter values). The attenuation was determined in dependence upon the following model parameters: physical distance between the stimulation and the recording sites (**B**), axial resistivity of the axon (**C**), diameter of the axon (**D**), surface area of the somato-dendritic compartment (**E**), specific membrane resistance (**F**), and input capacitance of the somato-dendritic compartment (**G**), which was varied selectively by changing the specific membrane capacitance of the somato-dendritic compartment (range $0.01 - 3.1\ \mu\mathrm{F/cm^2}$).

3.3.3 Spikelets, shoulder-APs, and full-blown APs in an active model with reduced morphology

We next tested whether the asymmetric voltage attenuation is indeed a key component underlying the generation of spikelets through somato-dendritic input. For this, we turned to a model consisting of a dendrite, a soma, and an axon that all expressed active conductances (Fig. 3.4 A; see Methods for details). Similarly to the detailed compartmental model in Fig. 3.1, the sodium channels at the distal AIS and in the axon were set to activate and inactivate at more hyperpolarized voltages than the sodium channels in the dendrite, the soma, and the proximal AIS (Hu et al., 2009; Colbert and Pan, 2002). However, the model in Fig. 3.4 is much simpler than the complex model in Fig. 3.1, which enabled us to explore its parameter space.

To study the response of the model neuron with a simple stimulus, we applied rectangular current pulses (50 ms) to the soma for a range of input strengths. When an AP at the AIS was evoked, the corresponding somatic maximum response amplitude was recorded and plotted in a continuous color code (Fig. 3.4 B-H). However, the somatic response amplitudes typically appeared in three well-separated clusters (examples in Fig. 3.4 B and 3.5 B): (i) Spikelets (yellow) resulted from the weakest inputs that generated APs at the AIS but failed to evoke a somatic AP. (ii) The sh-APs (red) were evoked by larger somatic inputs and resulted from APs at the AIS that evoked a somatic AP. The shoulders of the sh-APs matched the spikelet waveform (see phase plots in Fig. 3.4 B, right). (iii) Finally, strong enough inputs could lead to full-blown APs (fb-APs; orange), which did not display a shoulder. The fb-APs resulted from AP initiation at the soma before or concurrent with AP initiation at the AIS. Consequently, fb-APs lacked the rapid onset ("kink") typical for spikelets and sh-APs (Fig. 3.4 B, right) and the fb-AP amplitudes (from maximum curvature to maximum voltage) appeared smaller than the amplitudes of sh-APs because the maximum curvature occurred at higher voltages (Fig. 3.4 B, right). So similarly to the detailed model from Fig. 3.1, input amplitude determined whether a spikelet or an AP was generated at the soma (see also Fig. 3.5)

To quantify how the somatic response type (spikelet, sh-AP, or fb-AP) depends on the somatic stimulus amplitude and the model parameters, we performed extensive numerical simulations of the active model with reduced morphology (Fig. 3.4 C–H). These simulations indicated that the occurrence of spikelets required a certain degree of electrotonic separation between the soma and the AIS (Fig. 3.4 C, D) to allow for sufficient attenuation from axon to soma, as was suggested by the analytical results from the passive-membrane model (see Fig. 3.3 B-D). Furthermore, spikelet generation needed a high enough somatic input capacitance (Fig. 3.4 E), in agreement with the analytical result that membrane capacitance was the primary current sink for APs propagating from AIS to soma (Fig. 3.3 F, G). Also as predicted, spikelet activity depended only weakly on the membrane resistance in a range that is plausible for pyramidal neurons (Fig. 3.4 F).

Besides the passive membrane characteristics, also active properties of sodium channels were fundamental to the generation of somatic spikelets (Fig. 3.4 G, H). Lowering somato-dendritic sodium channel densities increased the somatic firing threshold and thereby promoted spikelet occurrence (Fig. 3.4 G). This result is in agreement with the reduced sodium channel densities boosting spikelet generation in the multi-compartment model in Fig. 3.1. Another way to increase the firing-threshold difference between the soma and the AIS and thereby facilitate spikelet occurrence was to introduce a voltage shift in the activation function between the somato-dendritic and the axonal sodium channels (Fig. 3.4 H). The voltage shift had to be large enough such that an AP initiated at the AIS did not reach the voltage threshold in the soma.

In summary, the simulation results of the active model with reduced morphology confirm that spikelets can be evoked through sufficiently small somatic input. In addition to strong and asymmetric voltage attenuation, the generation of spikelets requires a substantially lower AP threshold in the AIS compared to the soma.

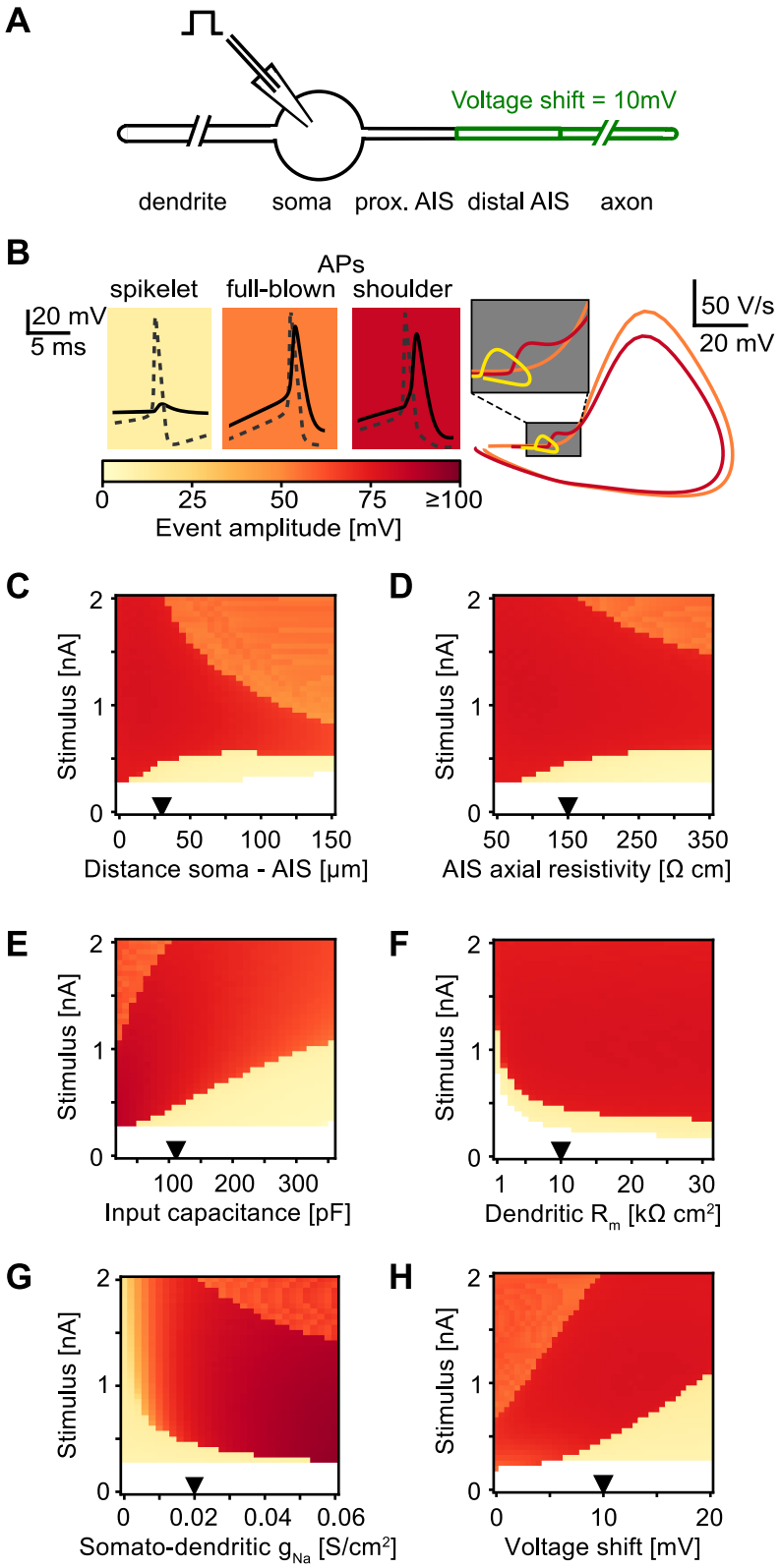

Figure 3.4: Conditions of spikelet generation in an active model with reduced morphology. (Continued on the following page.)

Figure 3.4: Conditions of spikelet generation in an active model with reduced morphology. **A**: Schematic of the neuron model. **B**: Left: exemplary APs and spikelets (solid line: soma, dashed line: AIS). The color bar indicates voltage amplitudes of somatic events. Right: phase plots of the exemplary somatic events shown on the left. Inset: a rapid onset ("kink") is present for spikelets (yellow) and sh-APs (red), but not for fb-APs (orange), which arise smoothly from the baseline. Note that fb-APs reached similar maximum voltages as the sh-APs, but fb-AP amplitudes were smaller because the maximum curvature, used to define the AP onset, occurred at more depolarized voltages (see Methods for details). **C**–**H**: Amplitude of somatic events (APs or spikelets) plotted in color code as a function of the stimulus strength (ordinate) and one of the model parameters (abscissa). Default values are indicated with triangles and given in the Methods. **C**: Physical distance between the soma and the distal AIS. **D**: Axial resistivity in the proximal and distal AIS. **E**: Input capacitance at the soma, varied through the specific membrane capacitance (range $0.2 - 3.2\ \mu\mathrm{F/cm^2}$). **F**: Specific membrane resistance, varied only in the dendrite. **G**: Sodium channel density at the soma and the dendrite. Axonal channel densities were kept constant. **H**: Voltage shift in the activation and inactivation curves between the somato-dendritic and the axonal sodium channels.

3.3.4 Orthodromic versus antidromic spikelets

Spikelets of axonal origin can be evoked with distal axonal stimulation when the antidromically propagating AP does not suffice to cross the somatic spiking threshold. Such antidromic spikelets could also result from axo-axonic coupling by gap junctions (Schmitz et al., 2001). Since the antidromic spikelets have different functional consequences than the orthodromic spikelets shown in Figs 3.1 and 3.4 , it is important to be able to distinguish the two phenomena.

To compare the properties of orthodromic and antidromic spikelets, the detailed model neuron with fluctuating somatic inputs from Fig. 3.1 was additionally stimulated with brief current pulses to the distal axon (Fig. 3.6 A), which evoked axonal APs propagating antidromically towards the soma. The resulting spikelets were classified as antidromic (evoked with the distal axonal stimulus) and orthodromic (evoked with the somatic stimulus). Classification was based on the relative timing of the AP occurring at the distal AIS and in the axon (Fig. 3.6 B; see Methods). The two spikelet types were similar in shape and amplitude (Fig. 3.6 B, C), but the averaged antidromic spikelet displayed a more hyperpolarized somatic threshold and started abruptly from the baseline without a preceding depolarization (Fig. 3.6 C1), which is also typical for experimentally recorded antidromic APs (Kandel et al., 1961). For the antidromic spikelets in our computational model, the somatic excitatory and inhibitory conductances as well as the effective synaptic reversal potential did not show any modulation, which is in line with its distal axonal origin and its independence from somatic activity (Fig. 3.6 C2 and C3).

3.3.5 Spikelets evoked by dendritic inputs

Although the physiological occurrence of antidromic spikelets is disputed (English et al., 2014), we hypothesized that spikelets with similar properties can occur in pyramidal cells when the axon is attached to a dendrite instead of the soma (Thome et al., 2014). To simulate this scenario, we adapted the morphology of the detailed model cell used in Figs 3.1 and 3.6 (Fig. 3.7; see Methods), and excitatory postsynaptic conductances (EPSGs) were delivered to the axon-carrying dendrite, additionally to the somatic fluctuating inputs (Fig. 3.7 A). The resulting spikelets (Fig. 3.7 B) were classified according to the relative timing of the spikelet and the EPSG (see Methods). Both types of spikelets had comparable shapes and phase plots (Fig. 3.7 B). Spikelets evoked with stimuli to the axon-carrying dendrite exhibited a hyperpolarized

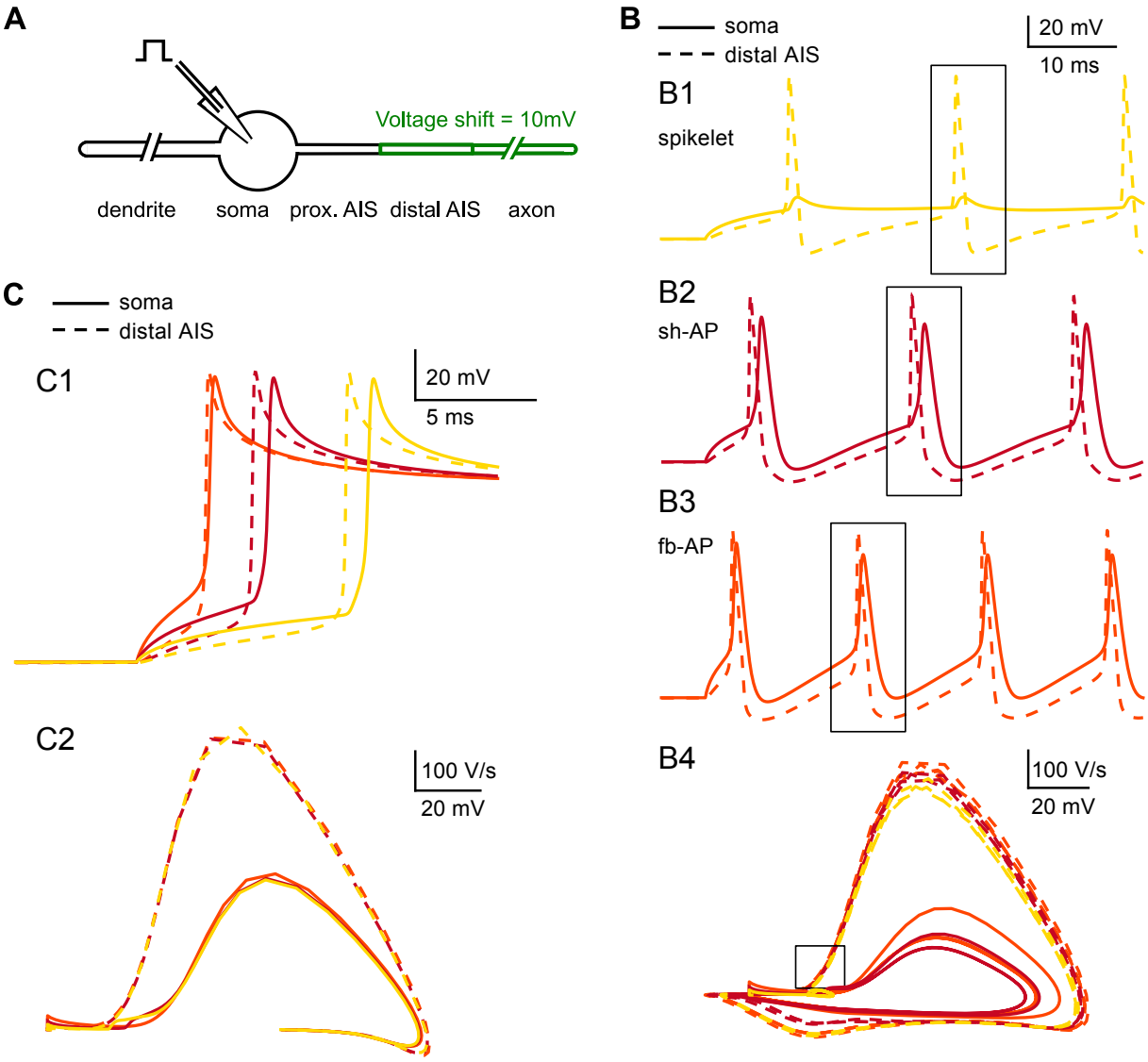

Figure 3.5: Fast sodium channel inactivation does not determine the somatic threshold of APs and spikelets in the simple model from Fig. 3.4. Unlike in the detailed model shown in Fig. 3.1, the threshold of spikelets appears smaller than the threshold of the sh-APs in the model with reduced morphology (Fig. 3.4 B). This might suggest that an additional mechanism, besides the input amplitude, might control the generation of spikelets versus APs for a given parameter set. However, the phase plots in B4 demonstrate that the threshold at the AIS was virtually identical for all three event types (compare curves within square box), but the maximum slope and peak voltage are larger for fb-APs than sh-APs, suggesting that more sodium current is generated during fb-APs than during sh-APs. Simulations with frozen dynamics of sodium channel inactivation, shown in C, indeed abolished the differences in the somatic waveforms (i.e., maximum amplitudes and slopes), but the somatic threshold differences remained. This result implies that sodium channel inactivation is not responsible for the observed voltage threshold difference between the three event types. Instead, the lower threshold of spikelets in these simulations is caused by the ongoing somatic input. (Continued on the following page.)

Figure 3.5: Fast sodium channel inactivation does not determine the somatic threshold of APs and spikelets in the simple model from Fig. 3.4. During the time between the AP initiation at the AIS and AP or spikelet occurrence at the soma, the soma is further depolarized by the ongoing current injection. Because the input is larger for APs than for spikelets, the soma depolarizes more for APs than for spikelets until the axial currents from AIS arrive, so that the somatic threshold appears higher for APs than spikelets. A: Sketch of the model neuron, as in Fig. 3.4. B: Full voltage traces used to extract the example events (boxes) in Fig. 3.4 B. Shown are traces generated with a 50-ms long somatic stimulus, recorded at the soma (solid lines) and at the distal AIS (dashed lines). The events were generated in a model with the default parameters, only the length of the proximal AIS was increased from 30 μm to 100 μm so that all three event types could be generated in the same model just by varying the input strength: 0.5 nA (B1, spikelet, yellow), 0.8 nA (B2, sh-AP, dark red) and 1.3 nA (B3, fb-AP, orange). B4: Phase plots for the somatic traces (solid lines) and traces at the distal AIS (dashed lines) shown in B1-B3. The threshold at the AIS is similar for all events (curves in square box). C: The same model and inputs as in B, but the dynamics of the sodium channel inactivation variable h was frozen to the steady-state value at -70 mV (see Methods). Shown are voltage traces (C1) recorded at the soma (solid lines) and at the AIS (dashed lines) and the corresponding phase plots (C2). Note that somatic spikelets do not occur here because the AP at the AIS does not repolarize, so the soma remains depolarized beyond the threshold.

average onset; nevertheless, some depolarization preceding these spikelets was visible in the somatic traces because the underlying input was located close enough to the soma ($\approx$ 25 μm). However, spikelets evoked with stimuli to the axon-carrying dendrite were basically independent of somatic conductances (Fig. 3.7 C), and these spikelets are therefore reminiscent of the antidromic spikelets described in Fig.ure 3.6.

Alternatively, when the model presented in Fig. 3.1 was additionally stimulated with brief current pulses at the proximal apical dendrite, the thresholds and waveforms of spikelets resulting from the dendritic stimulus were virtually identical to spikelets triggered by the fluctuating background stimulus applied to the soma (Fig. 3.8). The average background conductances (Fig. 3.8 C2) and the effective synaptic drive (Fig. 3.8 C3) were less modulated for the dendritically evoked spikelets than for the spikelets evoked with the background stimulus. The number of dendritically evoked spikelets was substantially smaller than for inputs located at the distal axon or at the axon-attached dendrite because of an interplay between the dendritic and somatic stimulus in spikelet generation: The dendritic stimulus added to the background somatic input and triggered spikelets if the soma had the right level of depolarization. If the soma was too depolarized at the time point when the dendritic stimulus arrives, somatic APs were evoked; if the soma was too hyperpolarized, the compound input did not suffice to trigger an AP at the AIS.

To summarize our results, spikelets can be generated within a single pyramidal neuron in three ways (Fig. 3.9 A, Sp1–Sp3). Each type of spikelet has characteristic features, which may allow to infer the origin of spikelets in experimental somatic voltage traces. Two key distinguishing features of spikelets are the somatic voltage threshold (Fig. 3.9 B) and the slope of the voltage a few milliseconds before the threshold is reached (Fig. 3.9 C). As a reference we consider the orthodromic APs, which exhibit the highest somatic firing threshold and are preceded by the steepest depolarization compared to the three types of spikelets: Orthodromic spikelets (Sp1) show a slightly smaller threshold and are preceded by a less steep depolarization, consistent with the finding that they required weaker inputs than APs. Antidromic spikelets (Sp2), which were evoked in our simulations with distal axonal stimulation, are characterized by the lowest thresholds and the highest somatic threshold variability. They arise

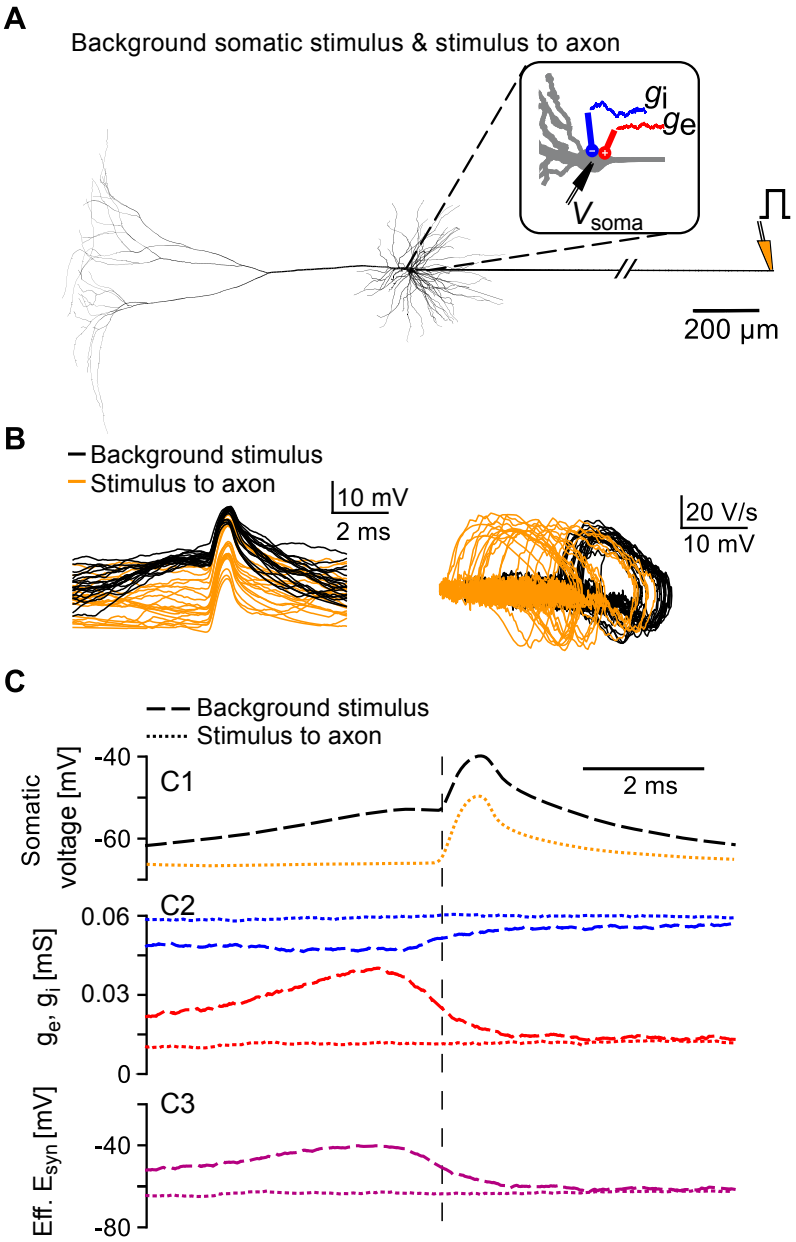

Figure 3.6: Orthodromic and antidromic spikelets in the biophysically complex model. **A**: Neuron model with fluctuating somatic inputs as in Fig. 3.1 (red: excitatory, blue: inhibitory). Additionally, the model cell was stimulated every 500 ms with a short current pulse at the distal axon (orange, see Methods). **B**: Left: example somatic spikelets; shown are 20 orthodromic (black, evoked with somatic inputs) and 20 antidromic spikelets (orange, evoked with distal axonal inputs). Right: phase plots of the spikelets depicted in the left panel. **C**: Spikelet-triggered averages for all orthodromic spikelets ($N = 66$, dashed lines) and all antidromic spikelets ($N = 194$, dotted lines) generated within 100 s of simulation. C1: Mean orthodromic (dashed black) and antidromic (dotted orange) spikelet, aligned to the voltage-threshold crossing at the AIS (as in Fig. 3.1 H). C2: Mean excitatory (red) and inhibitory (blue) conductances for orthodromic (dashed lines) and antidromic (dotted lines) spikelets. C3: Mean effective reversal potentials (as in Fig. 3.1 H) for the orthodromic (dashed line) and antidromic (dotted line) spikelets.

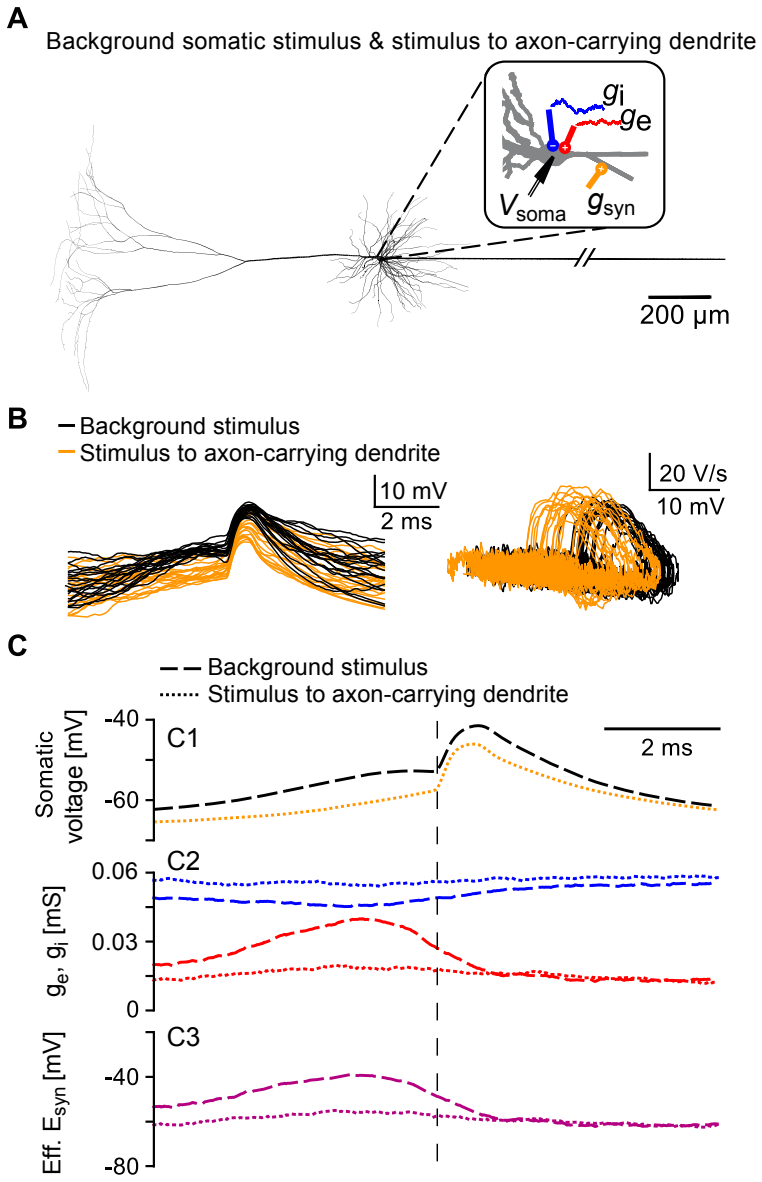

Figure 3.7: Orthodromic and antidromic-like spikelets in a model cell with the axon attached to a basal dendrite.
A: Neuron model with fluctuating somatic inputs as in Fig. 3.1 (red: excitatory, blue: inhibitory), except that the axon is attached to a basal dendrite. Additionally, the model cell was stimulated every 500 ms with a synaptic conductance g_{syn} located at the axon-carrying basal dendrite, distally to the AIS-connecting site (orange, see Methods). **B**: Left: example somatic spikelets; shown are 20 orthodromic (black, evoked with somatic inputs) and 20 antidromic-like (orange, evoked with dendritic input). Right: phase plots of the spikelets shown in the left panel. **C**: Spikelet-triggered averages for all orthodromic spikelets ($N = 137$, dashed lines) and all antidromic-like spikelets ($N = 100$, dotted lines) generated within 100 s of simulation. C1: Mean orthodromic (dashed black) and antidromic-like (dotted orange) spikelet, aligned to the voltage-threshold crossing at the AIS (as in Fig. 3.1 H). C2: Mean excitatory (red) and inhibitory (blue) conductances for orthodromic (dashed lines) and antidromic-like (dotted lines) spikelets. C3: Mean effective reversal potentials (as in Fig. 1H) for the orthodromic (dashed line) and antidromic-like (dotted line) spikelets.

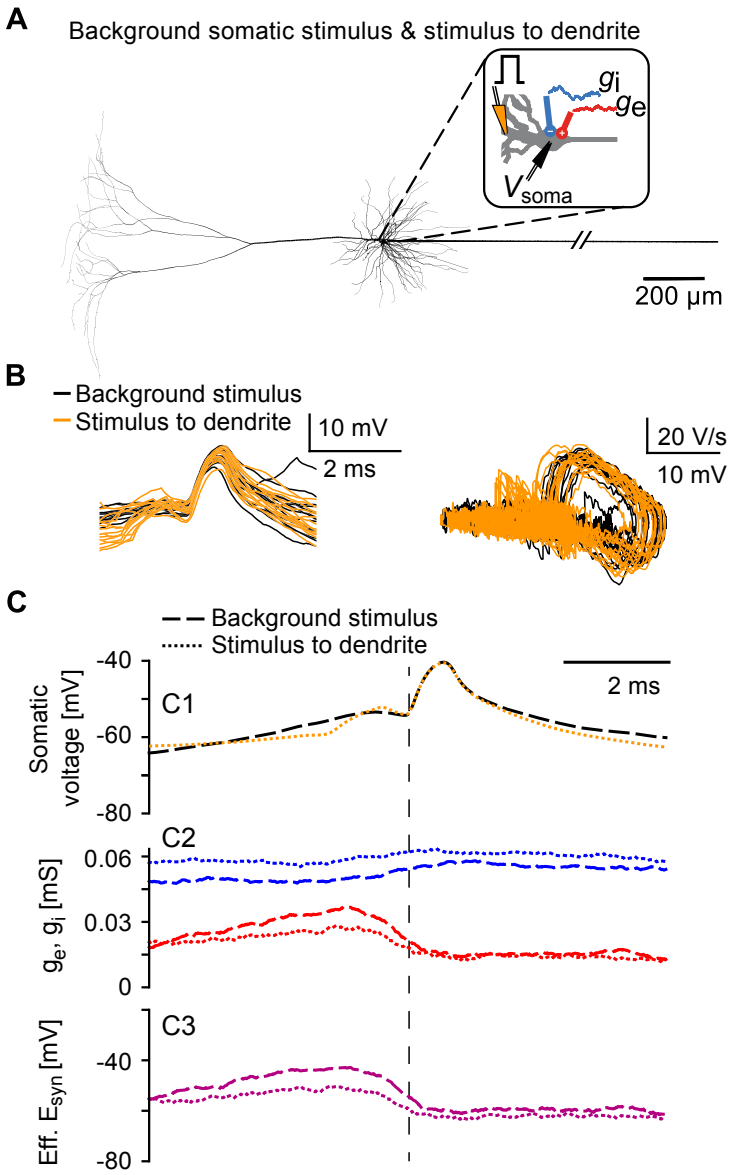

Figure 3.8: Orthodromic spikelets evoked with somatic background inputs and dendritic current stimuli. **A**: Neuron model with fluctuating somatic inputs as in to Fig. 3.1 (red: excitatory, blue: inhibitory). Additionally, the model cell was stimulated every 20 ms with a brief current pulse at the proximal apical dendrite (orange, see Methods). **B**: Left: example somatic spikelets; shown are 15 spikelets evoked with the dendritic stimulus (orange) and 15 spikelets evoked with the somatic background stimulus (black). Right: phase plots of the depicted spikelets. **C**: Spikelet-triggered averages for all spikelets evoked with the somatic background stimulus ($N = 41$, dashed lines) and all spikelets triggered by the dendritic input ($N = 43$, dotted lines) generated within 200 s of simulation, see Methods. C1: Mean spikelets evoked with the somatic background stimulus (black dashed line) and with the dendritic stimulus (orange dotted line), aligned to the voltage-threshold crossing at the AIS (as in Fig. 3.1 H). C2: Mean excitatory (red) and inhibitory (blue) conductances for spikelets evoked with the somatic background stimulus (dashed lines) and for spikelets evoked with the dendritic stimulus (dotted lines). C3: Mean effective reversal potentials (as in Fig. 1H) for spikelets evoked with the somatic background stimulus (dashed line) and with the dendritic stimulus (dotted line).

abruptly at the soma: the averaged voltage trace shows no preceding depolarization. Finally, spikelets evoked by inputs to the axon-carrying dendrite (Sp3) lie somewhere in between the orthodromic and antidromic spikelets, regarding the average somatic threshold and the preceding depolarization; their orthodromic-like versus antidromic-like appearance depends on the electrotonic separation of the soma and the axon-carrying dendrite.

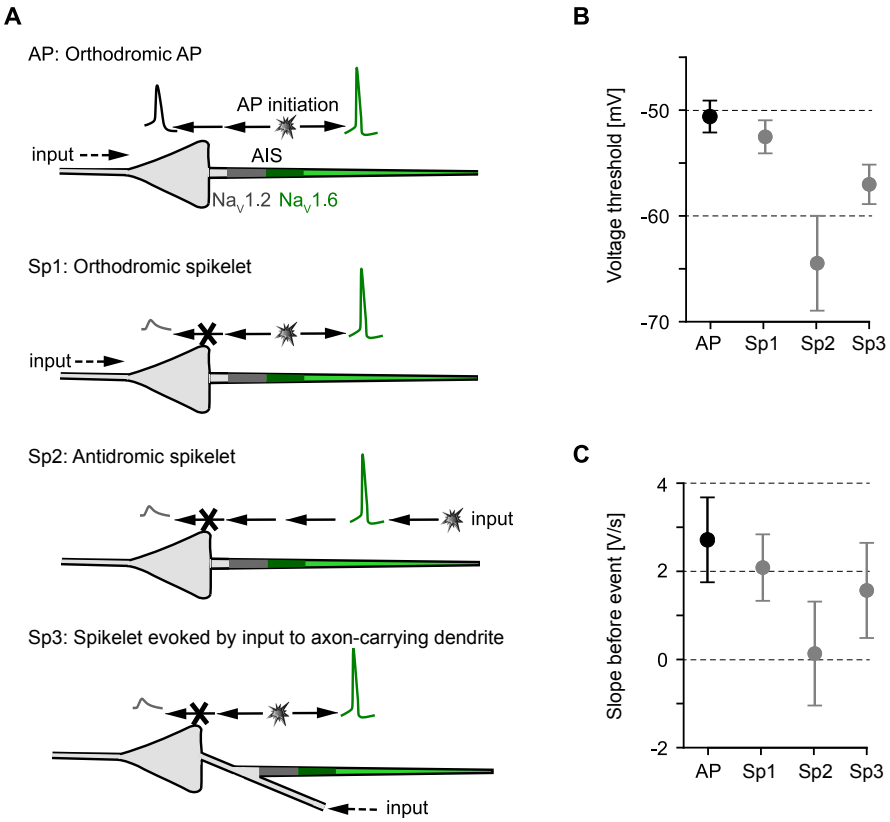

Figure 3.9: Mechanisms of spikelet generation in pyramidal neurons. **A**: Sketch of the pyramidal-cell neuron model. The axon initial segment (AIS) can be divided in the proximal part (dark gray), where high-threshold $Na_V1.2$ channels accumulate, and the distal part, where low-threshold $Na_V1.6$ channels accumulate (dark green). High-threshold $Na_V1.2$ channels are present at lower densities throughout the soma and dendrites (light gray). Low-threshold $Na_V1.6$ channels are located throughout the axon (light green), but at lower densities than in the distal AIS (see Methods). We distinguish four different scenarios (AP, Sp1, Sp2, Sp3), which are described in detail in what follows. AP: Strong enough somato-dendritic inputs initiate an AP at the distal AIS (dark green). The AP then propagates down the axon and back to the soma and into the dendrites. Sp1: Weaker and briefer somato-dendritic inputs give rise to somatic spikelets if the AP initiated at the AIS fails to trigger a somatic AP. However, the axonal AP propagation to the postsynaptic targets remains unaffected. Sp2: Antidromic spikelets occur when an AP initiated in the distal axon propagates to the soma, but does not suffice to evoke a somatic AP. Sp3: In neurons with the axon connected to a basal dendrite, spikelets can also be evoked by inputs to the axon-carrying dendrite. These inputs can evoke an AP at the AIS without passing the soma first. The evoked AP, in turn, propagates down the axon but might fail to trigger a somato-dendritic spike, so a somatic spikelet appears. **B**: Mean somatic voltage threshold for the four scenarios illustrated in A: orthodromic APs (AP, $N = 579$), orthodromic spikelets (Sp1, $N = 63$), antidromic spikelets (Sp2, $N = 194$), and spikelets evoked by inputs to the axon-carrying dendrite (Sp3, $N = 100$). Error bars mark standard deviation. **C**: Mean somatic voltage slope in the 5-ms interval before the event, for the four scenarios illustrated in A.

3.4 Discussion

Action potentials are the basis of neural function, yet some of their fundamental features are still not well understood, as highlighted by the recent focus on the rapidness of the AP onset (Yu et al., 2008; Naundorf et al., 2006; Brette, 2013). It is generally assumed that an AP initiated in the AIS of a pyramidal neuron always leads to an AP in the soma. We argue here that this view needs to be corrected. Under certain conditions, APs initiated in the AIS by somato-dendritic inputs fail to fully activate the soma and appear there as spikelets.

In simulations we showed that spikelets can result from APs that were evoked at the AIS with somato-dendritic inputs and propagated down the axon, but that did not trigger a somato-dendritic AP. This AP failure occurred for a sufficiently large difference in spiking thresholds between the soma and the AIS, together with a strong impedance mismatch (causing asymmetric voltage attenuation) and some degree of electrotonic separation between the soma and the AIS. In this way, a weak depolarizing input could pass through the soma and initiate an AP at the AIS, which, in turn, was not able to depolarize the soma to the firing threshold. Thus, a spikelet appeared at the soma instead of an AP.

This mechanism reproduced several key features of spikelets reported in the experimental literature (Chorev and Brecht, 2012; Epsztein et al., 2010; Crochet et al., 2004): the fast dynamics and rapid onset of spikelets as well as the match between the spikelet waveform and the shoulder of a sh-AP. This single-cell mechanism is also in line with the observation that APs and spikelets recorded in a single hippocampal place cell exhibit virtually identical place fields (Epsztein et al., 2010). In contrast, in the electrotonic-coupling (gap junction) scenario of pairs of pyramidal cells (Mercer et al., 2006; Hamzei-Sichani et al., 2007; Schmitz et al., 2001), the place fields of spikelets and APs measured in a single cell are expected to differ due to lack of topography in hippocampus (Redish et al., 2001). We found that the fast dynamics and amplitudes of spikelets observed in pyramidal neurons can be compatible with gap junction coupling only the somato-dendritic gap junctions are very strong and located at proximal sites (Fig. 3.4).

In previous experimental studies, spikelets could be evoked with dendritic stimulation or dendritic EPSPs (Spencer and Kandel, 1961; Crochet et al., 2004), which led the authors to conclude that somatic spikelets arise from dendritic spikes. However, our modelling results suggest that although spikelets can be evoked with somato-dendritic inputs, they rather originate in the axon. Depending on the state of the proximal axonal sodium channels, the AP is initiated either in the AIS, as we considered in this study, or further down the axon. Consistently, a recent experimental study demonstrated an axonal origin of spikelets occurring during dendritic plateau-driven complex spiking in CA1 pyramidal neurons (Apostolides et al., 2016). Also in other central neurons, spikelets occurring during somatic bursts can originate in the axon, for example, in inferior olivary neurons (Mathy et al., 2009) and in cerebellar Purkinje neurons (Khaliq and Raman, 2005).

Antidromic spikelets also result from axonal APs, but these are evoked by distal axonal inputs (Sheffield et al., 2010) or by APs propagating through putative axo-axonal gap junctions (Schmitz et al., 2001). Compared to the orthodromic spikelets, antidromic spikelets are characterized by hyperpolarized thresholds and they arise abruptly without a preceding depolarization (Fig. 3.6 C1). However, the best experimental distinguishing criterion is the fact that, because of their distal origin, they survive moderate levels of somatic hyperpolarization, as has been demonstrated, for example, in layer V pyramidal neurons *in vitro* (Hu et al., 2009). Orthodromic spikelets do not occur when the soma is hyperpolarized, since the synaptic depolarizing input has to pass through the soma to trigger an AP at the AIS. Spikelets evoked by inputs to the axon-carrying dendrite (Fig. 3.7) would also be abolished by a certain level of somatic hyperpolarization, because of the relatively small electrotonic distance between the soma and the axon origin (Thome et al., 2014). Consistent with an orthodromic origin of spikelets is

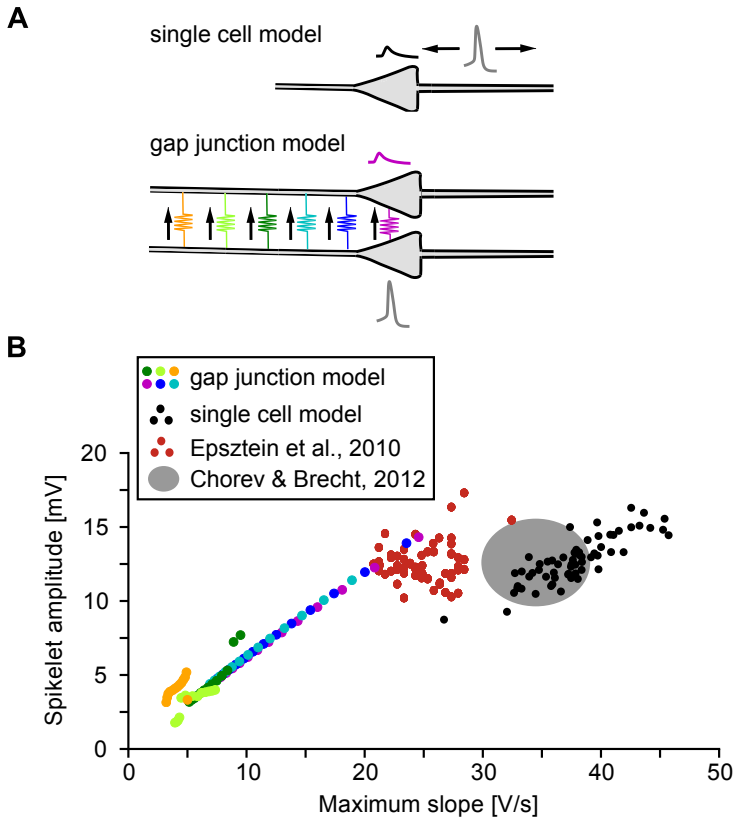

Figure 3.10: Comparison of spikelet properties generated in a single cell and in pairs of model cells coupled by gap junctions. We simulated spikelets resulting from somatic and dendritic coupling by gap junctions and compared them to the spikelets simulated in Fig. 3.1 as well as to the spikelets recorded experimentally (Epsztein et al., 2010, Fig. 3.1 G and Chorev and Brecht, 2012). The results demonstrate that properties of spikelets generated with somatic or very proximal dendritic gap junctions can fit spikelet properties observed experimentally. However, to reach such large amplitudes in the gap-junctional scenario, we had to hyperpolarize the somatic membrane voltage to -80 mV to prevent the postsynaptic cell from spiking. Moreover, the fast dynamics of experimentally recorded spikelets restricts the position of the putative somato-dendritic gap junctions to very proximal locations and predicts a very strong gap junctional conductance ($37 - 45$ nS), about 20 times stronger than the largest estimates for gap junctional conductances in cortical interneurons ($0.2 - 2.1$ nS, Galarreta and Hestrin, 2001) . Spikelets simulated in a single cell (Fig. 3.1) fit well to the properties of experimentally observed spikelets. A: Model schematics: single-cell spikelets from Fig. 3.1 are initiated as APs at the AIS that fail to activate the soma. In cells coupled by a gap junction (colored symbols), an AP evoked in the presynaptic cell appears as a spikelet in the postsynaptic cell. The gap junction was located at the soma or at various positions along the main apical dendrite, up to 109 μm away from soma (see Methods). B: Spikelet amplitude plotted against the maximum slope for spikelets generated in a single-cell model (black; Fig. 3.1 F), spikelets recorded in CA1 pyramidal cells *in vivo* (red; Fig. 3.1 G, Epsztein et al., 2010; gray Chorev and Brecht, 2012), and spikelets generated in the gap-junction coupling scenario for various strengths and positions of the gap junctions (see Methods; color code denotes the position of the gap junction, according to the schematic in A).

the observation that spikelets are suppressed by hyperpolarizing somatic current injections, leading to the conclusion that spikelets "are not generated far from the soma" (Crochet et al., 2004).

Our proposed spikelet hypothesis relies on AP initiation at the AIS. Indeed, APs in hippocampal (Meeks and Mennerick, 2007) and neocortical pyramidal neurons (Hu et al., 2009; Palmer and Stuart, 2006) are typically initiated in the distal portion of the AIS, about $20-40\ \mu$m away from the axon hillock. This site is preferred for AP initiation because of its decreased capacitive load from the soma (Baranauskas et al., 2013) and increased sodium channel density, especially of the $Na_V1.6$ channel subtype (Royeck et al., 2008), which activates at more hyperpolarized membrane potentials than the somatic sodium channel subtype $Na_V1.2$ (Colbert and Pan, 2002). However, it is still disputed whether the axonal sodium channel density is substantially higher (up to 50-times higher, (Kole et al., 2008)) than the somatic sodium channel density or whether the axonal and somatic sodium channels have similar densities (Fleidervish et al., 2010; Colbert and Pan, 2002).

The model neuron used in Figs 3.1, 3.6, 3.7, and 3.9 is characterized by a high ratio between the axonal and somatic sodium channel densities (up to a factor of 40; Hu et al., 2009), which contributes to the large threshold difference between the axon and the soma, thus favoring spikelet generation. The question then arises how spikelet generation is affected when the sodium channel density ratio is smaller. The model used in Fig. 3.4 employed a much smaller density ratio of 5 between the soma and the distal AIS (0.02 and 0.1 S/cm^2, respectively). Fig. 3.4G illustrates that spikelets occurred when the somatic sodium channel density was less than half the value at the distal AIS (i.e., $< 0.05\ S/cm^2$). *In vivo*, a fraction of somatic sodium channels is inactivated due to ongoing activity, which decreases the effective sodium channel density and promotes spikelet occurrence. However, the range of density ratios that support spikelet generation is not absolute, but depends on other parameters influencing somatic voltage threshold, like the voltage shift between the activation of somatic and axonal sodium channels (Fig. 3.4 H).

In the present study, we used the standard sodium channel models that were fitted to neocortical (Figs 3.1, 3.6, 3.7, and 3.9, Hu et al., 2009) and hippocampal (Fig. 3.4, Migliore et al., 1999) pyramidal neurons. However, the dynamics of these model channels is slow compared to what has been found in more recent experiments (Engel and Jonas, 2005; Baranauskas and Martina, 2006). Interestingly, simulations by Fleidervish et al. (2010) demonstrated that the faster, more realistic, sodium channel activation generated larger axo-somatic delays and larger voltage gradients than the classic, slower, sodium channel models. As this axo-somatic gradient is vital for spikelet generation, we expect faster Na-channel gating to support spikelet generation.

Experimental recordings featuring spikelets typically contain two types of APs: shoulder-APs with an initial slower phase corresponding to the spikelet, and full-blown APs, characterized by a single rising phase without a shoulder (Epsztein et al., 2010). The shoulder of sh-APs is considered to result from the AP evoked at the AIS (e.g., Yu et al., 2008). Then, the question about the origin of fb-APs arises. In our detailed compartmental model (Fig. 3.1), all APs are evoked at the AIS and exhibit a shoulder. In the simple model shown in Fig. 3.4, fb-APs can be generated with strong stimuli and for large electrotonic distances between the soma and the AIS, which allows somatic AP initiation to precede or co-occur with AP initiation at the AIS. However, unlike experimentally recorded fb-APs, they arise smoothly from the subthreshold depolarization and do not exhibit a rapid onset that is present also in simulated and experimentally recorded spikelets and sh-APs. According to the "compartmentalization hypothesis of AP initiation" (Brette, 2013), the AP onset rapidness is caused by axonal AP initiation. This suggests that experimentally recorded fb-APs with rapid onset are not generated at the soma. Consistently, somatic AP initiation due to serotonin inhibition of AIS channels can result in gradually rising APs without a rapid onset (Cotel et al., 2013). Therefore, we hypothesize that

fb-APs are either generated at the AIS and the shoulder is "masked" by fast somato-dendritic activation or they are initiated in the apical dendrites and no shoulder is visible because of the smooth morphologic transition between the primary apical dendrite and the soma.

An intriguing issue concerns the rare observation of spikelets *in vitro*. Our analyses suggest that pyramidal neurons are positioned at the edge of a regime that allows spikelet generation. In the complex model from Hu et al. (2009) used in Fig. 3.1, for example, a modest decrease in sodium channel density strongly increased spikelet occurrence. One reason for such a decrease in functional sodium channel availability might be slow sodium channel inactivation (Mickus et al., 1999). *In vitro*, there is less slow sodium channel inactivation: a larger fraction of sodium channels might be available for spiking due to a lower average membrane potential and a lower firing activity, which keeps the fraction of inactivated sodium channels low. Additionally, sodium channel availability is regulated by various neuromodulators, acting via activity-dependent phosphorylation (Carr et al., 2003). This might be especially relevant *in vivo*, where a variety of homeostatic mechanisms are expected to maintain spiking activity in neural circuits (Turrigiano, 2011). In our models, fast sodium channel inactivation was not a main factor influencing spikelet generation (Fig. 3.2 and 3.5). It cannot be ruled out, however, that fast sodium inactivation does play a significant role in real neurons under certain *in vivo* conditions.

Another important factor for spikelet generation is the somato-dendritic current sink, which is reduced in brain slices because of "dendritic pruning", i.e., dendritic processes cut by the slicing procedure (Mainen et al., 1996). The typical thickness of slices is a few hundred microns (e.g., 300 μm, Schmitz et al., 2001; Hu et al., 2009), which roughly matches the spatial extent of a pyramidal neuron's dendritic tree (e.g., Scorcioni et al., 2004). For patch-clamp recordings, cells close to the slice surface are preferentially used, which is where one expects significant damage to proximal dendrites (Mainen et al., 1996). A pyramidal cell's input capacitance is in the range of hundreds of picofarads (Narayanan and Johnston, 2008), and considerable changes of this value are predicted to strongly affect spikelet occurrence (Fig. 3.4 E). In contrast, an artificial capacitance increase of about $4 - 10$ pF by an uncompensated patch electrode (Thomas, 1977) is small compared to a pyramidal cell's input capacitance and, thus, should not influence spikelet incidence significantly.

The presented hypothesis predicts that all-or-none somatic spikelets in pyramidal neurons are associated with APs at the AIS or further down in the axon (Apostolides et al., 2016). This mechanism could be tested experimentally with simultaneous recordings of the somatic and axonal membrane voltages, which, however, might be difficult *in vivo*. An alternative would be to establish a reliable spikelet model *in vitro*. We propose to recreate *in vitro* a state of a pyramidal cell that retains the *in vivo* properties of sodium channels, for example by prolonged stimulation with fluctuating inputs and/or application of relevant neurotransmitters and neuromodulators naturally present in the cerebrospinal fluid *in vivo* (Bjorefeldt et al., 2015). Additionally, it might be necessary to record from neurons located in the middle of a slice, to minimize the dendritic loss and the resulting decrease in the somato-dendritic current sink.

Interestingly, unlike in mammalian cells, spikelets are easily evoked in turtle pyramidal neurons *in vitro* with weak somatic or dendritic stimuli (Connors and Kriegstein, 1986; Larkum et al., 2008). The amplitudes and waveforms of these spikelets closely resemble those in mammalian pyramidal neurons. Dual somatic and axonal recordings suggested an axonal origin of these spikelets (Larkum et al., 2008). We hypothesize that there might be two important differences between turtle and mammalian neurons that support *in vitro* spikelet firing in turtles. First, the slower and wider APs in turtles suggest that the effective (peri-)somatic sodium channel densities might be smaller in turtle than in mammalian pyramidal neurons. Second, the somata of turtle neurons are substantially larger than the somata of mammalian neurons, and most of the dendrites are single branches extending from the soma (Larkum et al., 2008).

This might result in an increased capacitive somato-dendritic current sink and augment the impedance mismatch between the axon and the soma.

The spikelets we described here are APs that propagate forward down the axon but not backward into the soma and the dendrites. What could be a functional role of such "output-only APs"? From an energetic point of view, spikelet firing saves energy since it avoids activation of sodium currents in the soma and the dendritic tree. Output-only APs thus minimize their contribution to activity-dependent metabolism (Alle et al., 2009; Ashida et al., 2007). Moreover, spikelets might be a means of reading out the result of neuronal computations without triggering dendritic plasticity through backpropagating APs (Spruston et al., 1995). Hence, spikelets potentially represent a mode of operation that is functionally highly relevant.

To further unravel the role spikelets may play in neural computations, more theoretical and experimental studies are needed. Developing a CA1 pyramidal neuron model with a realistic AIS composition incorporating state-of-the-art sodium channel models is vital for a quantitative study of spikelet generation and properties, as the prevailing experimental work on spikelets has been carried out in these neurons. In order to construct such a model, further experimental studies of AIS composition and function in CA1 pyramidal neurons are necessary. Future studies could also address the putative role of axo-axonic synapses in spikelet generation, which provide powerful inhibition at the proximal AIS that can prevent antidromically evoked APs from invading the soma (Dugladze et al., 2012). It would be important to see whether these synapses can control the propagation of orthodromically initiated APs and give rise to somatic spikelets, given the small distances between the soma and the distal AIS and the requirement for precise timing of inhibition: Too early inhibition would shunt the subthreshold depolarization and prevent AP initiation in the first place, whereas too late inhibition would be ineffective to stop the propagating AP (see also Wilmes et al., 2016). Also the influence of sodium channel neuromodulation on spikelet occurrence (Carr et al., 2003) and generation of full-blown APs in cells exhibiting spikelets are important topics for our understanding of spikelets in pyramidal neurons. This knowledge should allow to assess the computational consequences of spikelet firing at the single-cell and network level.

4 Extracellular correlates of spikelets: what do they reveal about spikelet origin?

The waveform of an extracellularly recorded action potential (eAP) provides valuable data about various aspects of AP generation and propagation within a neuron (Gold et al., 2006). Detailed computational modeling, however, is necessary to decode the information contained in the features of the eAP waveform. Chorev and Brecht (2012) performed dual intra- and extracellular recordings in hippocampal pyramidal neurons *in vivo* and identified extracellular correlates of AP and spikelet firing. They observed that the onset of the spikelet-associated extracellular waveform slightly preceded the onset of the AP-associated waveform and interpreted this finding as evidence for gap-junctional origin of spikelets. To gain further insights into the implications of this data for the mechanism of spikelet generation, I simulated extracellular waveforms associated with APs and spikelets in compartmental models of pyramidal neurons. I considered spikelets generated in neurons coupled by gap junctions as well as spikelets originating at the axon initial segment in a single cell. Overall, I found that the dual intra- and extracellular data by Chorev and Brecht (2012) provide strong constraints for the mechanism(s) of spikelet generation in pyramidal neurons. According to my results, the single-cell hypothesis of spikelet origin is consistent with the experimental data by Chorev and Brecht (2012). The electrotonic coupling can account for all considered data features only for an axonal location of the gap junction and a large distance between the somata of the coupled cells (> 140 μm), such that only the intracellularly recorded cell shapes the extracellular AP waveform. This scenario, however, is practically indistinguishable from a single-cell case with antidromic spikelets. My results demonstrate that the cell firing a spikelet does generate a detectable extracellular waveform that is different from the AP waveform generated by the same cell and recorded at the same location. This implies that spikelets and APs generated in one cell are incorrectly classified as two different units in extracellular recordings, albeit they together constitute the output of a single pyramidal neuron.

4.1 Introduction

Extracellular AP waveform

Recordings of extracellular potentials are a widespread method to study neural activity *in vivo* and *in vitro*. Extracellular correlates of action potential firing (eAPs) have been used for decades to identify spiking in the vicinity of an extracellular electrode. Here, the timing of the eAP is typically the main extracted information; the waveform of individual eAPs is only used for classification of cell types and for differentiation of spike trains of individual units (spike sorting; Fig. 4.1).

However, the eAP waveform potentially bears much more information about the cell and its state during spiking as it arises from the summed membrane currents along the neuron (Gold et al., 2006, 2007; Fig. 4.2 A). The individual components of the eAP waveform are determined by the combination of ionic action currents and the pattern of AP initiation. Recordings close to a large cellular compartment like soma or primary apical dendrite are predominantly shaped by localized currents from the nearby comparment. On the other hand, a recording electrode

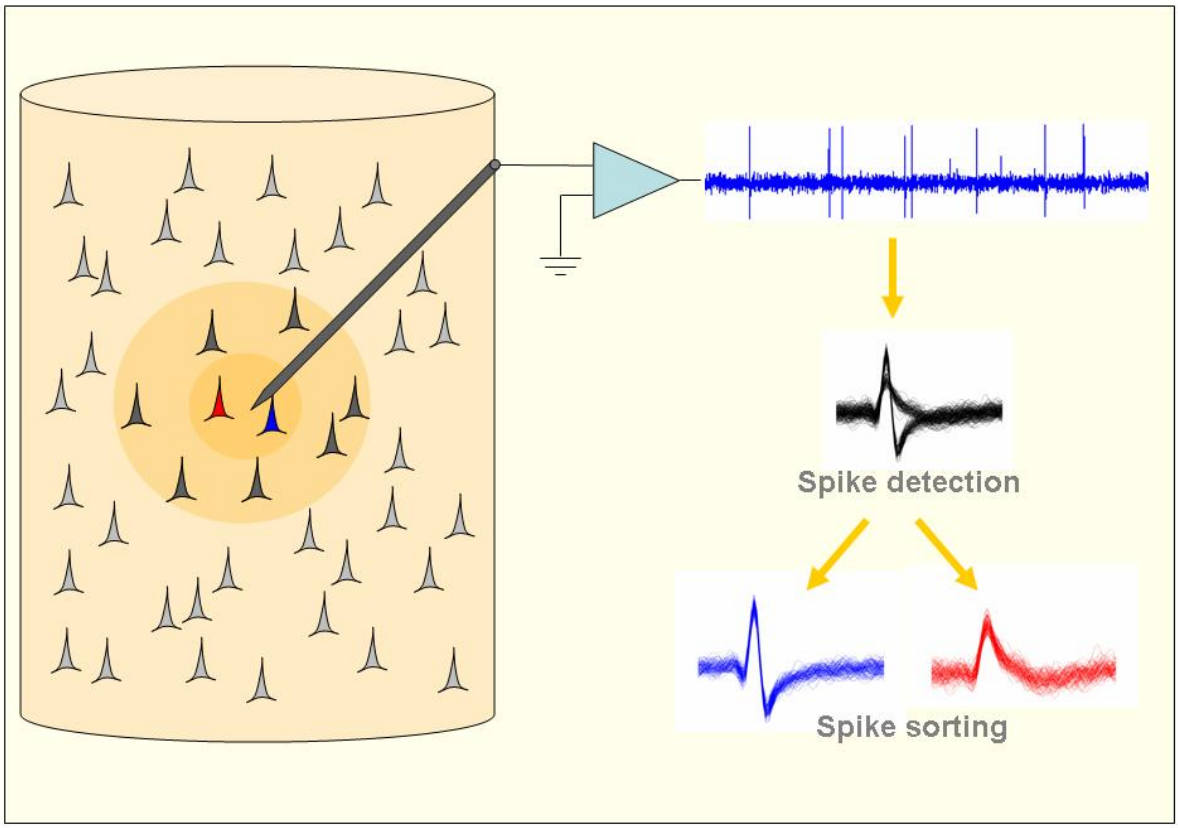

Figure 4.1: Extracellular recordings and spike sorting.
Extracellular potential is composed of the activity of many neurons surrounding the recording electrode (left). The recorded signal is amplified (blue "triangle") and band-pass filtered so that spiking activity of nearby neurons is distinguishable from the background activity (top right). The eAPs of the closest neurons (inner circle on the left, up to $\approx$ 50 μm from the electrode tip; Buzsáki, 2004) are detected via amplitude thresholding and sorted according to their shapes (single-unit activity). The eAPs can be detected for neurons located up to around 140 μm from the extracellular electrode (outer circle, left). However, their waveforms masked by the noise cannot be used to separate individual units.
From `http://www.scholarpedia.org/article/File:QQ_Fig1.jpg` by Rodrigo Quian Quiroga, used under the Creative Commons Attribution-NonCommmercial-ShareAlike 3.0 Unported licence. To view a copy of this licence, visit `https://creativecommons.org/licenses/by-nc-sa/3.0/deed.en_US`.

placed further away from the cell samples currents from a larger proportion of neuronal processes. All of this makes the interpretation of the extracellular AP waveforms rather difficult. Gold et al. (2006) established the main properties of eAP waveforms by fitting compartmental models of reconstructed CA1 pyramidal neurons to dual intra- and extracellular recordings from the same cells. The extracellular AP waveform consists of one to three peaks, which can be named according to the dominating currents that shape them: the capacitive peak, the sodium peak, and the potassium peak (Fig. 4.2 B).

The capacitive peak is the first positive peak and reflects axial currents from a propagating AP, which depolarize the membrane prior to sodium channel activation. Consequently, the capacitive peak is not visible at locations close to the spike initiation zone. For example, an AP initiated at the AIS does not exhibit an extracellular capacitive peak in the region of the basal dendrites; the capacitive peak develops and progressively increases in amplitude at recording locations along the main apical dendrite. So if the position of the extracellular electrode is known (for example, from the trace the electrode leaves in the tissue), the presence or absence of the capacitive peak provides information about the location of the spike initiation zone.

The sodium peak is a negative voltage deflection that corresponds to the AP-associated sodium current flow through the membrane. Typically, this is the dominant peak of the whole eAP. The sodium peak is usually missing only at very remote dendritic locations where the backpropagated AP is small and propagates passively. Here, the potassium peak is missing as well and the eAP waveform features a single positive (capacitive) peak. However, a passively propagating AP might also give rise to a biphasic eAP, where both the positive and the negative peak are capacitive.

The potassium peak is positive and follows the sodium peak. Gold et al. (2006) demonstrated that it can have a variety of shapes, depending on the type of potassium current responsible for membrane repolarization during the AP. The potassium peak is often missing at dendritic locations where the attenuated backpropagating AP does not reach amplitudes needed to activate a repolarizing potassium current (Fig. 4.2 C, waveform on the right).

Altogether, the extracellular AP waveform is a powerful source of information about various aspects of AP generation and propagation within a neuron. However, computational modeling is needed to disentangle the complex relationships between the membrane currents, pattern of AP initiation and the position of the extracellular recording electrode.

Extracellular correlates of spikelets

Chorev and Brecht (2012) performed dual intra- and extracellular recordings in CA1 pyramidal neurons *in vivo* and obtained extracellular correlates of AP and spikelet firing in these cells (Fig. 4.3). Their aim was to test the coupling (gap junction) hypothesis of spikelet origin, which states that spikelets arise from APs initiated in an electrotonically coupled cell.The authors found that intracellular spikelets were associated with an extracellular AP-like waveform, which they called SES – the secondary extracellular spike. They compared the timing of the SES waveform with the extracellular correlate of APs (PES – primary extracellular spike) and discovered that, in most cases, the first peak of the spikelet-associated SES slightly preceded the first peak of the AP-associated PES, when both events were aligned to the onset ("kink") of the intracellular events (Fig. 4.3 B, C). The authors interpreted this finding as evidence for the gap-junctional origin of spikelets, where the SES corresponds to an AP occuring in the coupled cell, which gives rise to the intracellularly recorded spikelet (Chorev and Brecht, 2012).

However, the dual extra- and intracellular data by Chorev and Brecht (2012) possibly carry further information about the mechanism of spikelet generation. Besides the small positive delays between the capacitive peaks of the spikelet- and AP-associated extracellular waveforms (SES and PES, respectively) introduced above, the data reveal a tendency for the amplitudes of

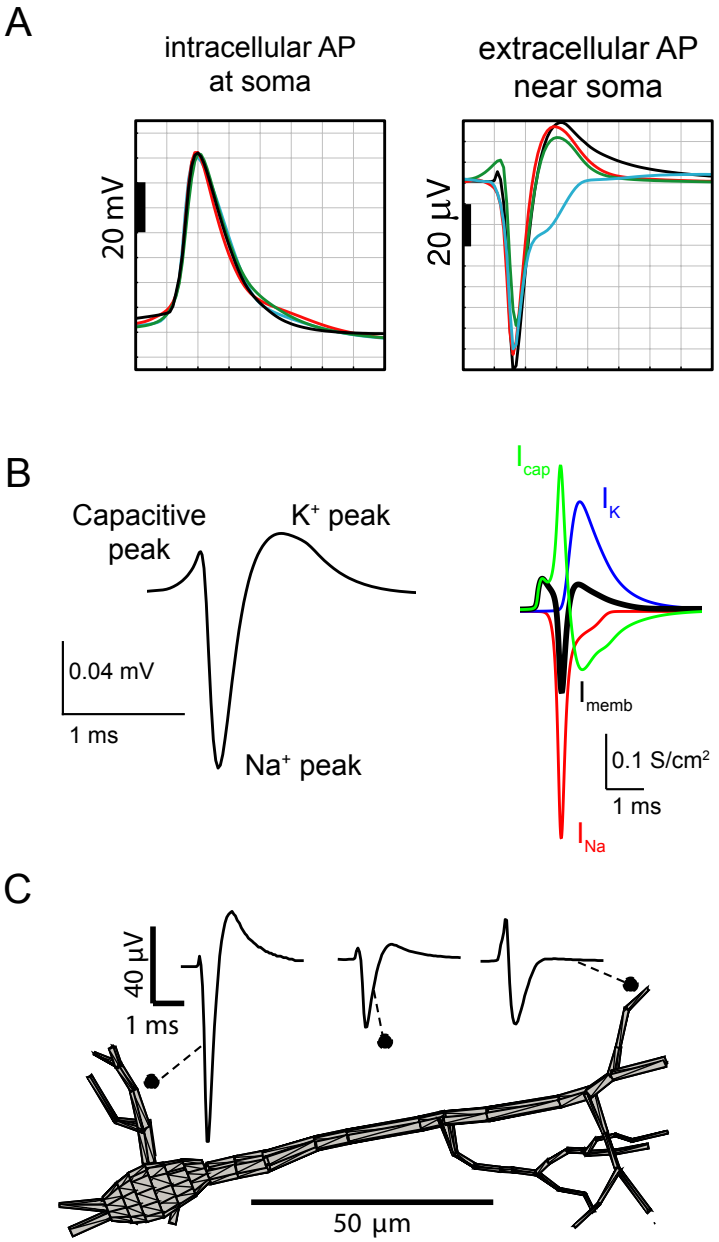

Figure 4.2: Features of the eAP waveform.
A Extracellular AP waveforms contain more information about the action currents than intracellular AP waveforms. Four models with different distributions of active conductancies show almost identical intracellular AP waveforms (left), whereas the extracellularly recorded waveforms differ substantially (right). **B** The three phases of extracellular AP waveforms (left) are named according to the dominating membrane current during each phase (right): capacitive current (green), sodium current (red) and potassium current (blue). **C** The shape of the extracellular AP waveform changes with the position of the recording electrode. A and C reprinted from Gold et al. (2007) with permission of Springer, all rights reserved. A: from Fig. 3 "Comparison of Intra and Extracellular Action Potentials for four conductance density models". B: from Fig. 4 "Details of simulation (A)".

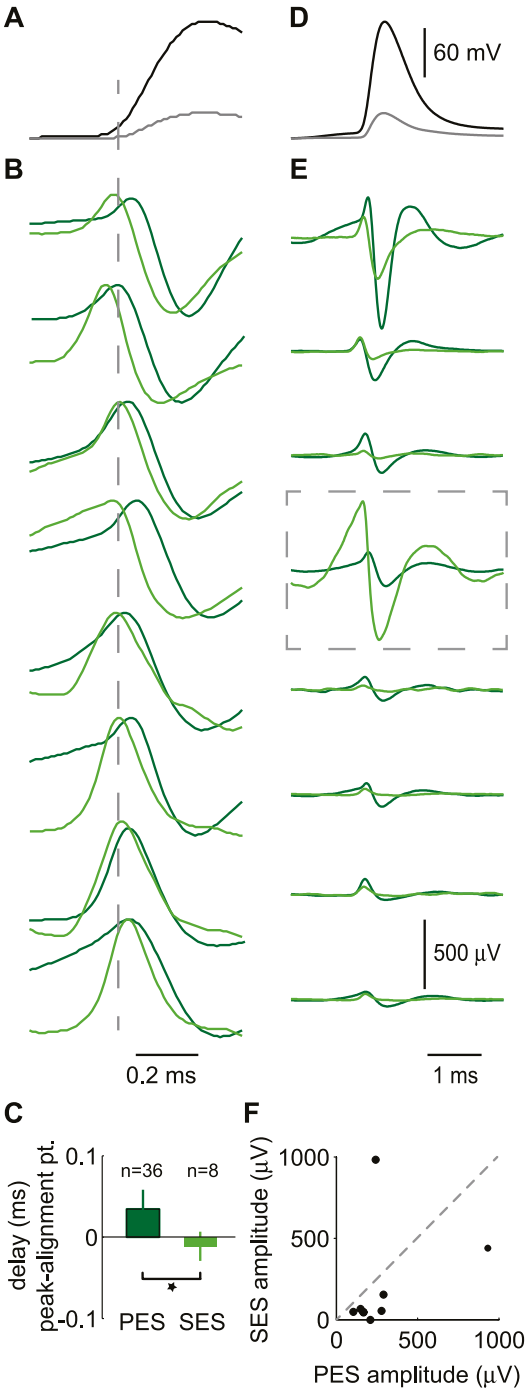

Figure 4.3: Extracellular correlates of APs and spikelets.
A+**D** Average intracellularly recorded AP (black) and spikelet (gray), aligned to the maximum curvature (dashed line in **A**). **B**+**E** Mean extracellular correlates of APs (PES, dark green) and spikelets (SES, gray) from eight cells, aligned according to the intracellular traces. Traces in **A**+**B** are stretched in time and waveforms in **B** have normalized amplitudes for a better comparison of the delays. **C** Delays between the capacitive peak and the alignment point for PES (dark green) and SES (light green). Shown are averages and the standard error of the mean. **F** The SES amplitude plotted against the PES amplitude from the same cell. Reprinted from Chorev and Brecht (2012), all rights reserved.

the SES to be smaller than the amplitudes of the PES, as well as a qualitative difference between the SES and PES waveforms recorded at the same location (Fig. 4.3). In this chapter, I am using computational modeling of extracellular waveforms associated with AP and spikelet firing to examine whether these data features are consistent with the single-cell model of spikelet origin (chapter 3), and how they constrain the gap-junction hypothesis of spikelet generation.

4.2 Methods

4.2.1 Calculation of extracellular potentials

Electric current generated by transmembrane flow of ions propagates in the extracellular space and gives rise to extracellular potential. The nature of the extracellular medium is typically considered to be purely resistive (Holt and Koch, 1999; Gold et al., 2006; Pettersen and Einevoll, 2008), and is described with an ohmic conductivity σ, which is a scalar, thus bearing the assumption of homogeneity and infinity of the extracellular medium.

Then, the extracellular potential Φ arising from a (time-dependent) point source of current $I(t)$ at a distance r from the recording site is defined by the quasistatic approximation to Maxwell's equation:

$$\Phi(r,t) = \frac{1}{4\pi\sigma}\frac{I(t)}{r} \tag{4.1}$$

In the case of neurons, however, membrane currents are not generated at a single point. Rather, they are dispersed over prolonged dendritic and axonal cables. Therefore, the approach of compartmental modeling is to divide neuronal processes into shorter segments and to consider each of these segments as a current source. The extracellular potential is then proportional to the linear sum of the individual current sources, weighted by their distances to the measuring site:

$$\Phi(r,t) = \frac{1}{4\pi\sigma}\sum_{n=1}^{N}\frac{I_n(t)}{r_n} \tag{4.2}$$

Equation 4.2 describes the *point-source approximation*, where the current generated by a segment is summed and placed in a single point in the middle of the segment. In the *line-source approximation*, the current generated by a segment is evenly distributed along the longitudinal axis of the segment (Holt and Koch, 1999).

So this forward modeling scheme of extracellular potentials consists of two steps: in the first step the transmembrane currents for each segment of the model neuron are computed, which are then used in the second step to calculate the extracellular potential. It is assumed that the extracellular potential is weak enough so its influence on the membrane currents can be neglected.

4.2.2 Simulations of extracellular waveforms

To simulate extracellular potentials, I used the line-source approximation implemented in the Python package LFPy (Lindén et al., 2013; Figs 4.5, 4.6 and 4.4). However, this package does not support simulations of connected neurons. To generate extracellular potentials of electrotonically coupled cells, I implemented in Python a point-source approximation algorithm to calculate extracellular potentials from transmembrane currents computed in NEURON (Carnevale and Hines, 2006) (Figs 4.8–4.15). The LFPy package was utilized here to plot the neuronal morphologies.

In these simulations, I used the layer V pyramidal neuron model from Hu et al. (2009) with the same modifications as described in chapter 3. The sodium channel densities were reduced in the single-cell simulations, but not in the simulations of two electrotonically coupled cells. The APs were generated by setting the reversal potential of leak current (E_{pas}) to 0 mV in the somato-dendritic compartments. This mimicks distributed synaptic inputs and generates an AP without a stimulation artifact that would distort the extracellular traces (Gold et al., 2006).

Orthodromic and antidromic spikelets in the single-cell scenario could be evoked by setting the leak reversal (E_{pas}) in the whole cell to -20 mV and -55 mV, respectively, and by removing the sodium channels from the axon hillock and the somato-dendritic compartments. In Fig. 4.4, an orthodromic spikelet generated with this manipulation is compared to an orthodromic spikelet resulting from somatic current injection of 6.8818 nA for the duration of 0.5 ms. It follows that the capacitive peak used for quantitative analysis in this study is almost identical in both cases.

Electrotonic coupling of two (identical) cells was modelled with a symmetric, purely resistive (ohmic) gap junction with a junctional resistance of 30 MΩ. For axonal coupling sites, somatic spikelets were generated by setting the leak reversal (E_{pas}) and the initial membrane voltage to -80 mV in both cells (except the somato-dendritic compartments of the cell firing an AP, where $E_{\text{pas}} = 0$ mV as stated above), as the default value of -70 mV resulted in somatic APs.

The extracellular waveforms were simulated at 8x6 recording positions on a grid with 30 μm spacing situated 20 μm above the plane containing the soma and the axon. The simulations were run with a fixed time step of 0.01 ms.

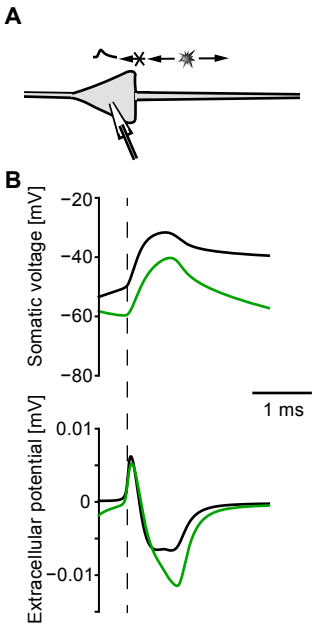

Figure 4.4: Extracellular waveforms of orthodromic spikelets.
A A sketch of the simulation scenario. Orthodromic spikelets are generated in a single cell as APs initiated at the AIS that fail to activate the soma. **B** Comparison of spikelet waveforms evoked with E_{pas} manipulation (black; see Methods) and with somatic current injection (green) in the Hu-model. Shown are somatic intracellular waveforms (top) and extracellular waveforms (bottom), aligned to the intracellular kinks (dashed lines).

For the results shown in Figs 4.7 and 4.16, I simulated extracellular fields of a CA1 pyramidal neuron model 'd151', provided with the extracellular simulation package EAPS (Gold et al., 2006, 2007; ModelDB accession number 84589). Unlike the "Hu-model" used in previous

simulations, the "Gold-model" allows to generate dendritic sodium spikes that propagate to the soma (Gold et al., 2006).

The results shown in Fig. 4.7 were simulated with the provided parameter set "D" with the following changes: default sodium channel density (gna_default) 0.03 S/cm^2; sodium channel density at the axon hillock (gna_hill) 5*gna_default; sodium channel density at the AIS (gna_iseg) 10*gna_default. For the spikelet, sodium channels were removed from the somato-dendritic compartments.

Spikelet waveforms shown in Fig. 4.16 were simulated with the provided parameter set "A", but sodium channels were removed from the axon hillock and the activation curve of somatic sodium channels was shifted to the right by 8 mV (vhalf_m_naf = -38 mV), so that the voltage shift between somatic and axonal channels became 13 mV (like in the Hu-model), instead of the original 5 mV. The individual curves in Fig. 4.16 differ in the following parameters: red: like described above; black: like red, plus the inactivation curve of the axonal sodium channels was shifted to the left by 4 mV (vhalf_h_nax = -54 mV); blue: like red, but the shift in the activation curves between somatic and axonal sodum channels was reduced to 10 mV (vhalf_m_naf = -41 mV) and sodium channels were removed from the dendrites; magenta: like blue, but additionally, sodium channels were removed also from the soma. The aim of these parameter variations was to demonstrate the relationship between the sodium currents and the extracellular and intracellular waveform of spikelets.

To evoke APs and spikelets in the Gold-model, reversal potential and conductivity of the leak current were transiently increased like in the original study (Gold et al., 2006, 2007): in dendritic compartments at distance 50 μm or more from the soma (for the spikelets and APs initiated at the AIS; like in the parameter set "A") and in distal apical dendrites 500 μm or more away from the soma (for the dendritic AP; like in the parameter set "D"). The simulations of the Gold-model were run with variable time steps and a maximum time step of 0.025 ms.

4.2.3 Data analysis

To compare the timing of the extracellular waveforms, the intracellular events were aligned to the maximum of the 2nd voltage derivative (the "kink") and the extracellular events were aligned accordingly. Shouldered APs featured two maxima of the 2nd derivative in their rising phase: one was associated with the transition from the subthreshold depolarization to the shoulder (the actual kink), the other one occured at the transition from the shoulder to the somato-dendritic potential. When such an AP was transmitted through a gap junction, the resulting spikelet also exhibited two "kinks". The first one was typically hardly visible in the voltage trace. Nevertheless, I aligned both events to the 1st kink to be able to compare the relative timing of the extracellular events.

To quantify the delays between the PES and SES in the electrotonic coupling scenarios, I compared relative delays of the sodium peaks. I did not consider the delays of the capacitive peaks as was done in Chorev and Brecht (2012) because in some of the simulation scenarios, the capacitive peaks very broad or missing. On the other hand, the sodium peaks always appeared sharp and clean. In the electrotonic coupling simulations, the contribution of the "spikeleting" cell (i.e., the cell firing a spikelet) to the extracellular field was calculated from the transmembrane currents of this one cell only.

4.3 Results

The dual intra- and extracellular data of Chorev and Brecht (2012) identified extracellular correlates of spikelet firing *in vivo*. To understand the potential implications of this data for the mechanism of spikelet generation, I simulated extracellular fields associated with AP- and spikelet

firing in compartmental models of pyramidal neurons. In the first part, I concentrated on extracellular waveforms of APs and spikelets generated within a single cell. In the second part, I analyzed extracellular fields of two neurons coupled by a gap junction.

4.3.1 Extracellular fields of APs and spikelets generated in a single cell

Large-amplitude somatic spikelets can be evoked in a single pyramidal model neuron as APs initiated at the AIS that fail to activate the soma (chapter 3). The top panel in Fig. 4.5 B shows a somatically recorded AP (red) and an orthodromic spikelet (black) generated in a pyramidal cell model (the Hu-model, see Methods), both aligned to the onset of the events (maximum curvature – the "kink"). The bottom panel in Fig. 4.5 B depicts extracellular waveforms of the AP (red, eAP) and the spikelet (black, eSpikelet), recorded close to the soma (boxed traces in Fig. 4.5 C). Compared to the eAP, the eSpikelet amplitude was smaller at all recording locations (Fig. 4.5 C) with a diminished Na-peak and a missing K-peak, which fits well to the experimental data (Chorev and Brecht, 2012). The capacitive peaks of the eAP and eSpikelet waveforms coincided when aligned to the onsets of the intracellular events. In the experimental data, one of the shown PES-SES pairs (Fig. 4.3 E, second from the top) had a similar appearance including the coinciding capacitive peaks. In my simulations, this coincidence resulted from the perfect match of the shoulder of the AP and the rising phase of the spikelet (Fig. 4.5 B). Consequently, the delays between the capacitive peak and the intracellular kink were identical for APs and orthodromic spikelets.

Negative kink-peak delays were possible for antidromic spikelets, i.e., for spikelets evoked in the distal axon that propagated antidromically towards the soma, but failed to activate the soma (Fig. 4.6). Nonetheless, these small negative delays occured at recording locations in the basal dendritic tree close to the AIS, where orthodromic APs and spikelets did not feature a capacitive peak at all (Fig. 4.6 C).

Chorev and Brecht (2012), however, considered full-blown APs, not shouldered APs as is the case in these simulations. The shoulder reflects somatic invasion of the axial currents from the AP initiated at the AIS. In a simplified model (Fig. 3.3, chapter 3), we showed that fb-APs initiated at the soma arise smoothly from the subthreshold depolarization and do not exhibit a "kink", which is consistent with experimental observation in motoneurons when the sodium channels at the AIS are inhibited by the action of serotonin (Cotel et al., 2013). Another way to generate fb-APs might be APs initiated in the apical dendrites that propagate to the soma. Unlike the AIS-soma transition, the primary apical dendrite leads smoothly to the soma, providing a possibility to mask the transition between the "shoulder" from dendritic axial currents and the somatic action currents.

Because the Hu-model does not support the propagation of dendritic APs into the soma, I simulated dendritic APs in a CA1 pyramidal-cell model from Gold et al. (2006, 2007). Figure 4.7 B shows a comparison of intracellular and extracellular waveforms of a dendritically evoked AP (blue), an AP initiated at the AIS (red), and a spikelet (black). Like in the Hu-model (Fig. 4.5), the capacitive peaks of the AIS-AP and spikelet coincided. In contrast, the capacitive peak of the dendritic AP was larger and occured later than the capacitive peak of the spikelet. It resembled the slowly-ramping capacitive peak of one of the experimentally recorded PESs (Fig. 4.3 E, top row).

In summary, I demonstrated that spikelets generated in a single pyramidal model neuron as APs initiated at the AIS are visible in the extracellular space. The shape of eSpikelets qualitatively matched the shape of SESs recorded experimentally (Chorev and Brecht, 2012). At all recording locations, the amplitudes of eSpikelets were smaller than the amplitudes of eAPs. The capacitive peaks of a sh-AP and a spikelet coincided, but the capacitive peak of a fb-AP occured later than the capacitive peak of a spikelet. Consequently, the mechanism of spikelet

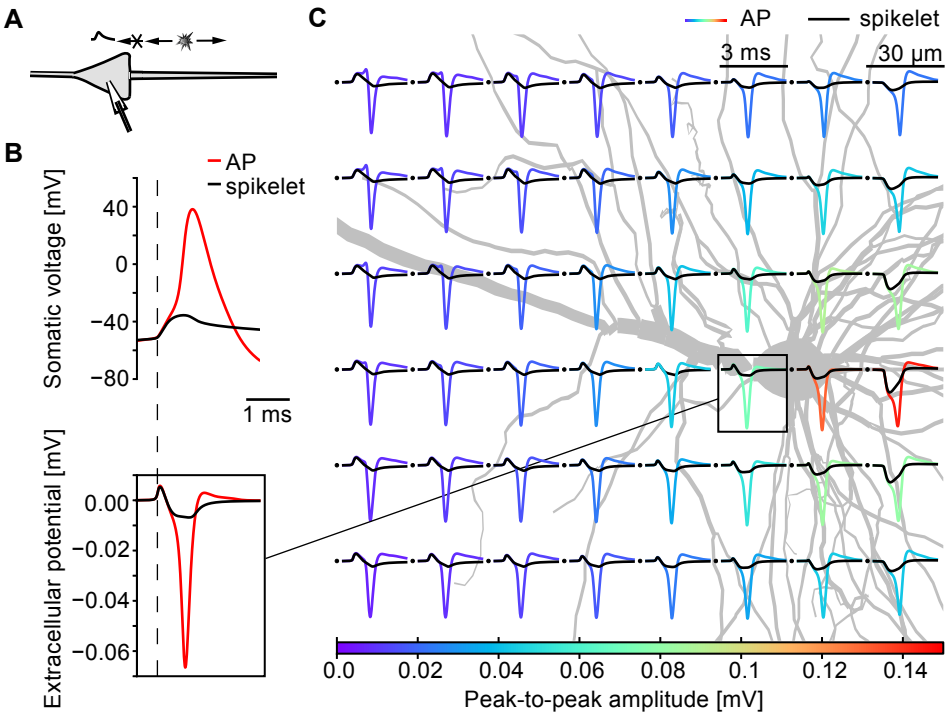

Figure 4.5: Extracellular fields of APs and spikelets generated in a single cell.
A A sketch of the simulation scenario. Orthodromic spikelets were generated in a single cell as APs initiated at the AIS (gray star) that failed to activate the soma. AP propagation is denoted with arrows. **B** top: A somatically recorded AP (red) and a spikelet (black). Both events are aligned to the maximum of the 2nd derivative (dashed line, the "kink"). Bottom: Extracellular waveforms correlated with the AP (red, eAP) and with the spikelet (black, eSpikelet), aligned to the corresponding intracellular events (dashed line). **C** Waveforms of eAPs (color) and eSpikelets (black), recorded on a grid like in Fig. 4.8. The color code denotes the peak-to-peak amplitude of the eAP. Waveforms of eSpikelet were scaled accordingly. The box marks the traces shown in **B**.

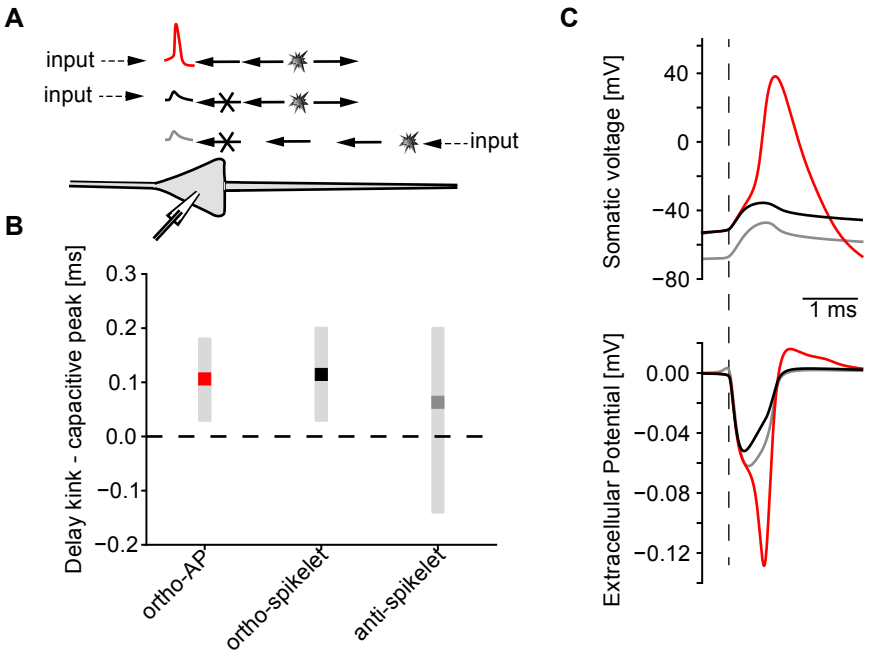

Figure 4.6: Delays of APs and spikelets generated in a single cell.
A A sketch of the simulation scenario. Orthodromic APs (red) and orthodromic spikelets (black) are initiated at the AIS. Antidromic spikelets are initiated in the distal axon. Dashed arrows denote subthreshold input, solid arrows denote AP propagation and the gray star marks the location of AP initiation. **B** Delays between the kink of the intracellular event and the maximum of the capacitive peak of the corresponding extracellular waveform for orthodromic APs (red), orthodromic spikelets (black) and antidromic spikelets (gray). Shown are mean delays (squares) and delay ranges (gray bars) for waveforms recorded on a 8x6 grid placed like in Fig. 4.5. **C** top: A somatically recorded orthodromic AP (red), an orthodromic spikelet (black), and an antidromic spikelet (gray), aligned to the maximum of the 2nd derivative (dashed line, the "kink"). Bottom: Extracellular waveforms of the AP (red), orthodromic spikelet (black), and antidromic spikelet (gray), recorded in the region of basal dendrites, ca. 30 μm from soma. The traces are aligned to the corresponding intracellular events (dashed line).

generation in a single cell as described in chapter 3 is consistent with the dual-recording data by Chorev and Brecht (2012).

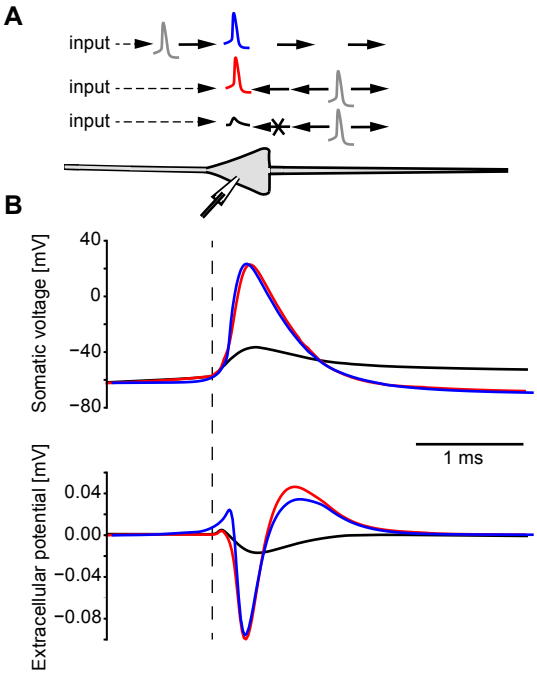

Figure 4.7: Extracellular waveforms of dendritic APs in the Gold-model.
A A sketch of the simulation scenario. Dendritic APs (blue) were initiated in the apical dendrites. Orthodromic APs (red) and orthodromic spikelets (black) were initiated at the AIS. Dashed arrows denote subthreshold input, solid arrows denote AP propagation, and the gray AP waveform marks the location of AP initiation. **B** top: A somatically recorded dendritic AP (blue), an orthodromic AP (red), and a spikelet (black). All events were aligned to the maximum of the 2nd derivative (dashed line, the "kink"). Bottom: The extracellular waveforms associated with the dendritic AP (blue), orthodromic AP (red), and the spikelet (black), aligned to the corresponding intracellular events; measured ≈ 30 μm away from the soma.

4.3.2 Gap-junctional coupling and extracellular fields of APs and spikelets

When two neurons are coupled by an electrical synapse – a gap junction – an AP evoked in the first (prejunctional) cell is transmitted into the second (postjunctional) cell and appears there as a spikelet. I investigated the effects of the cellular location of the gap junction and the relative position of the coupled cells on timing and amplitude ratio of extracellular correlates of APs and spikelets.

Somata close together

Two identical pyramidal model cells (the Hu-model, see Methods) were coupled by a somatic gap junction (Fig. 4.8). The somata were positioned close to each other as suggested by dye coupling data (Mercer et al., 2006; Wang et al., 2010) and one of the cells — cell 1 — was recorded intracellularly (Fig. 4.8 A). Fig. 4.8 compares two simulations: in the first simulation, an AP was evoked in cell 1 and appeared in cell 2 as a spikelet. This gave rise to an extracellular waveform

that can be called PES, the primary extracellular spike, in parallel to the naming conventions in Chorev and Brecht (2012). In the second simulation, an AP was evoked in cell 2 and manifested as a spikelet in cell 1. The associated extracellular waveform can be called SES, the secondary extracellular spike (Chorev and Brecht, 2012). Fig. 4.8 B shows an AP (red) and a spikelet (black) intracellularly recorded in cell 1, both aligned to the maximum curvature (the "kink"). The amplitude of the intracellular spikelet was small (< 5 mV) because of the strong low-pass filtering by the soma of the postjunctional neuron. The bottom panel of Fig. 4.8 B depicts the PES (red) and SES (black) recorded close to the soma of cell 1 (boxed traces in Fig. 4.8 C). The extracellular waveforms were aligned according to the intracellular events, like in Chorev and Brecht (2012). With such an alignment, the SES was slightly shifted to earlier times compared to the PES, so the capacitive peak of the SES slightly preceded the capacitive peak of the PES, which is in line with the findings in Chorev and Brecht (2012). As expected, the extracellular field was dominated by the cell firing the AP, but the cell featuring the spikelet contributed as well (gray trace in Fig. 4.8 C). The spikelet contribution, nonetheless, did not visibly manifest in the extracellular waveform because it (i.e., its prominent capacitive peak) coincided with the sodium peak of the eAP. Extracellular fields recorded on a grid above the coupled neurons (Fig. 4.8 C) revealed that the PES-SES amplitude ratio strongly depended on the recording location. If an extracellular recording electrode was placed in the vicinity of the coupled cells, the probability that the amplitude of the PES was larger than the amplitude of the SES ("PES $>$ SES") was equal to the probability "SES $>$ PES". (An exception would be very close distances of < 20 μm between the intracellular and extracellular electrode, where the soma of cell 2 would constrain the placement of the extracellular electrode, resulting in a higher probability of PES $>$ SES.) This "equal probability" was a consequence of the close apposition of the two coupled cells, as was the similarity of the PES and SES shapes at any given recording location.

Consistently, placing the gap junction in the axon instead of the soma did not change the PES-SES amplitude ratios, nor the similarity of the PES and SES waveforms (Fig. 4.9 C). However, unlike in the somatic coupling scenario, the AP propagated actively in the axon of the postjunctional cell and failed at the axon-soma boundary, similarly to spikelets generated in a single cell (Fig. 3.9). As a consequence, the intracellularly recorded spikelet was substantially larger than the spikelet resulting from somatic coupling (Fig. 4.9 B), and the contribution of the spikeleting cell was clearly visible in the extracellular field (Fig. 4.9 C).

Delays between the PES and SES depend on the cellular location of the gap junction: distal gap junctions lead to larger delays because the spikelet has to travel larger distance from its origin as an AP in the prejunctional AIS to the soma of the postjunctional cell. Since the SES waveform is dominated by the AP propagation in the prejunctional cell, but it is aligned to the postjunctional spikelet, it appears earlier in time than the PES. Fig. 4.10 shows sodium-peak delays between PES and SES for different locations of the gap junction, revealing that small positive delays (< 0.1 ms; Chorev and Brecht, 2012; Fig. 4.3) occured for proximal gap junctions located between ≈ 50 μm in the dendrites up to ≈ 140 μm in the axon. An exception was coupling close to the spike initiation zone at the end of AIS ($\approx 50 - 60$ μm away from soma), which gave rise to zero or even small negative delays.

To summarize, proximally placed gap junctions generated small positive delays between the PES and the SES that fit the experimental data by Chorev and Brecht (2012). However, when the somata of the coupled cells were located close to each other, there was an equal probability that the amplitude of the SES is larger than the amplitude of the PES and vice versa. In the experimental data, in only one of the $n = 8$ cases is the SES larger than the PES. This result has a 3% probability to occur when the underlying probabilities of SES $>$ PES and PES $>$ SES are equal. Additionally, the shapes of the simulated PESs and SESs at a given recording location appeared qualitatively similar. The last two points are consequences of the close somatic apposition of the coupled cells and disagree with the experimental data.

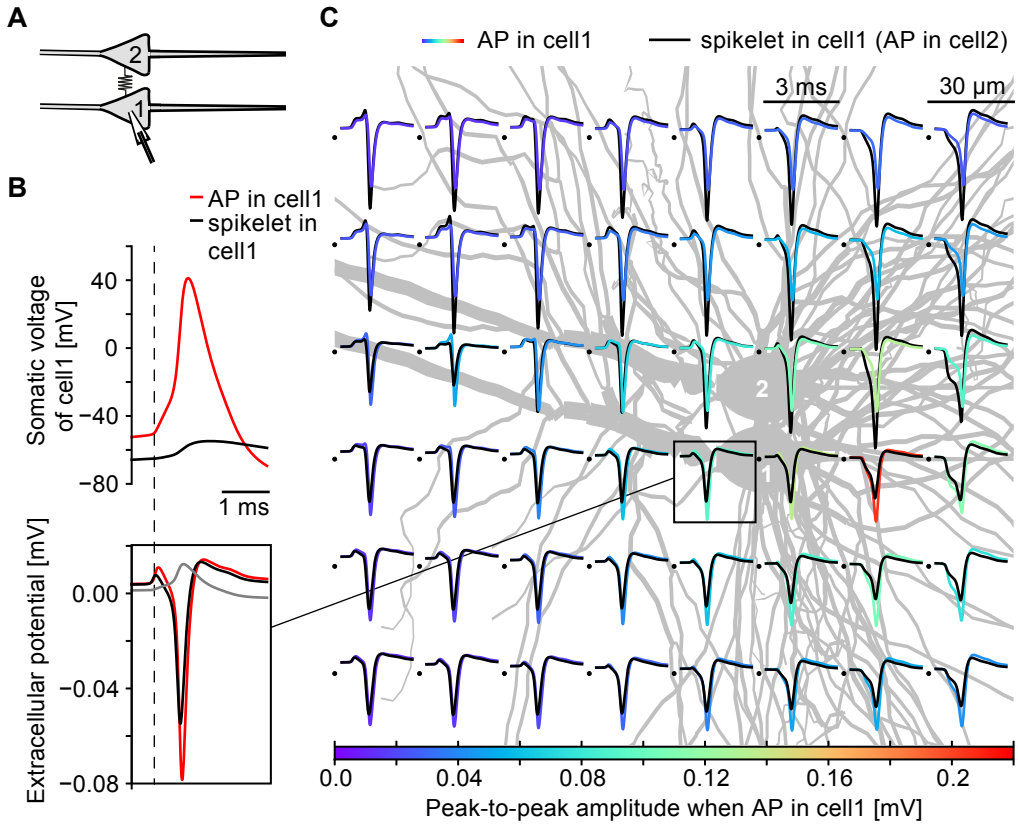

Figure 4.8: Extracellular fields of somatically coupled pyramidal neurons with close-by somata. **A** A sketch of the simulation scenario. The cells were connected with a somatic gap junction. The lower cell 1 was recorded intracellularly. **B** top: Somatic intracellular voltage traces; an AP (red) evoked in the recorded cell 1 and a spikelet (black) originating from an AP evoked in the coupled cell 2. Both events were aligned to the maximum of the 2nd derivative (dashed line, the "kink"). Bottom: Extracellular waveforms correlated with the AP (red, PES) and with the spikelet (black, SES). The contribution of the spikeleting cell (cell 1) to the extracellular waveform (black) is shown in gray. The SES (black) was slightly shifted to earlier times compared to PES (red). All traces were aligned according to the intracellular events (dashed line). **C** Extracellular waveforms recorded on a grid (black dots) during the occurrence of an AP (color, PES) and a spikelet (black, SES) in the intracellularly recorded cell (cell 1). The color code denotes the peak-to-peak amplitude of the AP-associated waveform (PES). The spikelet-associated waveform (SES) was scaled accordingly. The box marks the traces shown in **B**. Note that the amplitude ratio between the PES and the SES depended on the recording location.

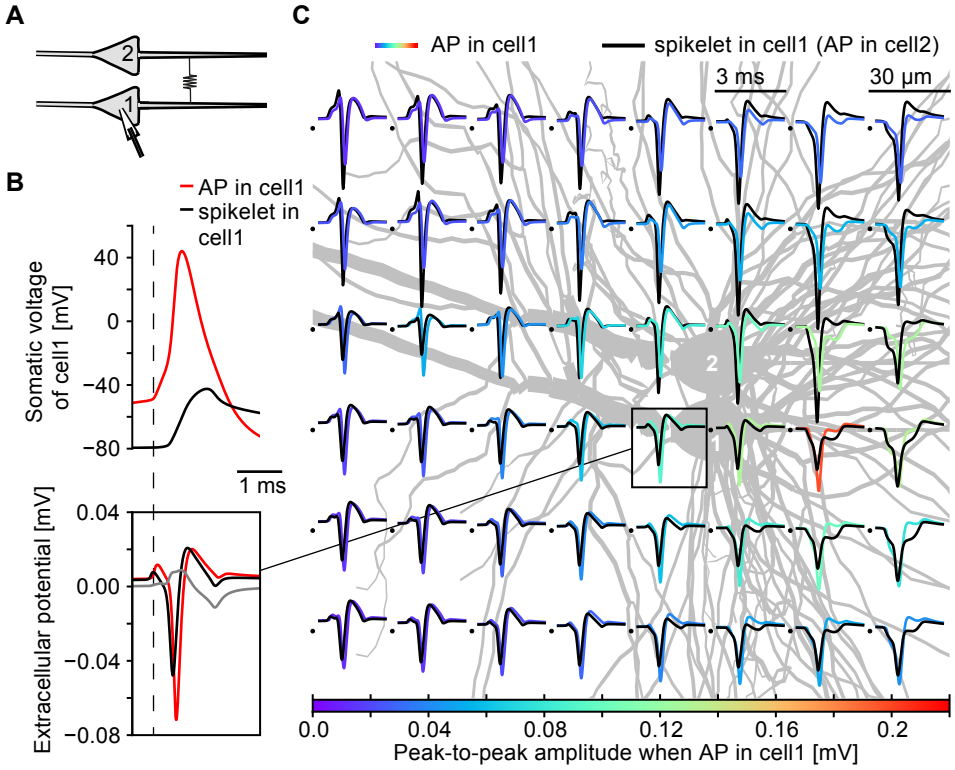

Figure 4.9: Extracellular fields of axonally coupled pyramidal neurons with close-by somata. **A** A sketch of the simulation scenario. The cells were connected by an axonal gap junction located 110 μm away from the somata. The lower cell (cell 1) was recorded intracellularly. **B** + **C** like in Fig. 4.8: **B** top: An intracellularly recorded AP (red) and a spikelet (black), which had a larger amplitude than the spikelet in Fig. 4.8. Bottom: Extracellular waveforms correlated with the AP (red, PES) and with the spikelet (black, SES). Contribution of the spikeleting cell (cell 1) to the extracellular waveform (black) is shown in gray. The SES (black) was slightly shifted to the left compared to PES (red). **C** Extracellular waveforms correlated with the AP (color, PES) and the spikelet (black, SES), recorded on a grid (black dots). Similarly to Fig. 4.8, the amplitude ratio between the PES and the SES depended on the recording location.

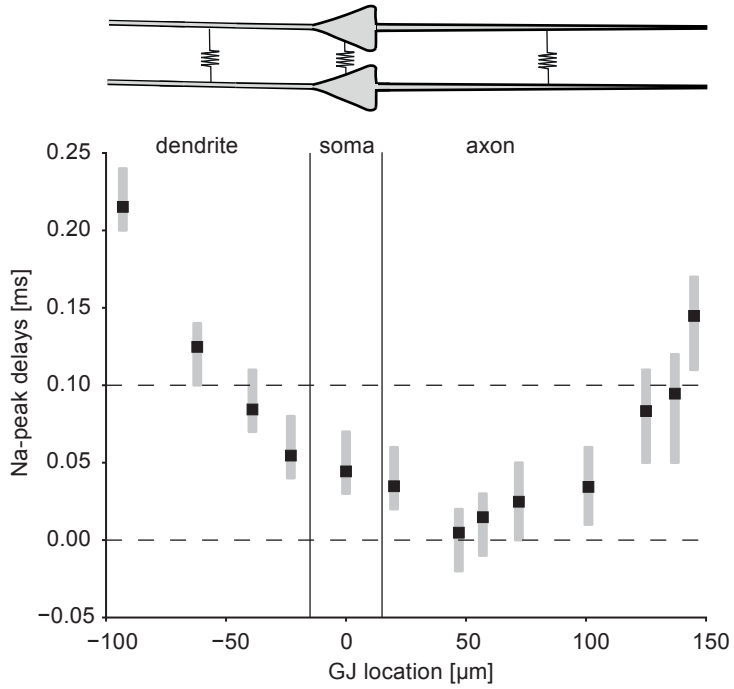

Figure 4.10: Sodium-peak delays between PES and SES for different positions of the gap junction.
Top: A sketch of the two coupled cells with neighboring somata. Bottom: Mean delays (black squares) and delay ranges (gray bars) for waveforms recorded on a 8x6 grid like in Figs 4.8 and 4.9. Small positive delays (< 0.1 ms) occured for proximal gap junctions, located between ≈ 50 μm in the dendrites up to ≈ 140 μm in the axon. Note the negative delays for axonal gap junctions close to the AP initiation site ($\approx$ 50–60 μm from soma).

Somata separated in space

To be able to generate different shapes and amplitudes of PES and SES, as observed experimentally (Chorev and Brecht, 2012), I simulated two coupled cells shifted by 80 μm along their longitudinal axis (Fig. 4.11 A). This shift fits to the anatomy of the CA1 pyramidal cell layer, which is $\approx$ 120 μm wide (Mizuseki et al., 2011).

Fig. 4.11 shows extracellular fields of such shifted cells connected by a proximal dendritic gap junction. If the *superficial* cell 1 (shifted towards the apical dendrites of cell 2) was recorded intracellularly, the SES exhibited smaller amplitudes than the PES at most recording locations around cell 1 (Fig. 4.11 C). Moreover, the SES waveforms differed qualitatively from the PES waveforms in the same way as in the data by Chorev and Brecht (2012): the SES showed a reduced sodium peak and a missing the potassium peak. On the other hand, the capacitive peak was rather wide and flat (Fig. 4.11 B), and the intracellularly recorded spikelet was even smaller and broader than the spikelet generated by somatic coupling (Fig. 4.8).

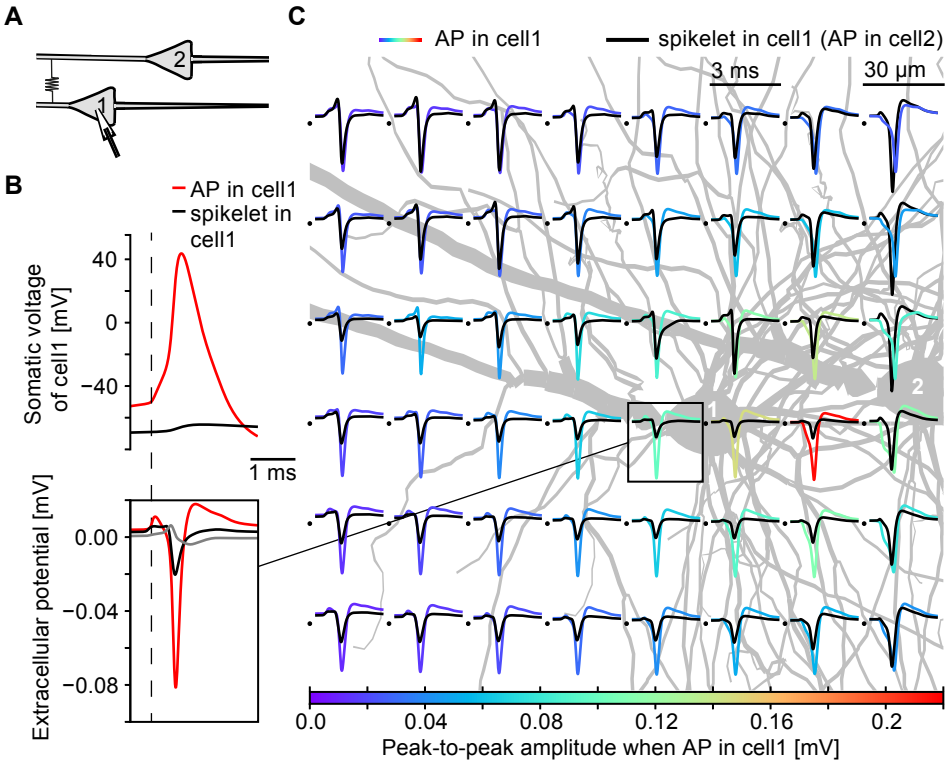

Figure 4.11: Extracellular fields of dendritically coupled neurons shifted along the longitudinal axis.
A A sketch of the simulation scenario. Distance between the midpoints of the somata was 80 μm. The cells were connected by a dendritic gap junction located 8 μm away from the soma of the closer cell 1. The lower cell 1 is recorded intracellularly. **B** + **C** like in Fig. 4.8: **B** top: An intracellularly recorded AP (red) and a spikelet (black) with a small amplitude. Bottom: Extracellular waveforms correlated with the AP (red, PES) and with the spikelet (black, SES). Contribution of the spikeleting cell (cell 1) to the extracellular waveform (black) is shown in gray. The sodium peak of the SES (black) was slightly shifted to the left compared to the PES (red). **C** Extracellular waveforms correlated with the AP (color, PES) and the spikelet (black, SES), recorded on a grid (black dots). The SES amplitudes are smaller than the PES amplitudes at most electrode locations.

Proximal axonal coupling of such shifted cells gave rise to large-amplitude intracellular spikelets (Fig. 4.12). However, the spikeleting cell strongly influenced the extracellular field and created a second negative peak in the SES. The sodium-peak delays, on the other hand, fitted the experimental data for proximal dendritic gap junctions as well as for axonal gap junctions located ≈ 50–90 μm from the closer cell (Fig. 4.13).

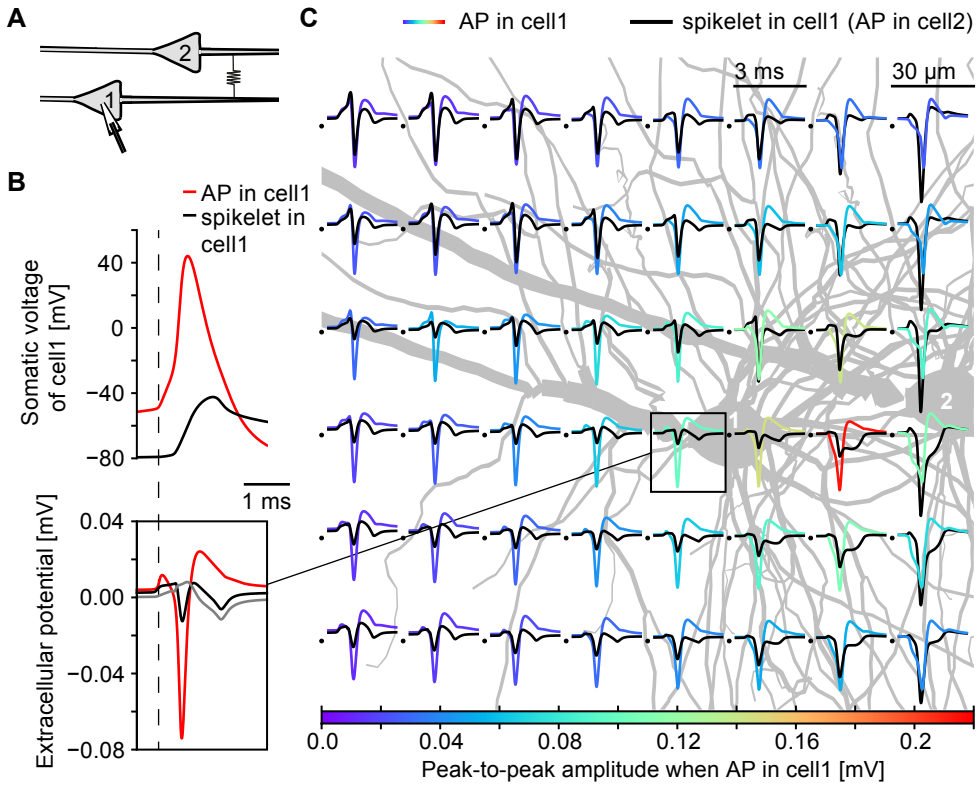

Figure 4.12: Extracellular fields of axonally coupled neurons shifted along the longitudinal axis.
A A sketch of the simulation scenario. Distance between the midpoints of the somata was 80 μm. The cells were connected by an axonal gap junction located 57 μm away from the soma of the closer cell 2. The lower cell 1 was recorded intracellularly. **B** + **C** like in Fig. 4.8: **B** top: An intracellularly recorded AP (red) and a spikelet (black) with a large amplitude. Bottom: Extracellular waveforms correlated with the AP (red, PES) and with the spikelet (black, SES). Contribution of the spikeleting cell (cell 1) to the extracellular waveform (black) is shown in gray. **C** Extracellular waveforms correlated with the AP (color, PES) and the spikelet (black, SES), recorded on a grid (black dots). The SES amplitudes are smaller than the PES amplitudes at most electrode locations.

Such a longitudinal shift of the coupled neurons introduced an asymmetry in the appearance of the PES-SES pairs. If the *deep* cell 2 (i.e., shifted towards basal dendrites of cell 1) was recorded intracellularly, the SES shape was much more irregular (complex) with multiple peaks and strongly depended on the recording location for dendritic (Fig. 4.14) as well as for axonal coupling (Fig. 4.15).

In summary, two coupled neurons shifted along their main axis can explain the apparently higher probability of PES amplitudes being larger than the SES amplitudes. Small positive delays occured for coupling at proximal dendritic and axonal sites. However, dendritic coupling resulted in too small intracellular amplitudes of spikelets, and axonal coupling generated com-

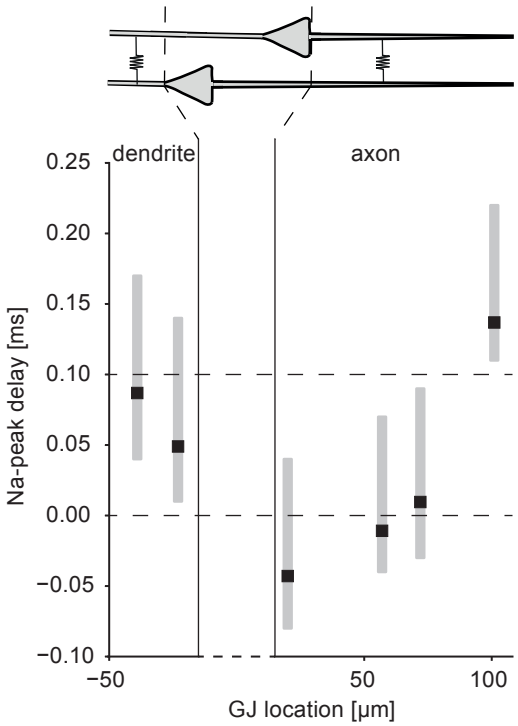

Figure 4.13: Sodium-peak delays between the PES and SES for different positions of the gap junction, cells shifted.
Top: A sketch of the two coupled cells. The distance between the midpoints of the somata was 80 μm. Bottom: Mean delays (black squares) and delay ranges (gray bars) for waveforms recorded on a 8x6 grid when the lower cell was recorded intracellularly, like in Figs 4.11 and 4.12. Small positive delays (< 0.1 ms) occured for proximal dendritic gap junctions and for axonal gap junctions located $\approx$ 50–90 μm away from the closer soma.

plex extracellular waveforms with multiple peaks. Moreover, if the "deep" cell was recorded intracellularly, the extracellular waveforms became even more complex.

Hence, neither of the presented coupling scenarios could account for all aspects of the experimental data. Nevertheless, the modeling results point to a plausible scenario: the large intracellular amplitudes of experimentally recorded spikelets fit to axonal coupling, but not to somatic or dendritic coupling. In the case of axonal coupling, the contribution of the spikeleting cell to the extracellular field is biphasic, with distinct capacitive and sodium peaks that resemble the experimentally recorded SES waveforms (Fig. 4.3; Chorev and Brecht, 2012). At the same time, the axonal gap junction can be located relatively distant to the soma (> 200 μm of summed soma-axon distances of both cells) and still produce realistic (i.e., small) PES-SES delays, because of the AP initiation zone at the distal AIS and fast AP conduction in the axon. The width of the pyramidal cell layer (≈ 120 μm; Mizuseki et al., 2011) constrains the possible longitudinal distances between the somata, but if the axonally coupled cells were laterally remote from each other (> 140 μm; Buzsáki, 2004), the extracellular electrode located near the intracellularly recorded cell would pick up just the signal from this cell. In this case, the PES would correspond to the extracellularly recorded AP (eAP) and the SES would reflect the extracellularly recorded spikelet (eSpikelet). Such a scenario is practically indistinguishable from a single-cell case with spikelets evoked in the axon and antidromically propagating to the soma.

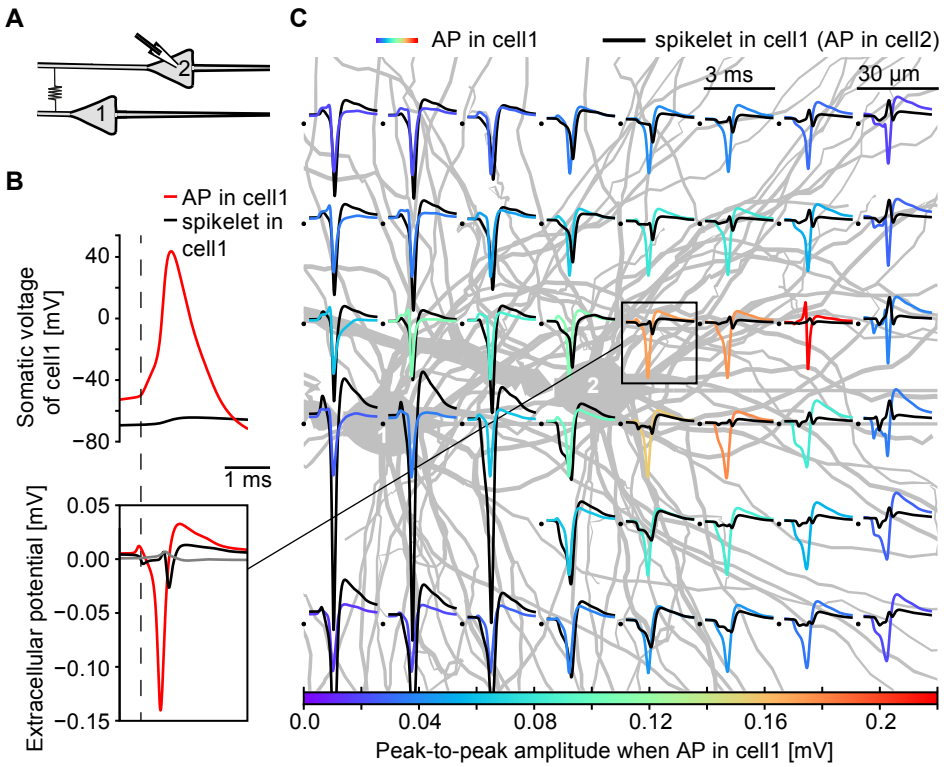

Figure 4.14: Extracellular fields of dendritically coupled neurons shifted along the longitudinal axis like in Fig. 4.11, but the upper cell (cell 2) was recorded intracellularly.
A A sketch of the simulation scenario. Distance between the midpoints of the somata was 80 μm. The cells were connected by a dendritic gap junction located 8 μm away from the soma of the closer cell 1. **B** + **C** like in Fig. 4.8: **B** top: An intracellularly recorded AP (red) and a spikelet (black) with a small amplitude. Bottom: Extracellular waveforms correlated with the AP (red, PES) and with the spikelet (black, SES). Contribution of the spikeleting cell (cell 2) to the extracellular waveform (black) is shown in gray. **C** Extracellular waveforms correlated with the AP (color, PES) and the spikelet (black, SES), recorded on a grid (black dots).

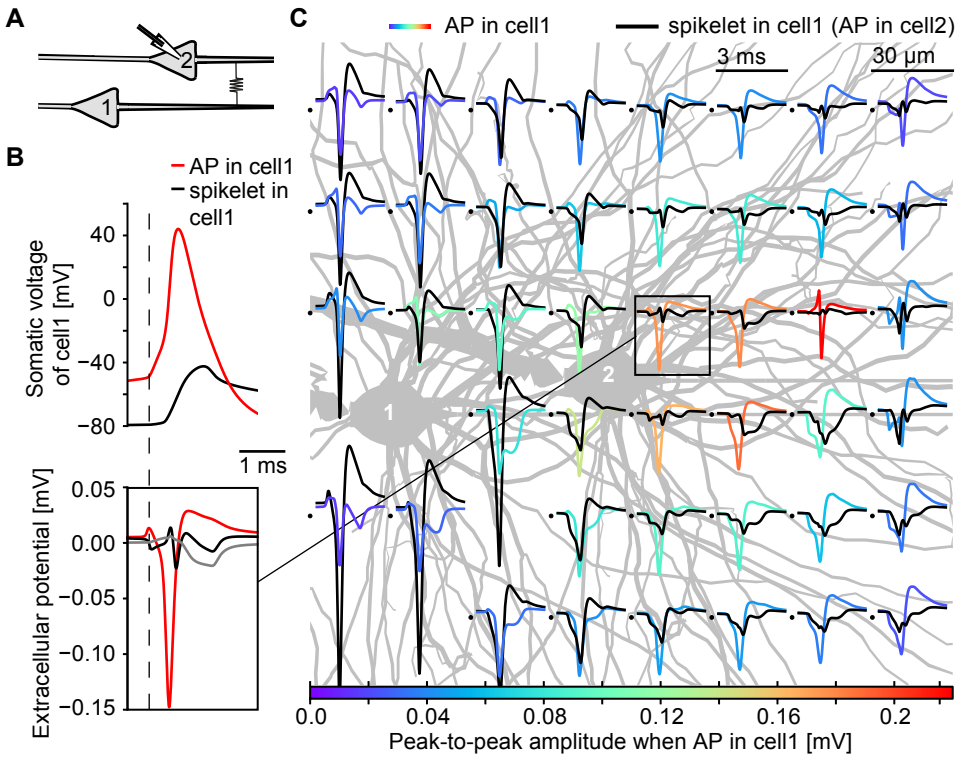

Figure 4.15: Extracellular fields of axonally coupled neurons shifted along the longitudinal axis like in Fig. 4.12, but the upper cell 2 was recorded intracellularly.
A A sketch of the simulation scenario. Distance between the midpoints of the somata was 80 μm. The cells were connected by an axonal gap junction located 57 μm away from the soma of the closer cell 2. **B** + **C** like in Fig. 4.8: **B** top: An intracellularly recorded AP (red) and a spikelet (black) with a large amplitude. Bottom: Extracellular waveforms correlated with the AP (red, PES) and with the spikelet (black, SES). Contribution of the spikeleting cell (cell 2) to the extracellular waveform (black) is shown in gray. **C** Extracellular waveforms correlated with the AP (color, PES) and the spikelet (black, SES), recorded on a grid (black dots).

4.4 Discussion

In this study, I simulated extracellular waveforms of APs and spikelets generated in two electrotonically coupled cells as well as in a single cell. I compared the results to the *in vivo* dual extra- and intracellular data by Chorev and Brecht (2012).

There are four salient features of the experimental data that can be used to assess how well a particular model of spikelet generation matches the data (Table 4.4):

1. Delays between the extracellular correlates of APs and spikelets: In the data, these delays were positive and small (< 0.1 ms).

2. Amplitude ratios: In seven out of eight recordings, the amplitude of the AP-associated extracellular waveform was larger than the spikelet-associated waveform.

3. Waveform shapes: The extracellular waveform linked to spikelets had a qualitatively different shape than the waveform linked to APs.

4. Intracellular spikelet amplitude: The intracellularly recorded spikelets we re characterized by relatively large amplitudes (5–20 mV).

Small positive delays are consistent with all analyzed models. In the electrotonic coupling cases, small delays occured for proximal gap junctions. In the single-cell scenario, there were no delays between the extracellular waveforms of spikelets and APs initiated at the AIS, whereas small positive delays occurred between dendritically initiated APs and spikelets. Larger amplitudes of AP-associated waveforms are expected to arise for coupled cells with distant somata as well as in the single-cell scenario. The one experimental case with a larger spikelet-associated waveform cannot be explained with the single-cell hypothesis, but it is still compatible with the electrotonic coupling scenario. Extracellular waveforms with a reduced sodium peak and a missing potassium peak are a hallmark of the single-cell spikelets. In the coupling condition, such waveforms occured when dendritically coupled neurons were shifted along the main axis and the "superficial" cell was recorded intracellularly. However, the intracellular amplitudes of spikelets arising from dendritic or somatic gap-junction coupling were small (typically < 5 mV) for reasonable conductances of gap junctions.

In summary, the single-cell hypothesis fits best to the experimentally observed spikelet features (Table 4.4). Electrotonic coupling at dendritic, somatic or axonal sites with the two somata located near-by or shifted along the main neuronal axis is consistent only with some aspects of the data. However, the case of axonally coupled cells with large somatic (lateral) distance (> 140 μm), such that the extracellular signal is shaped just by the currents of the intracellularly recorded cell, is compatible with the data and indistinguishable from a single-cell scenario with antidromic spikelets.

A main finding of the study by Chorev and Brecht (2012) was the small positive delay between the extracellular correlates of APs and spikelets. The authors chose to align the intracellular traces to the maximum curvature – the "kink" – and compared the capacitive-peak delays of the extracellular waveforms. Such an approach brings up the question about the inherent relationship between the intracellular kink and the extracellular capacitive peak. The kink marks the onset of the AP or spikelet in the recorded intracellular compartment and corresponds to the maximum of the 2nd derivative of membrane voltage with respect to time (max. $\frac{\mathrm{d}^2 V_m}{\mathrm{d}t^2}$). If the AP is initiated at a remote site, the axial currents precede the local sodium channel activation and give rise to the extracellular capacitive peak. According to the cable equation for an infinite cable of a constant diameter, the extracellular potential is proportional to the 2nd derivative of membrane voltage with respect to space ($V_e \approx \frac{\mathrm{d}^2 V_m}{\mathrm{d}x^2}$). So for a traveling wave,

Table 4.1: Features of the extracellular waveforms: modeling results vs. experimental data (Chorev and Brecht, 2012).

Scenario	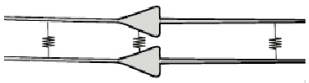			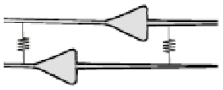		
Extracellular delays	✓	✓	✓	✓	✓	✓
Amplitude ratios	✗	✗	✗	✓	✓	(✓)
Waveform shape	✗	✗	✗	(✓)	✗	✓
Spikelet amplitude	✗	✗	✓	✗	✓	✓

The consistency (green ticks) and inconsistency (red crosses) of properties of different models (first row) with the experimental data. The compared properties are: "Extracellular delays": The delays between the capacitive peaks of the AP- and spikelet-associated extracellular waveforms, aligned to the onset of the intracellular events, were positive and small (< 0.1 ms) in the data. "Amplitude ratios": The amplitudes of the AP-correlated extracellular waveforms were larger in seven out of eight cases than the amplitudes of the corresponding spikelet-correlated extracellular waveforms. "Waveform shapes": The spikelet-linked extracellular waveforms were characterized by a diminished sodium peak and a missing potassium peak when compared to the AP-linked extracellular waveforms recorded at the same location. "Spikelet amplitudes": The amplitudes of the intracellularly recorded spikelets reached 5–20 mV.

i.e., an AP propagating in a cable at a constant speed, the 2nd derivatives of membrane voltage with respect to time and space are proportional ($\frac{\mathrm{d}^2V_m}{\mathrm{d}t^2} \approx \frac{\mathrm{d}^2V_m}{\mathrm{d}x^2}$; Jack et al., 1975, chapter 10) and the capacitive peak (max. $\frac{\mathrm{d}^2V_m}{\mathrm{d}x^2}$) corresponds to the intracellular kink (max. $\frac{\mathrm{d}^2V_m}{\mathrm{d}t^2}$). Thus, an AP propagating in a homogeneous cable (e.g., an axon) generates extracellular fields where the capacitive peak corresponds to the intracellular kink. However, an AP spreading from the AIS through the soma and into the dendrites does not propagate with a constant speed. Moreover, the infinite-cable approximation does not hold and the boundary conditions need to be considered. Figure 4.5 B demonstrates that the capacitive peak recorded close to the soma does not correspond to the somatically recorded kink, but is slightly delayed. Moreover, a delay between the capacitive peak and the kink occurs when the extracellular electrode is shifted along the longitudinal neuronal axis with respect to the intracellular electrode. If the AP is initiated at the AIS, a somatically located intracellular electrode and an extracellular electrode positioned in the apical dendritic tree result in a delayed capacitive peak with respect to the kink because the currents shaping the extracellular waveform originate in the backpropagating AP in the dendrites that is delayed with respect to the somatic AP. Similarly, a capacitive peak occuring before the intracellular kink can be caused, for example, by dendritically placed intracellular electrode while the extracellular electrode is located closer to the soma. (In contrast, no delays due to extracellular signal propagation occur in a purely resistive extracellular medium.) Thus, the relationship between the intracellular kink and the extracellular capacitive peak of a somato-dendritic AP or spikelet is complex and depends also on the placement of recording electrodes.

Chorev and Brecht (2012) reported very small negative delays for some of the spikelet-associated waveform with respect to the onset (kink) of the spikelet. In the simulated single-cell scenario, such small negative delays were observed only for antidromic spikelets, but not for orthodromic spikelets. According to the above considerations, however, these negative delays might be a consequence of dendritic placement of the intracellular electrode. Additionally, the analysis in Chorev and Brecht (2012) was performed on averaged traces, which could also distort the real condition, given the very small kink-peak delays of spikelets.

The single-cell scenario, albeit fitting well to the available data, cannot explain the one experimental recording where the spikelet-associated waveform is larger than the AP-associated waveform (Fig. 4.3 E, boxed traces). This spikelet-correlated waveform, however, looks unusual: its amplitude is large ($\approx$ 1 mV), but the sodium peak is not the dominant phase as is typical for such large-amplitude waveforms (Gold et al., 2009). Rather, the capacitive peak is enlarged as well and appears wider than in all the other traces. To resolve how or where such a waveform could be generated would require further (quantitative) modeling. Yet it would not be the first instance of an extracellular waveform that is hard to explain with state-of-the-art models: Gold et al. (2009) reported large-amplitude positive eAPs recorded in cat visual cortex, which they failed to replicate with compartmental models. The authors concluded that "there is a significant gap in our present understanding of either the spike-generation process in pyramidal neurons, the biophysics of extracellular recording, or both" (Gold et al., 2009).

The process of AP initiation is indeed an ongoing focus of theoretical and experimental work (e.g., Naundorf et al., 2006; Baranauskas and Martina, 2006; Yu et al., 2008; Brette, 2013). Sodium channel dynamics – a main player in AP initiation – is very fast and thus hard to investigate under natural conditions. Instead, sodium channels are typically studied in transfected cells or neuronal slices cooled down to slow the channel dynamics (reviewed in, e.g., Patlak, 1991; Diss et al., 2004; Catterall, 2012) and the *in vivo* properties of the channels have to be estimated from this data.

The main considerations about the biophysics of extracellular recordings concern the properties of the extracellular medium. The assumption of an ohmic extracellular medium has been questioned over the years (e.g., Bédard et al., 2010), yet the apparent low-pass filtering of eAPs

with distance could be explained by intracellular filtering of dendritically propagating APs, together with the fact that the extracellular signal is shaped by progressively larger stretches of neuronal processes as the recording electrode moves away from soma (Pettersen and Einevoll, 2008). Consistently, direct measurements in primate neocortex confirmed ohmic properties of the extracellular medium for the relevant frequencies (from one Hertz to a few kiloHertz; Logothetis et al., 2007). On the other hand, the homogeneity assumption has been shown to be violated in hippocampal area CA1, where the resistivity of the pyramidal layer (*stratum pyramidale*) is around twice the resistivity of the surrounding layers (López-Aguado et al., 2001). Gold et al. (2006) analyzed this effect and found it moderate and strongly distance-dependent, resulting in a maximum 40% increase in the eAP amplitude in the center of the high-resistivity region. Nevertheless, Gold et al. (2006) pointed out that they had to used low values of axial resistivity (70 Ωcm) in their models in order to get extracellular amplitudes as large as experimentally measured. In contrast, the experimentally estimated values of axial resistivity for CA1 pyramidal neurons are at least twice as large: 139–218 Ωcm (Golding et al., 2005). Overall, these discrepancies indeed suggest that our understanding of the processes shaping the extracellular AP waveforms is not complete and requires further study.

Taken together, the dual intra- and extracellular data by Chorev and Brecht (2012) provide strong constraints for the mechanism of spikelet generation. My modeling results revealed that the single-cell hypothesis of spikelet origin fits well to the data. The gap-junction model is consistent with the data only for axonal coupling sites with laterally distant somata of the coupled cells.

Extracellular data combined with compartmental modeling can potentially yield further insights into the exact conditions of spikelet generation. For example, more quantitative modeling could shed light on the origin of the one spikelet-associated waveform with larger amplitude than the AP-associated waveform (Chorev and Brecht, 2012; Fig. 4.3 E, boxed trace) and assess whether it contradicts the single-cell hypothesis of spikelet origin. Moreover, the spikelet-linked extracellular waveform might be used to understand more precisely the state of the pyramidal neuron during spikelet firing. For example, the relative magnitude and shape of the sodium peak contains information about the activation of somato-dendritic sodium channels during spikelet firing (Fig. 4.16).

To understand the dynamics of the axon and particularly the AIS during AP initiation is especially important for spikelets generated with the single-cell mechanism. The axon is a thin structure, so its direct study by means of intracellular recordings is challenging. Unfortunately, axonal eAP waveforms are typically too small to be distinguished from noise in extracellular recordings. However, there are promising new developments of high-density electrode arrays with improved signal-to-noise ratio that might enable detailed study of axonal function with extracellular recordings (Bakkum et al., 2013).

This study demonstrated that cells firing a spikelet do contribute a distinct waveform to the extracellular potential. If the single-cell scenario is correct, the spikelet-associated waveform is misclassified in extracellar recordings as a different unit than the AP-associated waveform, albeit both constitute the output of a single pyramidal cell. Therefore, future studies should assess whether there are ways to relate the AP- and spikelet-associated waveforms generated in a single cell. This, in turn, would allow to analyze the effects of spikelet firing on computation in pyramidal neurons and the networks they are embedded in.

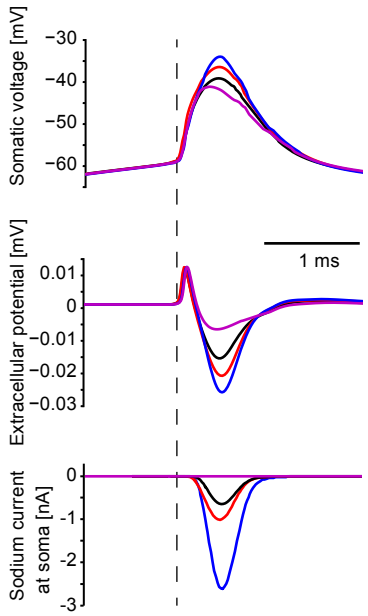

Figure 4.16: Relationships between intracellular and extracellular waveforms of spikelets. Spikelets generated in the Gold-model with different parameter sets (see Methods). Top: somatic intracellular waveforms; middle: extracellular waveforms; bottom: somatic sodium currents; all aligned to the kinks in the somatic voltage traces (dashed line). Note the distinct shape of the extracellular "sodium" peak for the spikelet with no somatic sodium current flow (magenta).

5 Discussion

Spikelets, the small spike-like events, were observed for decades in somatic intracellular recordings of cortical pyramidal neurons. They were shown to influence membrane voltage dynamics including AP initiation. Nevertheless, no consensus could be reached on the mechanism of spikelet generation. In this thesis, I used computational modeling to address the question of spikelet origin in pyramidal neurons.

In chapter 2, I reviewed the mechanisms that can give rise to spikelets. I noted that there are actually two distinct types of pyramidal-neuron spikelets reported in the experimental literature. The large-amplitude spikelets (< 20 mV), which were the focus of this thesis, match the properties of axonally generated spikelets. Moreover, another type of spikelets with small-amplitudes ($1 - 6$ mV) and a brief time course occurs in pyramidal neurons, which might result from ephaptic coupling to a nearby neuron.

In chapter 3, I demonstrated that somatic spikelets of axonal origin might be generated with orthodromic somato-dendritic inputs. Accordingly, these spikelets emerge from an AP initiated at the AIS that propagates down the axon, but does not trigger a somatic AP. Such spikelets provide a means of controlling the dendritic plasticity as they allow to generate axonal output-APs without evoking backpropagating APs in the dendrites. Moreover, such a selective activation of axonal compartments reduces the metabolic cost of AP firing.

In chapter 4, I examined extracellular waveforms of APs and spikelets, and the constraints they provide for the spikelet-generating mechanism. I found that the single-cell hypothesis presented in chapter 3 is consistent with extracellular features of experimentally recorded spikelets. My simulations indicate that a spikelet of axonal origin is manifested in the extracellular recordings as an AP-like waveform, which is different from the extracellular waveform of an AP occuring in the same cell and recorded at the same extracellular location. This finding has implications for extracellular spike sorting since the APs and spikelets generated in a single cell are incorrectly classified as two different units, although they comprise the output of a single pyramidal cell. In summary, the presented work supports the axonal hypothesis of spikelet origin and identifies the functional consequences of spikelet occurrence in cortical pyramidal neurons.

In contrast, the evidence for the gap-junction mechanism of spikelet generation remains ambiguous. My analysis suggests that the somata of the putatively coupled cells should be rather distant from each other for the extracellular waveforms to fit the *in vivo* experimental data (Chorev and Brecht, 2012). However, dual *in vitro* recordings unequivocally identified electronically coupled cell pairs as having very proximal, often touching somata (Mercer et al., 2006; Wang et al., 2010). Despite this and other inconsistencies, it is not straight forward to directly disprove the gap-junctional hypothesis. As has been reviewed in chapter 2, there are no specific gap junction blockers. Moreover, the scenario of spikelets generated due to distal axo-axonal gap junctions, which matches the experimentally recorded intracellular and extracellular spikelet waveforms, is similar to antidromic axonal spikelets generated within a single cell and, thus, cannot be distinguished with single-cell neurophysiology.

However, there is also the possibility that spikelets in pyramidal neurons are generated by a different mechanism *in vivo* than *in vitro*. The axonal single-cell hypothesis studied in the present work fits well to the *in vivo* conditions: The ongoing neural activity renders a portion of the sodium channels unavailable for spiking, especially in the somato-dendritic compartments

where the channels undergo slow inactivation. As a result, the somato-dendritic excitability decreases so that weak orthodromic stimuli are able to generate an AP at the AIS, which, however, does not suffice to depolarize the soma to the firing threshold. So a spikelet appears at the soma instead of an AP. In contrast, spikelets recorded *in vitro* might occur in electronically coupled pairs of neurons. Such coupling can be artifactual, due to the fusion of neuronal processes cut by the slicing procedure (Buzsáki, 2001). Alternatively, Cx36 gap junctions might form as a reaction to the neuronal injury, transiently connecting neighboring neurons within two hours after the damage (Belousov and Fontes, 2013). The waveforms of recorded spikelets predict that the connection occurs at axonal locations.

Alternatively, it has been proposed that the *in vivo* spikelets in pyramidal neurons might be of artifactual origin as well, since they could not be detected in all *in vivo* studies (for example, English et al., 2014). According to my simulation results, the somato-dendritic current sink is an important parameter determining spikelet incidence. This capacitive current sink can be increased by an uncompensated capacitance of the recording electrode, which could promote spikelet generation. However, this artificial increase of capacitance is estimated to be small ($4 - 10$ pF; Thomas, 1977) compared to the input capacitance of pyramidal neurons (range of hundreds of picofarads; Narayanan and Johnston, 2008) and, thus, should not significantly influence spikelet generation. Spikelet occurrence seems to be independent from the electrode type, as spikelets have been recorded with patch-clamp electrodes (Chorev and Brecht, 2012) as well as with sharp microelectrodes (Crochet et al., 2004). Spikelet generation might be influenced by anaesthetics and other pharmacological agents, but the demonstration of spikelets in awake drug-free mice (Harvey et al., 2009) suggests that spikelets in general are not a drug-caused artifact. So I conclude that the artifactual hypothesis of spikelet origin seems unlikely to explain all observed spikelet instances.

In the present thesis, I explored the origin of spikelets in pyramidal neurons with computational methods. Converging lines of evidence from this work as well as from previous (experimental) studies suggest that spikelets in pyramidal neurons are generated in the axon within a single cell. I demonstrated that axonal APs might underlie somatic spikelets even when they are triggered with somato-dendritic (orthodromic) input. This mechanism endows pyramidal neurons with a capability for a selective axonal activation and generation of "output-only" APs. Besides the energetic advantages of such signaling, future studies are needed to assess its further functional implications. For example, spikelet firing might be involved in the regulation of dendritic plasticity dependent on backpropagating APs. Orthodromic spikelets of axonal origin further illustrate that the axons are not "just" cables for a faithful AP propagation, but they might be a vital part of neuronal computations as well.

Acknowledgements

First and foremost, I would like to express my deepest gratitude to my advisor Prof. Richard Kempter for his guidance during my PhD studies. He strongly supported me in my research and writing, while allowing me to experiment and find my own way.

Next I would like to thank Michiel Remme for the very nice and fruitful collaboration, and all the great hints and insights that really helped me advance this project.

I am also very grateful to Prof. Susanne Schreiber, for the many inspiring and helpful debates about my research, but also about the more practical aspects of the scientific life.

Furthermore, I would like to thank Prof. Michael Brecht and Edith Chorev for the generous sharing of their data and for interesting discussions.

My sincere thanks also goes to Romain Brette, for his helpful comments and suggestions about my results, for his invitation to present my research in the CNS workshop last year, as well as for his agreement to review this thesis.

Moreover, I am thankful to Prof. Matthias Hennig for agreeing to be the head of my PhD committee and James Poulet for reviewing this thesis.

I would also like to thank the students, professors, secretaries and admins from ITB and BCCN Berlin, especially the "neuros" from ITB and Prof. Hammerstein. It has been a great pleasure to work in such a welcoming and stimulating environment. It truly feels like a second home.

Last but not least, my thoughts of thanks go to my nearest – my partner, my family, and my friends, who were always there for me.

Bibliography

H Alle and JRP Geiger. Combined analog and action potential coding in hippocampal mossy fibers. *Science*, 311(5765):1290–1293, 2006.

H Alle, A Roth, and JRP Geiger. Energy-efficient action potentials in hippocampal mossy fibers. *Science*, 325(5946):1405–1408, 2009.

V Alvarez-Maubecin, F García-Hernández, JT Williams, and EJ Van Bockstaele. Functional coupling between neurons and glia. *The Journal of Neuroscience*, 20(11):4091, 2000.

CA Anastassiou, R Perin, H Markram, and C Koch. Ephaptic coupling of cortical neurons. *Nature Neuroscience*, 2011.

RD Andrew, CP Taylor, RW Snow, and FE Dudek. Coupling in rat hippocampal slices: dye transfer between CA1 pyramidal cells. *Brain Research Bulletin*, 8(2):211–222, 1982.

PF Apostolides, AD Milstein, C Grienberger, KC Bittner, and JC Magee. Axonal Filtering Allows Reliable Output during Dendritic Plateau-Driven Complex Spiking in CA1 Neurons. *Neuron*, 89(4):770–783, 2016.

A Arvanitaki. Effects evoked in an axon by the activity of a contiguous one. *Journal of Neurophysiology*, 5(2):89–108, 1942.

G Ashida, K Abe, K Funabiki, and M Konishi. Passive soma facilitates submillisecond coincidence detection in the owl's auditory system. *Journal of Neurophysiology*, 97(3):2267–2282, 2007. ISSN 0022-3077.

M Avoli, M Methot, and H Kawasaki. GABA-dependent generation of ectopic action potentials in the rat hippocampus. *European Journal of Neuroscience*, 10(8):2714–2722, 1998. ISSN 1460-9568.

DJ Bakkum, U Frey, M Radivojevic, TL Russell, J Müller, M Fiscella, H Takahashi, and A Hierlemann. Tracking axonal action potential propagation on a high-density microelectrode array across hundreds of sites. *Nature Communications*, 4, 2013.

R Baldi, C Varga, and G Tamas. Differential distribution of KCC2 along the axo-somato-dendritic axis of hippocampal principal cells. *European Journal of Neuroscience*, 2010.

G Baranauskas and M Martina. Sodium currents activate without a Hodgkin and Huxley-type delay in central mammalian neurons. *Journal of Neuroscience*, 26(2):671–684, 2006.

G Baranauskas, Y David, and IA Fleidervish. Spatial mismatch between the Na+ flux and spike initiation in axon initial segment. *Proceedings of the National Academy of Sciences*, 110 (10):4051–4056, 2013.

C Bédard, S Rodrigues, NR, D Contreras, and A Destexhe. Evidence for frequency-dependent extracellular impedance from the transfer function between extracellular and intracellular potentials. *Journal of Computational Neuroscience*, 29(3):389–403, 2010.

AB Belousov and JD Fontes. Neuronal gap junctions: making and breaking connections during development and injury. *Trends in Neurosciences*, 36(4):227–236, 2013.

KJ Bender and LO Trussell. Axon initial segment Ca2+ channels influence action potential generation and timing. *Neuron*, 61(2):259–271, 2009. ISSN 0896-6273.

MVL Bennett and A Pereda. Pyramid power: Principal cells of the hippocampus unite! *Brain Cell Biology*, 35(1):5–11, 2006. ISSN 1559-7105.

MVL Bennett and RS Zukin. Electrical coupling and neuronal synchronization in the mammalian brain. *Neuron*, 41(4):495–511, 2004.

O Bernander, RJ Douglas, KA Martin, and C Koch. Synaptic background activity influences spatiotemporal integration in single pyramidal cells. *Proceedings of the National Academy of Sciences*, 88(24):11569, 1991.

MO Bevensee, TR Cummins, GG Haddad, WF Boron, and G Boyarsky. pH regulation in single CA1 neurons acutely isolated from the hippocampi of immature and mature rats. *The Journal of Physiology*, 494(Pt 2):315, 1996.

A Bjorefeldt, U Andreasson, J Daborg, I Riebe, P Wasling, Henrik Zetterberg, and Eric Hanse. Human cerebrospinal fluid increases the excitability of pyramidal neurons in the in vitro brain slice. *Journal of Physiology*, 593(1):231–243, 2015.

R Brette. Sharpness of spike initiation in neurons explained by compartmentalization. *PLOS Computational Biology*, 9(12):e1003338, 2013.

MW Brightman and TS Reese. Junctions between intimately apposed cell membranes in the vertebrate brain. *The Journal of Cell Biology*, 40(3):648, 1969.

R Bruzzone, SG Hormuzdi, MT Barbe, A Herb, and H Monyer. Pannexins, a family of gap junction proteins expressed in brain. *Proceedings of the National Academy of Sciences of the United States of America*, 100(23):13644, 2003.

EH Buhl, ZS Han, Z Lorinczi, VV Stezhka, SV Karnup, and P Somogyi. Physiological properties of anatomically identified axo-axonic cells in the rat hippocampus. *Journal of Neurophysiology*, 71(4):1289, 1994.

TH Bullock, MVL Bennett, D Johnston, R Josephson, E Marder, and RD Fields. The neuron doctrine, redux. *Science*, 310(5749):791, 2005.

G Buzsáki. Electrical wiring of the oscillating brain. *Neuron*, 31(3):342–344, 2001.

G Buzsáki. Large-scale recording of neuronal ensembles. *Nature Neuroscience*, 7(5):446–451, 2004.

NT Carnevale and ML Hines. *The NEURON Book*. Cambridge UP, Cambridge, UK, 2006.

DB Carr, M Day, AR Cantrell, J Held, T Scheuer, William A Catterall, and D James Surmeier. Transmitter modulation of slow, activity-dependent alterations in sodium channel availability endows neurons with a novel form of cellular plasticity. *Neuron*, 39(5):793–806, 2003.

WA Catterall. Voltage-gated sodium channels at 60: structure, function and pathophysiology. *Journal of Physiology*, 590(11):2577–2589, 2012.

Q Chang and RJ Balice-Gordon. Gap junctional communication among developing and injured motor neurons. *Brain research reviews*, 32(1):242–249, 2000.

N Chen, J Yu, H Qian, R Ge, and JH Wang. Axons amplify somatic incomplete spikes into uniform amplitudes in mouse cortical pyramidal neurons. *PloS one*, 5(7):e11868, 2010.

Y Chen, FH Yu, EM Sharp, D Beacham, T Scheuer, and WA Catterall. Functional properties and differential neuromodulation of Nav1. 6 channels. *Molecular and Cellular Neuroscience*, 38(4): 607–615, 2008.

M Chesler. Regulation and modulation of pH in the brain. *Physiological Reviews*, 83(4):1183, 2003.

E Chorev and M Brecht. In vivo dual intra-and extracellular recordings suggest bidirectional coupling between CA1 pyramidal neurons. *Journal of Neurophysiology*, 108(6):1584–1593, 2012.

BD Clark, EM Goldberg, and B Rudy. Electrogenic tuning of the axon initial segment. *The Neuroscientist*, 15(6):651, 2009.

CM Colbert and E Pan. Ion channel properties underlying axonal action potential initiation in pyramidal neurons. *Nature Neuroscience*, 5(6):533–538, 2002.

BW Connors and AR Kriegstein. Cellular physiology of the turtle visual cortex: distinctive properties of pyramidal and stellate neurons. *Journal of Neuroscience*, 6(1):164–177, 1986.

BW Connors and MA Long. Electrical synapses in the mammalian brain. *Annual Review of Neuroscience*, 27:393–418, 2004.

BW Connors, LS Benardo, and DA Prince. Carbon dioxide sensitivity of dye coupling among glia and neurons of the neocortex. *The Journal of neuroscience*, 4(5):1324, 1984.

D Contreras, R Curró Dossi, and M Steriade. Electrophysiological properties of cat reticular thalamic neurones in vivo. *The Journal of Physiology*, 470(1):273, 1993.

JS Coombs, JC Eccles, and P Fatt. The electrical properties of the motoneurone membrane. *Journal of Physiology*, 130(2):291, 1955. ISSN 0022-3751.

JS Coombs, DR Curtis, and JC Eccles. The interpretation of spike potentials of motoneurones. *Journal of Physiology*, 139(2):198, 1957a.

JS Coombs, DR Curtis, and JC Eccles. The generation of impulses in motoneurones. *Journal of Physiology*, 139(2):232, 1957b.

F Cotel, R Exley, SJ Cragg, and JF Perrier. Serotonin spillover onto the axon initial segment of motoneurons induces central fatigue by inhibiting action potential initiation. *Proceedings of the National Academy of Sciences of USA*, 110(12):4774–9, March 2013. doi: 10.1073/pnas.1216150110.

S Crochet, P Fuentealba, I Timofeev, and M Steriade. Selective amplification of neocortical neuronal output by fast prepotentials in vivo. *Cerebral Cortex*, 14(10):1110–21, October 2004. doi: 10.1093/cercor/bhh071.

SJ Cruikshank, M Hopperstad, M Younger, BW Connors, DC Spray, and M Srinivas. Potent block of Cx36 and Cx50 gap junction channels by mefloquine. *Proceedings of the National Academy of Sciences of the United States of America*, 101(33):12364, 2004.

J Csicsvari, DA Henze, B Jamieson, KD Harris, A Sirota, P Barthó, KD Wise, and G Buzsáki. Massively parallel recording of unit and local field potentials with silicon-based electrodes. *Journal of Neurophysiology*, 90(2):1314, 2003.

S Curti and J O'Brien. Characteristics and plasticity of electrical synaptic transmission. *BMC Cell Biology*, 17(1):59, 2016.

JT Davie, BA Clark, and M Hausser. The origin of the complex spike in cerebellar Purkinje cells. *Journal of Neuroscience*, 28(30):7599, 2008.

D Debanne, A Bialowas, and S Rama. What are the mechanisms for analogue and digital signalling in the brain? *Nature Reviews Neuroscience*, 14(1):63–69, 2013.

M Deschenes, M Paradis, JP Roy, and M Steriade. Electrophysiology of neurons of lateral thalamic nuclei in cat: resting properties and burst discharges. *Journal of neurophysiology*, 51 (6):1196, 1984.

A Destexhe, M Rudolph, J M Fellous, and T J Sejnowski. Fluctuating synaptic conductances recreate in vivo-like activity in neocortical neurons. *Neuroscience*, 107(1):13–24, 2001.

J Deuchars and AM Thomson. CA1 pyramid-pyramid connections in rat hippocampus in vitro: dual intracellular recordings with biocytin filling. *Neuroscience*, 74(4):1009–1018, 1996.

F Ding, J O'Donnell, Q Xu, N Kang, N Goldman, and M Nedergaard. Changes in the composition of brain interstitial ions control the sleep-wake cycle. *Science*, 352(6285):550–555, 2016.

JKJ Diss, SP Fraser, and MBA Djamgoz. Voltage-gated Na+ channels: multiplicity of expression, plasticity, functional implications and pathophysiological aspects. *European Biophysics Journal*, 33(3):180–193, 2004.

A Draguhn, RD Traub, D Schmitz, and JGR Jefferys. Electrical coupling underlies high-frequency oscillations in the hippocampus in vitro. *Nature*, 394(6689):189–192, 1998.

T Dugladze, D Schmitz, MA Whittington, I Vida, and T Gloveli. Segregation of axonal and somatic activity during fast network oscillations. *Science*, 336(6087):1458–61, June 2012. doi: 10.1126/science.1222017.

CG Dulla and JR Huguenard. Who let the spikes out? *Nature Neuroscience*, 12(8):959–960, 2009.

D Engel and P Jonas. Presynaptic action potential amplification by voltage-gated Na+ channels in hippocampal mossy fiber boutons. *Neuron*, 45(3):405–417, 2005.

DF English, A Peyrache, E Stark, L Roux, D Vallentin, MA Long, and G Buzsáki. Excitation and inhibition compete to control spiking during hippocampal ripples: intracellular study in behaving mice. *Journal of Neuroscience*, 34(49):16509–16517, 2014.

J Epsztein, AK Lee, E Chorev, and M Brecht. Impact of spikelets on hippocampal CA1 pyramidal cell activity during spatial exploration. *Science*, 327(5964):474, 2010.

J Epsztein, M Brecht, and AK Lee. Intracellular Determinants of Hippocampal CA1 Place and Silent Cell Activity in a Novel Environment. *Neuron*, 70(1):109–120, 2011.

T Fellin. Communication between neurons and astrocytes: relevance to the modulation of synaptic and network activity. *Journal of neurochemistry*, 108(3):533–544, 2009.

RD Fields. Oligodendrocytes changing the rules: action potentials in glia and oligodendrocytes controlling action potentials. *The Neuroscientist*, 14(6):540, 2008.

IA. Fleidervish, E Katz, A Scheller, M Meisler, S Gobbels, MJ Gutnick, F Kirchhoff, and F Wolf. Role of axonal $Na_V1.6$ Na^+ channels in action potential generation in Layer 5 neocortical neurons. Göttingen Meeting of the German Neuroscience Society, 2011.

IA Fleidervish, N Lasser-Ross, MJ Gutnick, and WN Ross. Na^+ imaging reveals little difference in action potential-evoked Na^+ influx between axon and soma. *Nature Neuroscience*, 13(7): 852–860, 2010. ISSN 1097-6256.

A Foust, M Popovic, D Zecevic, and DA McCormick. Action Potentials Initiate in the Axon Initial Segment and Propagate through Axon Collaterals Reliably in Cerebellar Purkinje Neurons. *Journal of Neuroscience*, 30(20):6891, 2010.

JE Fox, M Bikson, and JGR Jefferys. Tissue resistance changes and the profile of synchronized neuronal activity during ictal events in the low-calcium model of epilepsy. *Journal of Neurophysiology*, 92(1):181–188, 2004.

P Fuentealba, S Crochet, I Timofeev, M Bazhenov, TJ Sejnowski, and M Steriade. Experimental evidence and modeling studies support a synchronizing role for electrical coupling in the cat thalamic reticular neurons in vivo. *European Journal of Neuroscience*, 20(1):111–119, 2004.

M Galarreta and S Hestrin. A network of fast-spiking cells in the neocortex connected by electrical synapses. *Nature*, 402(6757):72–75, 1999.

M Galarreta and S Hestrin. Electrical synapses between GABA-releasing interneurons. *Nature Reviews Neuroscience*, 2(6):425–433, 2001.

S Gasparini, M Migliore, and JC Magee. On the initiation and propagation of dendritic spikes in CA1 pyramidal neurons. *Journal of Neuroscience*, 24(49):11046, 2004.

JRP Geiger and P Jonas. Dynamic control of presynaptic Ca 2+ inflow by fast-inactivating K+ channels in hippocampal mossy fiber boutons. *Neuron*, 28(3):927–939, 2000.

JR Gibson, M Beierlein, and BW Connors. Functional properties of electrical synapses between inhibitory interneurons of neocortical layer 4. *Journal of Neurophysiology*, 93(1):467–480, 2005.

LL Glickfeld, JD Roberts, P Somogyi, and M Scanziani. Interneurons hyperpolarize pyramidal cells along their entire somatodendritic axis. *Nature Neuroscience*, 12(1):21–23, 2008.

C Gold, DA Henze, C Koch, and G Buzsaki. On the origin of the extracellular action potential waveform: a modeling study. *Journal of neurophysiology*, 95(5):3113, 2006. ISSN 0022-3077.

C Gold, DA Henze, and C Koch. Using extracellular action potential recordings to constrain compartmental models. *Journal of Computational Neuroscience*, 23(1):39–58, 2007.

C Gold, CC Girardin, KAC Martin, and C Koch. High-amplitude positive spikes recorded extracellularly in cat visual cortex. *Journal of Neurophysiology*, 102(6):3340–51, December 2009. doi: 10.1152/jn.91365.2008.

NL Golding, TJ Mickus, Y Katz, WL Kath, and N Spruston. Factors mediating powerful voltage attenuation along CA1 pyramidal neuron dendrites. *Journal of Physiology*, 568(1):69–82, 2005.

NL Golding and N Spruston. Dendritic sodium spikes are variable triggers of axonal action potentials in hippocampal CA1 pyramidal neurons. *Neuron*, 21(5):1189–1200, 1998. ISSN 0896-6273.

NL Golding, NP Staff, and N Spruston. Dendritic spikes as a mechanism for cooperative long-term potentiation. *Nature*, 418(6895):326–331, 2002. ISSN 0028-0836.

D González-Nieto, JM Gómez-Hernández, B Larrosa, C Gutiérrez, MD Muñoz, I Fasciani, J O'Brien, A Zappalà, F Cicirata, and LC Barrio. Regulation of neuronal connexin-36 channels by pH. *Proceedings of the National Academy of Sciences*, 105(44):17169, 2008.

MS Grubb and J Burrone. Activity-dependent relocation of the axon initial segment fine-tunes neuronal excitability. *Nature*, 465(7301):1070–1074, 2010a. ISSN 0028-0836.

MS Grubb and J Burrone. Building and maintaining the axon initial segment. *Current Opinion in Neurobiology*, 20(4):481–488, 2010b.

J Gründemann and M Häusser. A plastic axonal hotspot. *Nature*, 465(7301):1022–1023, 2010.

MJ Gutnick, R Lobel-Yaakov, and G Rimon. Incidence of neuronal dye-coupling in neocortical slices depends on the plane of section. *Neuroscience*, 15(3):659–666, 1985.

JS Haas, CM Greenwald, and AE Pereda. Activity-dependent plasticity of electrical synapses: increasing evidence for its presence and functional roles in the mammalian brain. *BMC Cell Biology*, 17(1):51, 2016.

MM Halassa and PG Haydon. Integrated brain circuits: astrocytic networks modulate neuronal activity and behavior. *Annual review of physiology*, (0), 2010.

F Hamzei-Sichani, N Kamasawa, WGM Janssen, T Yasumura, KGV Davidson, PR Hof, SL Wearne, MG Stewart, SR Young, MA Whittington JE Rash, and RD Traub. Gap junctions on hippocampal mossy fiber axons demonstrated by thin-section electron microscopy and freeze–fracture replica immunogold labeling. *Proceedings of the National Academy of Sciences*, 104(30):12548, 2007.

L Harris et al. Emerging issues of connexin channels: biophysics fills the gap. *Quarterly reviews of biophysics*, 34(03):325–472, 2001.

CD Harvey, F Collman, DA Dombeck, and DW Tank. Intracellular dynamics of hippocampal place cells during virtual navigation. *Nature*, 461(7266):941–6, October 2009. doi: 10.1038/nature08499.

KL Hedstrom, X Xu, Y Ogawa, R Frischknecht, CI Seidenbecher, P Shrager, and MN Rasband. Neurofascin assembles a specialized extracellular matrix at the axon initial segment. *Journal of Cell Biology*, 178(5):875–886, 2007.

DA Henze and G Buzsaki. Action potential threshold of hippocampal pyramidal cells in vivo is increased by recent spiking activity. *Neuroscience*, 105(1):121–130, 2001.

AS Hill, A Nishino, K Nakajo, G Zhang, JR Fineman, ME Selzer, Y Okamura, and EC Cooper. Ion channel clustering at the axon initial segment and node of Ranvier evolved sequentially in early chordates. *PLoS genetics*, 4(12):e1000317, 2008.

ML Hines, AP Davison, and E Muller. Neuron and Python. *Frontiers in Neuroinformatics*, 3: 1–12, 2009.

AL Hodgkin and AF Huxley. A quantitative description of membrane current and its application to conduction and excitation in nerve. *Journal of Physiology*, 117(4):500, 1952.

GR Holt and C Koch. Electrical interactions via the extracellular potential near cell bodies. *Journal of Computational Neuroscience*, 6(2):169–84, 1999.

SG Hormuzdi, I Pais, FEN LeBeau, S K Towers, A Rozov, EH Buhl, MA Whittington, and H Monyer. Impaired electrical signaling disrupts gamma frequency oscillations in connexin 36-deficient mice. *Neuron*, 31(3):487–495, 2001.

W Hu, C Tian, T Li, M Yang, H Hou, and Y Shu. Distinct contributions of Nav1. 6 and Nav1. 2 in action potential initiation and backpropagation. *Nature Neuroscience*, 12(8):996–1002, 2009. ISSN 1097-6256.

SW Hughes, KL Blethyn, DW Cope, and V Crunelli. Properties and origin of spikelets in thalamocortical neurones in vitro. *Neuroscience*, 110(3):395–401, 2002. ISSN 0306-4522.

JJB Jack, D Noble, and RW Tsien. *Electric current flow in excitable cells*. Clarendon Press Oxford, 1975.

T Jarsky, A Roxin, WL Kath, and N Spruston. Conditional dendritic spike propagation following distal synaptic activation of hippocampal CA1 pyramidal neurons. *Nature Neuroscience*, 8(12):1667–1676, 2005.

JG Jefferys. Nonsynaptic modulation of neuronal activity in the brain: electric currents and extracellular ions. *Physiological Reviews*, 75(4):689–723, 1995.

D Johnston and SMS Wu. *Foundations of cellular neurophysiology*. MIT press Cambridge, MA:, 1995.

ER Kandel, WA Spencer, and FJ Brinley. Electrophysiology of hippocampal neurons: I. Sequential invasion and synaptic organization. *Journal of Neurophysiology*, 24(3):225, 1961.

E Kaplan and R Shapley. The origin of the S (slow) potential in the mammalian lateral geniculate nucleus. *Experimental Brain Research*, 55(1):111–116, 1984.

S Keros and JJ Hablitz. Ectopic action potential generation in cortical interneurons during synchronized GABA responses. *Neuroscience*, 131(4):833–842, 2005.

ZM Khaliq and IM Raman. Axonal propagation of simple and complex spikes in cerebellar Purkinje neurons. *Journal of Neuroscience*, 25(2):454–463, 2005.

S Khirug, J Yamada, R Afzalov, J Voipio, L Khiroug, and K Kaila. GABAergic depolarization of the axon initial segment in cortical principal neurons is caused by the Na–K–2Cl cotransporter NKCC1. *The Journal of Neuroscience*, 28(18):4635, 2008.

T Klausberger, PJ Magill, LF Márton, JDB Roberts, PM Cobden, G Buzsáki, and P Somogyi. Brain-state-and cell-type-specific firing of hippocampal interneurons in vivo. *Nature*, 421 (6925):844–848, 2003.

WD Knowles, PG Funch, and PA Schwartzkroin. Electrotonic and dye coupling in hippocampal CA1 pyramidal cells in vitro. *Neuroscience*, 7(7):1713–1722, 1982. ISSN 0306-4522.

MHP Kole and GJ Stuart. Is action potential threshold lowest in the axon? *Nature Neuroscience*, 11(11):1253–1255, 2008.

MHP Kole, JJ Letzkus, and GJ Stuart. Axon initial segment Kv1 channels control axonal action potential waveform and synaptic efficacy. *Neuron*, 55(4):633–647, 2007. ISSN 0896-6273.

MHP Kole, SU Ilschner, BM Kampa, SR Williams, PC Ruben, and GJ Stuart. Action potential generation requires a high sodium channel density in the axon initial segment. *Nature*, 11(2): 178–186, 2008.

GJ Kress, MJ Dowling, LN Eisenman, and S Mennerick. Axonal sodium channel distribution shapes the depolarized action potential threshold of dentate granule neurons. *Hippocampus*, 20(4):558–571, 2010.

H Kuba, Y Oichi, and H Ohmori. Presynaptic activity regulates Na+ channel distribution at the axon initial segment. *Nature*, 465(7301):1075–1078, 2010. ISSN 0028-0836.

ME Larkum, S Watanabe, NL-Ross, P Rhodes, and WN Ross. Dendritic properties of turtle pyramidal neurons. *Journal of Neurophysiology*, 99(2):683–694, 2008.

XG Li, P Somogyi, JM Tepper, and G Buzsaki. Axonal and dendritic arborization of an intracellularly labeled chandelier cell in the CA1 region of rat hippocampus. *Experimental brain research*, 90(3):519–525, 1992.

H Lindén, E Hagen, S Lęski, ES Norheim, KH Pettersen, and GT Einevoll. LFPy: a tool for biophysical simulation of extracellular potentials generated by detailed model neurons. *Frontiers in Neuroinformatics*, 7:41, 2013. doi: 10.3389/fninf.2013.00041.

R Llinas, R Baker, and C Sotelo. Electrotonic coupling between neurons in cat inferior olive. *Journal of Neurophysiology*, 37(3):560, 1974.

NK Logothetis, C Kayser, and A Oeltermann. In vivo measurement of cortical impedance spectrum in monkeys: implications for signal propagation. *Neuron*, 55(5):809–823, 2007.

L López-Aguado, JM Ibarz, and O Herreras. Activity-dependent changes of tissue resistivity in the CA1 region in vivo are layer-specific: modulation of evoked potentials. *Neuroscience*, 108(2):249–262, 2001.

A Lorincz and Z Nusser. Cell-type-dependent molecular composition of the axon initial segment. *The Journal of Neuroscience*, 28(53):14329, 2008.

A Lorincz and Z Nusser. Molecular identity of dendritic voltage-gated sodium channels. *Science*, 328(5980):906, 2010.

A Losonczy, JK Makara, and Jeffrey C Magee. Compartmentalized dendritic plasticity and input feature storage in neurons. *Nature*, 452(7186):436–441, 2008.

BA MacVicar and RJ Thompson. Non-junction functions of pannexin-1 channels. *Trends in neurosciences*, 33(2):93–102, 2010.

BA MacVicar, N Ropert, and K Krnjevic. Dye-coupling between pyramidal cells of rat hippocampus in vivo. *Brain Research*, 238(1):239–244, 1982.

ZF Mainen, NT Carnevale, AM Zador, BJ Claiborne, and TH Brown. Electrotonic architecture of hippocampal CA1 pyramidal neurons based on three-dimensional reconstructions. *Journal of Neurophysiology*, 76(3):1904–1923, 1996.

ZF Mainen and TJ Sejnowski. Influence of dendritic structure on firing pattern in model neocortical neurons. *Nature*, 382(6589):363–366, 1996. ISSN 0028-0836.

P Mann-Metzer and Y Yarom. Electrotonic coupling interacts with intrinsic properties to generate synchronized activity in cerebellar networks of inhibitory interneurons. *The Journal of Neuroscience*, 19(9):3298, 1999.

TW Margrie, AH Meyer, A Caputi, H Monyer, MT Hasan, AT Schaefer, W Denk, and M Brecht. Targeted whole-cell recordings in the mammalian brain in vivo. *Neuron*, 39(6):911–918, 2003. ISSN 0896-6273.

M Martina, I Vida, and P Jonas. Distal initiation and active propagation of action potentials in interneuron dendrites. *Science*, 287(5451):295, 2000.

A Mathy, SSN Ho, JT Davie, IC Duguid, BA Clark, and M Häusser. Encoding of oscillations by axonal bursts in inferior olive neurons. *Neuron*, 62(3):388–399, 2009.

S Maxeiner, O Krüger, K Schilling, O Traub, S Urschel, and K Willecke. Spatiotemporal transcription of connexin45 during brain development results in neuronal expression in adult mice. *Neuroscience*, 119(3):689–700, 2003.

JP Meeks and S Mennerick. Action potential initiation and propagation in CA3 pyramidal axons. *Journal of Neurophysiology*, 97(5):3460–3472, 2007.

A Mercer, AP Bannister, and AM Thomson. Electrical coupling between pyramidal cells in adult cortical regions. *Brain Cell Biology*, 35(1):13–27, 2006. ISSN 1559-7105.

A Mercer. Electrically coupled excitatory neurones in cortical regions. *Brain Research*, 1487: 192–197, 2012.

JN Mercer, CS Chan, T Tkatch, J Held, and DJ Surmeier. Nav1.6 sodium channels are critical to pacemaking and fast spiking in globus pallidus neurons. *The Journal of Neuroscience*, 27(49): 13552, 2007.

T Mickus, HY Jung, and N Spruston. Properties of slow, cumulative sodium channel inactivation in rat hippocampal CA1 pyramidal neurons. *Biophysical Journal*, 76(2):846–860, 1999.

M Migliore, DA Hoffman, JC Magee, and D Johnston. Role of an A-type K+ conductance in the back-propagation of action potentials in the dendrites of hippocampal pyramidal neurons. *Journal of Computational Neuroscience*, 7(1):5–15, 1999.

K Mizuseki, K Diba, E Pastalkova, and G Buzsáki. Hippocampal CA1 pyramidal cells form functionally distinct sublayers. *Nature Neuroscience*, 14(9):1174–81, September 2011. doi: 10.1038/nn.2894.

G Molnár, S Oláh, G Komlósi, M Füle, J Szabadics, C Varga, P Barzó, and G Tamás. Complex events initiated by individual spikes in the human cerebral cortex. *PLoS biology*, 6(9):e222, 2008.

P Monsivais, BA Clark, A Roth, and M Hausser. Determinants of action potential propagation in cerebellar Purkinje cell axons. *Journal of Neuroscience*, 25(2):464, 2005.

RJ Montoro and R Yuste. Gap junctions in developing neocortex: a review. *Brain Research Reviews*, 47(1-3):216–226, 2004.

C Müller, H Beck, D Coulter, and S Remy. Inhibitory control of linear and supralinear dendritic excitation in CA1 pyramidal neurons. *Neuron*, 75(5):851–864, 2012.

JI Nagy, FE Dudek, and JE Rash. Update on connexins and gap junctions in neurons and glia in the mammalian nervous system. *Brain Research Reviews*, 47(1-3):191–215, 2004.

R Narayanan and D Johnston. The h channel mediates location dependence and plasticity of intrinsic phase response in rat hippocampal neurons. *Journal of Neuroscience*, 28(22):5846–5860, 2008.

B Naundorf, F Wolf, and M Volgushev. Unique features of action potential initiation in cortical neurons. *Nature*, 440(7087):1060–1063, 2006.

A Nunez, E García-Austt, and W Buņo. In vivo electrophysiological analysis of lucifer yellow-coupled hippocampal pyramids. *Experimental Neurology*, 108(1):76–82, 1990. ISSN 0014-4886.

J O'Brien. The ever-changing electrical synapse. *Current Opinion in Neurobiology*, 29:64–72, 2014.

I Pais, SG Hormuzdi, H Monyer, RD Traub, IC Wood, EH Buhl, MA Whittington, and FEN LeBeau. Sharp wave-like activity in the hippocampus in vitro in mice lacking the gap junction protein connexin 36. *Journal of Neurophysiology*, 89(4):2046–2054, 2003.

SL Palay, C Sotelo, A Peters, and PM Orkand. The axon hillock and the initial segment. *The Journal of Cell Biology*, 38(1):193, 1968.

LM Palmer and GJ Stuart. Site of action potential initiation in layer 5 pyramidal neurons. *Journal of Neuroscience*, 26(6):1854–1863, 2006.

C Papatheodoropoulos. A possible role of ectopic action potentials in the in vitro hippocampal sharp wave-ripple complexes. *Neuroscience*, 157(3):495–501, 2008.

J Patlak. Molecular kinetics of voltage-dependent Na+ channels. *Physiological Reviews*, 71(4): 1047–1080, 1991.

JL Perez Velazquez and PL Carlen. Gap junctions, synchrony and seizures. *Trends in Neurosciences*, 23(2):68–74, 2000.

JL Perez-Velazquez, TA Valiante, and PL Carlen. Modulation of gap junctional mechanisms during calcium-free induced field burst activity: a possible role for electrotonic coupling in epileptogenesis. *Journal of Neuroscience*, 14(7):4308–4317, 1994.

JL Perez Velazquez, D Han, and PL Carlen. Neurotransmitter modulation of gap junctional communication in the rat hippocampus. *European Journal of Neuroscience*, 9(12):2522–2531, 1997. ISSN 1460-9568.

KH Pettersen and GT Einevoll. Amplitude variability and extracellular low-pass filtering of neuronal spikes. *Biophysical Journal*, 94(3):784–802, February 2008. doi: 10.1529/biophysj.107.111179.

J Platkiewicz and R Brette. Impact of fast sodium channel inactivation on spike threshold dynamics and synaptic integration. *PLOS Comput Biol*, 7(5):e1001129, 2011.

JR Pugh and CE Jahr. Axonal $GABA_A$ Receptors Increase Cerebellar Granule Cell Excitability and Synaptic Activity. *The Journal of Neuroscience*, 31(2):565, 2011.

W Rall. Membrane potential transients and membrane time constant of motoneurons. *Experimental Neurology*, 2(5):503–532, 1960.

MN Rasband. The axon initial segment and the maintenance of neuronal polarity. *Nature Reviews Neuroscience*, 11(8):552–562, 2010.

JE Rash, WA Staines, T Yasumura, D Patel, CS Furman, GL Stelmack, and JI Nagy. Immunogold evidence that neuronal gap junctions in adult rat brain and spinal cord contain connexin-36 but not connexin-32 or connexin-43. *Proceedings of the National Academy of Sciences of the United States of America*, 97(13):7573, 2000.

JE Rash, KGV Davidson, N Kamasawa, and T Yasumura. Freeze-fracture Replica Immunogold Labeling (FRIL) in Biological Electron Microscope. *Microscopy and Microanalysis*, 11(S02):138–139, 2005.

AD Redish, FP Battaglia, MK Chawla, AD Ekstrom, JL Gerrard, P Lipa, ES Rosenzweig, PF Worley, JF Guzowski, BL McNaughton, et al. Independence of firing correlates of anatomically proximate hippocampal pyramidal cells. *Journal of Neuroscience*, 21(5):RC134, 2001.

S Remy, J Csicsvari, and H Beck. Activity-dependent control of neuronal output by local and global dendritic spike attenuation. *Neuron*, 61(6):906–916, 2009.

C Rivera, J Voipio, and K Kaila. Two developmental switches in GABAergic signalling: the K+–Cl- cotransporter KCC2 and carbonic anhydrase CAVII. *The Journal of physiology*, 562(1): 27, 2005.

P Rojas, A Akrouh, LN Eisenman, and S Mennerick. Differential Effects of Axon Initial Segment and Somatodendritic $GABA_A$ Receptors on Excitability Measures in Rat Dentate Granule Neurons. *Journal of Neurophysiology*, 105(1):366, 2011.

N Rouach, M Segal, A Koulakoff, C Giaume, and E Avignone. Carbenoxolone blockade of neuronal network activity in culture is not mediated by an action on gap junctions. *The Journal of Physiology*, 553(3):729–745, 2003.

M Royeck, MT Horstmann, S Remy, M Reitze, Y Yaari, and H Beck. Role of axonal Nav1. 6 sodium channels in action potential initiation of CA1 pyramidal neurons. *Journal of Neurophysiology*, 100(4):2361–2380, 2008. ISSN 0022-3077.

R Rozental, M Srinivas, and DC Spray. How to close a gap junction channel: Efficacies and potencies of uncoupling agents. *Methods in molecular biology*, 154:447–476, 2001.

AM Rush, SD Dib-Hajj, and SG Waxman. Electrophysiological properties of two axonal sodium channels, Nav1.2 and Nav1.6, expressed in mouse spinal sensory neurones. *The Journal of Physiology*, 564(3):803, 2005.

JC Saez, MA Retamal, D Basilio, FF Bukauskas, and MVL Bennett. Connexin-based gap junction hemichannels: gating mechanisms. *Biochimica et Biophysica Acta (BBA)-Biomembranes*, 1711(2):215–224, 2005.

F Saraga, L Ng, and FK Skinner. Distal gap junctions and active dendrites can tune network dynamics. *Journal of Neurophysiology*, 95(3):1669, 2006a. ISSN 0022-3077.

F Saraga, XL Zhang, L Zhang, PL Carlen, and FK Skinner. Exploring gap junction location and density in electrically coupled hippocampal oriens interneurons. *Neurocomputing*, 69(10-12): 1048–1052, 2006b.

D Schlingloff, S Káli, TF Freund, N Hájos, and AI Gulyás. Mechanisms of sharp wave initiation and ripple generation. *Journal of Neuroscience*, 34(34):11385–11398, 2014.

D Schmitz, S Schuchmann, A Fisahn, A Draguhn, EH Buhl, E Petrasch-Parwez, R Dermietzel, U Heinemann, and RD Traub. Axo-Axonal Coupling: A Novel Mechanism for Ultrafast Neuronal Communication. *Neuron*, 31(5):831–840, 2001. ISSN 0896-6273.

B Scholl, S Andoni, and NJ Priebe. Functional characterization of spikelet activity in the primary visual cortex. *Journal of Physiology*, 593(22):4979–4994, 2015.

R Scorcioni, MT Lazarewicz, and GA Ascoli. Quantitative morphometry of hippocampal pyramidal cells: differences between anatomical classes and reconstructing laboratories. *Journal of Comparative Neurology*, 473(2):177–193, 2004.

MM Shah, M Migliore, I Valencia, EC Cooper, and DA Brown. Functional significance of axonal Kv7 channels in hippocampal pyramidal neurons. *Proceedings of the National Academy of Sciences*, 105(22):7869, 2008.

MEJ Sheffield, TK Best, BD Mensh, WL Kath, and N Spruston. Slow integration leads to persistent action potential firing in distal axons of coupled interneurons. *Nature Neuroscience*, 14: 200–207, 2010.

VI Shestopalov and Y Panchin. Pannexins and gap junction protein diversity. *Cellular and Molecular Life Sciences*, 65(3):376–394, 2008.

Y Shu, A Hasenstaub, A Duque, Y Yu, and DA McCormick. Modulation of intracortical synaptic potentials by presynaptic somatic membrane potential. *Nature*, 441(7094):761–765, 2006.

VA Skeberdis, L Rimkute, A Skeberdyte, N Paulauskas, and FF Bukauskas. pH-dependent modulation of connexin-based gap junctional uncouplers. *The Journal of Physiology*, 2011.

JJ Sloper. Gap junctions between dendrites in the primate neocortex. *Brain Research*, 44(2):641, 1972.

JJ Sloper and TPS Powell. Gap junctions between dendrites and somata of neurons in the primate sensori-motor cortex. *Proceedings of the Royal Society of London. Series B, Biological Sciences*, 203(1150):39–47, 1978.

WA Spencer and ER Kandel. Electrophysiology of hippocampal neurons: IV. Fast prepotentials. *Journal of Neurophysiology*, 24(3):272, 1961. ISSN 0022-3077.

DC Spray, AL Harris, and MV Bennett. Gap junctional conductance is a simple and sensitive function of intracellular pH. *Science*, 211(4483):712, 1981.

N Spruston. Pyramidal neurons: dendritic structure and synaptic integration. *Nature Reviews Neuroscience*, 9(3):206–221, 2008.

N Spruston, Y Schiller, G Stuart, and B Sakmann. Activity-dependent action potential invasion and calcium influx into hippocampal CA1 dendrites. *Science*, 268(5208):297–300, 1995.

E Stark, L Roux, R Eichler, Y Senzai, S Royer, and G Buzsáki. Pyramidal cell-interneuron interactions underlie hippocampal ripple oscillations. *Neuron*, 83(2):467–480, 2014.

SF Stasheff, M Hines, and WA Wilson. Axon terminal hyperexcitability associated with epileptogenesis in vitro. I. Origin of ectopic spikes. *Journal of neurophysiology*, 70(3):961, 1993.

M Steriade, RC Dossi, D Pare, and G Oakson. Fast oscillations (20-40 Hz) in thalamocortical systems and their potentiation by mesopontine cholinergic nuclei in the cat. *Proceedings of the National Academy of Sciences*, 88(10):4396, 1991.

G Stuart, J Schiller, and B Sakmann. Action potential initiation and propagation in rat neocortical pyramidal neurons. *Journal of Physiology*, 505(3):617–632, 1997.

Q Sun, KV Srinivas, A Sotayo, and SA Siegelbaum. Dendritic Na+ spikes enable cortical input to drive action potential output from hippocampal CA2 pyramidal neurons. *eLife*, 3:e04551, 2014.

J Szabadics, C Varga, G Molnár, S Oláh, P Barzó, and G Tamás. Excitatory effect of GABAergic axo-axonic cells in cortical microcircuits. *Science*, 311(5758):233, 2006.

TM Szabo and MJ Zoran. Transient electrical coupling regulates formation of neuronal networks. *Brain research*, 1129:63–71, 2007.

G Tamás, EH Buhl, A Lörincz, and P Somogyi. Proximally targeted GABAergic synapses and gap junctions synchronize cortical interneurons. *Nature Neuroscience*, 3(4):366–371, 2000.

AL Taylor. What we talk about when we talk about capacitance measured with the voltage-clamp step method. *Journal of Computational Neuroscience*, 32(1):167–175, 2012.

B Teubner, J Degen, G Söhl, M Güldenagel, FF Bukauskas, EB Trexler, VK Verselis, CI De Zeeuw, CG Lee, CA Kozak, et al. Functional expression of the murine connexin 36 gene coding for a neuron-specific gap junctional protein. *Journal of Membrane Biology*, 176(3):249–262, 2000.

MV Thomas. Microelectrode amplifier with improved method of input-capacitance neutralisation. *Medical and Biological Engineering and Computing*, 15(4):450–454, 1977.

C Thome, T Kelly, A Yanez, C Schultz, M Engelhardt, SB Cambridge, M Both, A Draguhn, H Beck, and AV Egorov. Axon-carrying dendrites convey privileged synaptic input in hippocampal neurons. *Neuron*, 83(6):1418–1430, 2014.

I Timofeev and M Steriade. Fast (mainly 30–100 Hz) oscillations in the cat cerebellothalamic pathway and their synchronization with cortical potentials. *The Journal of Physiology*, 504(1): 153–168, 1997.

KR Tovar, BJ Maher, and GL Westbrook. Direct actions of carbenoxolone on synaptic transmission and neuronal membrane properties. *Journal of Neurophysiology*, 102(2):974, 2009.

RD Traub, JG Jefferys, R Miles, MA Whittington, and K Toth. A branching dendritic model of a rodent CA3 pyramidal neurone. *The Journal of Physiology*, 481(Pt 1):79, 1994.

RD Traub, D Schmitz, JGR Jefferys, and A Draguhn. High-frequency population oscillations are predicted to occur in hippocampal pyramidal neuronal networks interconnected by axoaxonal gap junctions. *Neuroscience*, 92(2):407–426, 1999. ISSN 0306-4522.

HC Tuckwell. *Introduction to theoretical neurobiology. Vol. 1, Linear cable theory and dendritic structure and stochastic theories*. Cambridge: Cambridge University Press, 1988.

RW Turner, DER Meyers, and JL Barker. Fast pre-potential generation in rat hippocampal CA1 pyramidal neurons. *Neuroscience*, 53(4):949–959, 1993. ISSN 0306-4522.

G Turrigiano. Too many cooks? Intrinsic and synaptic homeostatic mechanisms in cortical circuit refinement. *Annual Review of Neuroscience*, 34:89–103, 2011.

TA Valiante, JL Perez Velazquez, SS Jahromi, and PL Carlen. Coupling potentials in CA1 neurons during calcium-free-induced field burst activity. *Journal of Neuroscience*, 15(10):6946, 1995.

EJ Vigmond, JL Perez Velazquez, TA Valiante, B Bardakjian, and PL Carlen. Mechanisms of electrical coupling between pyramidal cells. *Journal of Neurophysiology*, 78(6):3107, 1997.

T Viitanen, E Ruusuvuori, K Kaila, and J Voipio. The K^+–Cl^- cotransporter KCC2 promotes GABAergic excitation in the mature rat hippocampus. *The Journal of physiology*, 588(9):1527, 2010.

M Volgushev, A Malyshev, P Balaban, M Chistiakova, S Volgushev, and F Wolf. Onset dynamics of action potentials in rat neocortical neurons and identified snail neurons: quantification of the difference. *PlOS One*, 3(4):e1962, 2008.

Y Wang, A Barakat, and H Zhou. Electrotonic coupling between pyramidal neurons in the neocortex. *PLOS One*, 5(4):e10253, 2010.

SA Weiss and DS Faber. Field effects in the CNS play functional roles. *Frontiers in Neural Circuits*, 4:15, 2010.

K Willecke, J Eiberger, J Degen, D Eckardt, A Romualdi, M Güldenagel, U Deutsch, and G Söhl. Structural and functional diversity of connexin genes in the mouse and human genome. *Biological Chemistry*, 383(5):725–737, 2002.

KA Wilmes, H Sprekeler, and S Schreiber. Inhibition as a Binary Switch for Excitatory Plasticity in Pyramidal Neurons. *PLoS Comput Biol*, 12(3):e1004768, 2016.

MJ Wilson, D Yoshikami, L Azam, J Gajewiak, BM Olivera, G Bulaj, and MM Zhang. μ-Conotoxins that differentially block sodium channels Nav1.1 through 1.8 identify those responsible for action potentials in sciatic nerve. *Proceedings of the National Academy of Sciences*, 2011.

VC Wimmer, CA Reid, EYW So, SF Berkovic, and S Petrou. Axon initial segment dysfunction in epilepsy. *The Journal of Physiology*, 588(11):1829–1840, 2010.

RK Wong and M Stewart. Different firing patterns generated in dendrites and somata of CA1 pyramidal neurones in guinea-pig hippocampus. *Journal of Physiology*, 457(1):675, 1992. ISSN 0022-3751.

A Woodruff, Q Xu, SA Anderson, and R Yuste. Depolarizing effect of neocortical chandelier neurons. *Frontiers in Neural Circuits*, 3, 2009.

AR Woodruff, H Monyer, and P Sah. GABAergic excitation in the basolateral amygdala. *The Journal of Neuroscience*, 26(46):11881, 2006.

AR Woodruff, SA Anderson, and R Yuste. The Enigmatic Function of Chandelier Cells. *Frontiers in Neuroscience*, 4, 2010.

B Yang, R Tadavarty, JY Xu, and BR Sastry. Activity-mediated plasticity of GABA equilibrium potential in rat hippocampal CA1 neurons. *Experimental neurology*, 221(1):157–165, 2010.

Y Yu, Y Shu, and DA McCormick. Cortical action potential backpropagation explains spike threshold variability and rapid-onset kinetics. *Journal of Neuroscience*, 28(29):7260, 2008.

Y Yu, C Maureira, X Liu, and D McCormick. P/Q and N channels control baseline and spike-triggered calcium levels in neocortical axons and synaptic boutons. *The Journal of Neuroscience*, 30(35):11858, 2010.

C Yue, S Remy, H Su, H Beck, and Y Yaari. Proximal persistent Na+ channels drive spike afterdepolarizations and associated bursting in adult CA1 pyramidal cells. *The Journal of neuroscience*, 25(42):9704, 2005.

H Zhang and AS Verkman. Microfiberoptic measurement of extracellular space volume in brain and tumor slices based on fluorescent dye partitioning. *Biophysical journal*, 99(4):1284–1291, 2010.

XL Zhang, L Zhang, and PL Carlen. Electrotonic coupling between stratum oriens interneurones in the intact in vitro mouse juvenile hippocampus. *The Journal of Physiology*, 558(3): 825–839, 2004.

Y Zhang, JL Perez Velazquez, GF Tian, CP Wu, FK Skinner, PL Carlen, and L Zhang. Slow oscillations ($\leq$ 1 Hz) mediated by GABAergic interneuronal networks in rat hippocampus. *Journal of Neuroscience*, 18(22):9256, 1998.

Selbständigkeitserklärung

Ich erkläre, dass ich die vorliegende Arbeit selbständig und nur unter Verwendung der angegebenen Literatur und Hilfsmittel angefertigt habe.

Berlin, den 16.09.2016 Martina Michalikova